TERAHERTZ SPECTROSCOPY OF $YBa_2Cu_3O_{7-\delta}$ THIN FILMS

TERAHERTZ SPECTROSCOPY OF OPTICALLY EXCITED $YBa_2Cu_3O_{7-\delta}$ THIN FILMS

By

ANNA KRISTOFFERSEN, B.Sc.

A Thesis

Submitted to the School of Graduate Studies

in Partial Fulfillment of the Requirements

for the Degree

Doctor of Philosophy

McMaster University

DOCTOR OF PHILOSOPHY (2009) McMaster University
(Physics and Astronomy) Hamilton, Ontario

TITLE: Terahertz Spectroscopy of Dynamic $YBa_2Cu_3O_{7-\delta}$ Thin Films

AUTHOR: Anna Kristoffersen, B.Sc. (University of New Brunswick)

SUPERVISOR: Dr. J.S. Preston

NUMBER OF PAGES: xx, 175

ABSTRACT

The optical properties of high temperature superconductors have long been of interest to condensed matter physicists. The majority of the research has concentrated on the steady-state properties of cuprates. Optical excitation of cuprate superconductors provides the valuable opportunity to study the dynamics of the superconducting state via the evolution of the superconducting condensate and excited quasiparticles. Terahertz (THz) spectroscopy is particularly attractive for the study of thin film cuprates, as the energies available in broad spectrum THz pulses lie below the maximum superconducting gap values. Optical pump THz probe spectroscopy utilizes a high energy infrared pulse to destroy the condensate and excite quasiparticles states out of equilibrium. The THz probe is capable of spectrally resolving the sample's temporal response to the optical perturbation. The direct measurement of both the amplitude and phase of the electric fields associated with the transmitted THz radiation allow for the calculation of both the real and imaginary parts of the conductivity. This offers the tantalizing potential of untangling the condensate's recovery from quasi-particle dynamics.

The focus of this thesis will be upon the long timescale dynamics of $YBa_2Cu_3O_{7-\delta}$ (YBCO) thin films. It has generally been believed that the condensate is fully recovered after a few picoseconds, and that the recovery of these films at longer timescales is essentially a thermal process although perhaps slowed by a phonon bottleneck. However, we will show spectral evidence that this picture cannot fully explain long lived dynamics in YBCO thin films. Specifically we see a suppression of the low frequency components of the optical conductivity. This anomaly is consistent with the formation of spatial inhomogeneity in the superconducting fraction, which likely arises from a non-uniform formation of the condensate across the film. The role of local inhomogeneity in the condensate and its effect on the conductivity of the thin film will be discussed. Evidence of intrinsic inhomogeneities in YBCO films may prove useful to the theoretical

understanding of condensate dynamics in the cuprates. The spectral response of three doping levels, from optimally doped to underdoped YBCO, will also be shown, with a brief discussion of the normal state dynamics in underdoped films and the possible sensitivity of THz radiation to pseudogap dynamics.

Acknowledgements

I would like to take this opportunity to thank my supervisor Dr. John Preston for his guidance and insight during this project. I owe thanks to my supervisor Dr. Tom Timusk for patiently answering my questions. With their direction I was able to learn a great deal of interesting science, and ultimately make a discovery of which I am truly proud. I would also like to thank Dr. Harold Haugen for keeping the laser lab safe for all of us to use and for his helpful comments on my thesis and presentation. Thanks go to the rest of the defense committee, Dr. Elisabeth Nicol and Dr. Zdislav Kovarik for reading my thesis.

Dr. Rob Hughes was a great help not only as a lab mentor - discussing results and experimental difficulties, but as a source of excellent quality superconducting films. It is not easy growing such thin films, especially when the substrate of choice is not viable, but Rob was more than capable of producing high quality samples. Thanks also go to Dr. Henry Tiedje for training me on ultra-fast laser maintenance and how to build and use Terahertz systems. I owe thanks to Dr. Paul Dube for keeping the helium supply flowing.

I am grateful for the countless scientific (and silly) discussions that were so helpful during my time at McMaster. I'd like to acknowledge Dr. Travis Crawford, Eugene Hsu, Ben Doyle, Derek Sahota, Clare Armstrong, Nicholas Mailman, Dr. John Nam, Paul Speziale, and Gabe Devenyi.

I'd also like to thank my friends and loved ones for all their love and support. Thanks to Rod, a true partner, for always being there for me. I'd also like to thank my mother Margot for being so supportive, and my brothers Samuel and Petter. You guys are the best family anyone could ask for. Thanks for always being interested in my research and also for encouraging me to take breaks! I'd also like to acknowledge Sarah, Jen and Robin for being such good friends. I am very lucky to have so many kind and wonderful people in my life.

This thesis is dedicated to my mother,

and my loving husband Rod

TABLE OF CONTENTS

Chapter 6 Conclusions and Future work

PARAMETERS

Symbol	Description	Typical Units
Δ	Superconducting energy gap	eV
ε_0	Permittivity of free space	F/m
ε	Electric permittivity	F/m
λ	Penetration depth	nm
λ	Wavelength	nm
μ_0	Permeability of free space	N/A^2
ρ	resistivity	$m\Omega$ cm
σ	Optical conductivity	$m\Omega^{-1}cm^{-1}$
σ_1	Real part of optical conductivity	$m\Omega^{-1}cm^{-1}$
σ_2	Imaginary part of optical conductivity	$m\Omega^{-1}cm^{-1}$
τ	Scattering time	s
$\tau_{e\text{-}e}$	Electron-electron scattering time	s
$\tau_{e\text{-}ph}$	Electron-phonon scattering time	s
τ_γ	Phonon escape time	s
φ	Phase angle	radians
χ	Electric susceptibility	-
κ	Extinction coefficient	-
ω	Frequency	s^{-1}
ω_p	Plasma frequency	Hz
c	Speed of light	m/s
c_j	"backscattering" term for Drude-Smith model	-
C_v	Specific heat	$Jcm^{-3}K^{-1}$
d	Film thickness	nm
e	Electron unit charge	C
E	Electric field	V/m
f_s	Superconducting fraction	-
H	Magnetic field	T
J	Current density	A/cm^2
ℓ	Path length	m
m	Electron mass	Kg
M	Magnetization	A/m
n_0	Total electron density	-
n_n	Normal quasiparticles density	-
n_s	Superconducting quasiparticles density	-
n	Index of refraction	-
P	Polarization	C/m^2

P	Power	mW
r	Electro-optical constant	m/V
R	Reflectance	-
t	Reduced temperature, T/T_c	-
t	Transmission through film/substrate, normalized by bare substrate	-
t^*	Transmission through bare substrate, normalized by film/substrate	
t	Time	s
T	Transmission	-
T_o	Ambient sample temperature	K
T_c	Critical temperature	K
U	Energy density	J/cm^3
Z_0	Impedance of free space	Ω

ABBREVIATIONS

ARPES	Angle resolved photo-emission
BSCCO	$Bi_2Sr_2Ca_nCu_{n+1}O_{2n+6-d}$
CW	Continuous wave
DAQ	Data acquisition
FWHM	Full width half maximum
HTSC	High temperature superconductor
IR	Infrared
LSAT	$(LaAlO_3)_{0.3}(Sr_2AlTaO_6)_{0.7}$
PLD	Pulsed laser deposition
STM	Scanning tunneling microscopy
THz	Terahertz
YBCO	$YBa_2Cu_3O_{7-\delta}$

LIST OF FIGURES

Chapter 1. Introduction

1.1 Introduction to Superconductivity

For the lay person, the most impressive and defining characteristic of a superconductor is the absence of electrical resistance below the superconducting transition temperature, or T_c. This leads to the temptation to view a superconductor as an ideal metal - a metal with a complete absence of scattering. From this perspective it is noteworthy that in the metallic state above T_c, the "best"* superconductors often have the largest amount of scattering. Above their T_c the highest temperature superconductors, the cuprates, are marginal metals. Although this simplistic view captures some of the salient features of superconductivity it does not address the origin of superconductivity, or many of the observed characteristics of high temperature superconductors.

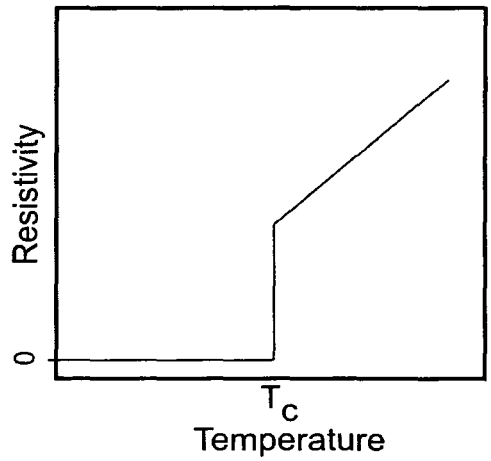

Figure 1.1 The temperature dependent resistivity of cuprate superconductors typically exhibit a sharp transition from a linear a dependence of resistivity with temperature above the critical temperature to a zero resistivity below it.

* Best here refers to those with the highest transition temperature.

1.1.1 BCS Theory

In 1957, Bardeen Cooper and Schrieffer developed a theory that would explain conventional superconductors[1]. Although electrons are fermions, superconductivity has striking similarities to the superfluidity observed for ^{4}He at low temperatures. Superfluidity originates from a significant fraction of the bosons entering a single, collective quantum state known as the Bose condensate.

BCS theory postulates that in the superconducting state, the electrons are bound into entities known as Cooper pairs.* In the superconducting condensate, there is significant overlap between pairs, due to their size. The size of the pairs is known as the coherence length. In a close analogy to superfluidity, this condensate has the ability to move through the lattice unhindered by random scattering events, thus creating the celebrated superconducting property of zero resistance at finite temperatures. An important fundamental issue is how the electrostatic repulsion of the electrons is overcome during the pairing process. To help visualize the attraction mechanism, consider one of the electrons in the pair as it moves through the lattice. This negatively charged electron will exert an attractive force on the positively charged lattice ions as it moves through the crystal structure. In response to this, the lattice distorts creating a region of enhanced positive charge. It is this positive charge which attracts the second electron of the quasiparticle pair. The net result is an attractive force between two electrons mediated by a lattice vibration (or phonon). The finite binding energy of the Cooper pairs is responsible for the superconducting energy gap that opens up below T_c. An illustration of the superconducting gap is shown in Figure 1.2.

---

* Cooper pairs are constructed from electrons with opposite spins, and equal but opposite momenta leading to a spin-zero composite particle with zero momentum. They are frequently labeled by the momenta of the contributing electron states.

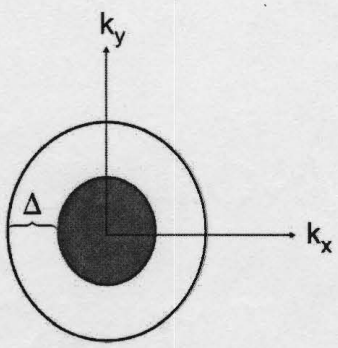

Figure 1.2 s-wave gap. The gap is uniform in k-space for s-wave superconductors. The green region represents the Fermi surface. The superconducting gap has an energy of Δ.

Much of the description above also holds for cuprate superconductors. However, while conventional superconductors have a so called "s-wave" energy gap that is independent of direction, high temperature cuprates, such as $YBa_2Cu_3O_{7-\delta}$ (YBCO), exhibit a d-wave gap[2,3] such as shown in Figure 1.3. The d-wave gap is anisotropic, containing nodes along the $|k_x| = |k_y|$ directions in k-space. Angle resolved photo-emission spectroscopy (ARPES) measurements for the high temperature superconductor (HTSC) YBCO have found that the maximum values for the d-wave gap are $\Delta^x_{max} = 44$ meV, and $\Delta^y_{max} = 29.3$ meV.[4]

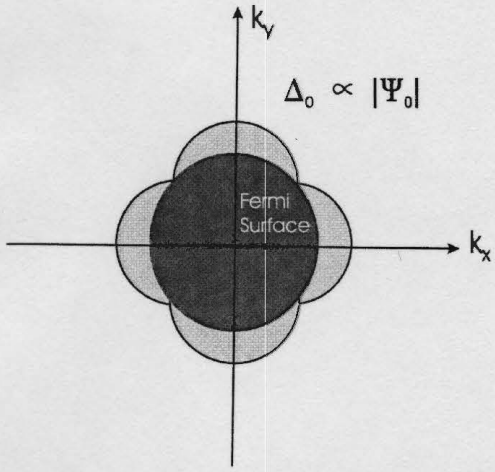

Figure 1.3 Superconducting gap for a d-wave superconductor.

1.1.2 The two-fluid model and the electrodynamics of HTSC

It would be natural to assume that once a superconductor's temperature is lowered below T_c, its conductivity arises entirely from the superconducting condensate. However, some electrons will be thermally excited out of the condensate at nonzero temperatures. It is useful to consider two coexisting populations of electrons: one participating in the condensate, and the other behaving as a normal metal.[5,6*] The normal electrons are irrelevant to the resistance-less response to static electric fields exhibited below T_c; however they play an important role in the response of the superconductor at non-zero frequencies.

In the two-fluid model the normal and superconducting electrons are treated as separate fluids i.e.: $n_0 = n_s + n_n$ where n_0 is the total electron density, n_s is the density of the paired superconducting electrons, and n_n is the density of the normal electrons.[5] Above T_c, n_s is given to be 0 and n_n is therefore equal to n_0. At T = 0, $n_s = n_0$ and $n_n = 0$. The superconducting fraction, f_s, is given by: n_s/n_0 (see Figure 1.4). The original two-fluid model developed by Gorter and Casimir for conventional superconductors has a $1-t^4$ dependence of the superconducting fraction, as shown in equation 1.1, where t is the reduced temperature T/T_c.

$$n_s = n_0(1-t^4) \qquad \textbf{1.1}$$

For cuprates, a $1-t^2$ has been empirically found to be a better fit to their temperature dependence.[7,8] Although this does not capture the linear dependence of the superconducting fraction at low temperatures, as seen by Bonn *et al.*, this approximation also works for thin film cuprates.

The currents associated with the condensate and normal fluids simply add:

$$J = J_s + J_n \qquad \textbf{1.2}$$

---

* Although this technically violates the concept that electrons are indistinguishable, it has proven to be a remarkably robust approximation

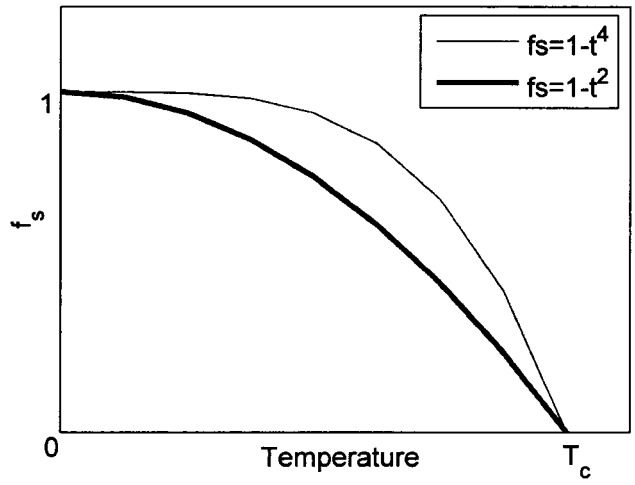

Figure 1.4 Two models for the superconducting density of states as a function of temperature. For conventional superconductors the Gorter-Casimir model $fs=1-t^4$ is used. For HTSC D-wave superconductors $fs=1-t^2$ is used.

It is straightforward to understand the normal contribution to the current, as it obeys Ohm's law. To understand the superconducting contribution one must turn to the London equations:[9,10]

$$\frac{dJ_s}{dt} = \left(\frac{n_s e^2}{m}\right) E \qquad \textbf{1.3}$$

where E is the electric field, and

$$\nabla \times J_s = -\frac{H}{4\pi\lambda^2} \qquad \textbf{1.4}$$

The first equation is considered to be Ohm's law for superconductors, and implies that there is no energy loss due to random collisions. The second equation describes the penetration of a magnetic field, H, into the superconductor, as characterized by λ, which is given by: $\lambda = \sqrt{\frac{m}{4\pi n_s e^2}}$ where m is the effective mass of the electron.

The optical conductivity $\sigma = \sigma_1 + i\sigma_2$ is given by:

$$J_s + J_n = \sigma E = (\sigma_s + \sigma_n) E \qquad \textbf{1.5}$$

The contribution from the normal state is given by the Drude conductivity:

$$\sigma_n = \frac{n_n e^2 \tau}{m(1 - i\omega\tau)} \quad \textbf{1.6}$$

the superconducting contribution is:

$$\sigma_S = \frac{i n_S e^2}{m\omega} \quad \textbf{1.7}$$

thus the real part of the optical conductivity, σ_1 comes entirely from the normal conduction electrons and follows the Drude model, while at low frequencies, the imaginary part* of the optical conductivity σ_2 is dominated by the superconducting condensate.

1.1.3 Drude-Smith Model

There are many times when the standard Drude model is not appropriate. Indeed, it is remarkable that such a simplistic model often works so well in describing metals. There have been many modifications to the Drude model presented to refine agreement with experimental results.[11,12,13] In this section the Drude-Smith model[14] will be discussed. This model is commonly used to fit experimental data from inhomogeneous samples.[15,16,17,18] The Drude-Smith model is given by:

$$\sigma = \frac{ne^2\tau}{m(1 - i\omega\tau)}\left[1 + \sum_j \frac{c_j}{(1 - i\omega\tau)^j}\right] \quad \textbf{1.8}$$

where c_j, generally referred to as the "backscattering" term,† ranges from -1 to 0. This fitting parameter is meant to represent the fraction of the original velocity retained by an electron after its jth collision, where c_j = -1 for case of complete backscattering, and c = 0

---

* The imaginary part of the conductivity refers to the component of the current that is out of phase with the electric field due to lag from the scattering time τ.

† Smith originally called it the "persistence of velocity."

for isotropic scattering. The form for the modification to the Drude model comes from a examining the Poisson distribution for the number of quasi-particle collisions in time t:

$$p_j(0,t) = \left(\frac{t}{\tau}\right)^j \frac{e^{-t/\tau}}{j!} \qquad 1.9$$

Typically, the higher order terms are ignored, and only the first term is included. The main advantage of the Drude-Smith model, is that it can fit the suppression of the conductivity at low frequencies commonly seen in inhomogeneous samples. This suppression is illustrated in Figure 1.5, where the real and imaginary parts of the Drude-Smith conductivity is shown for c = 0, -0.5 and -1. This model can be useful in fitting conductivities that exhibit a suppression at low frequencies, often caused by inhomogeneity.

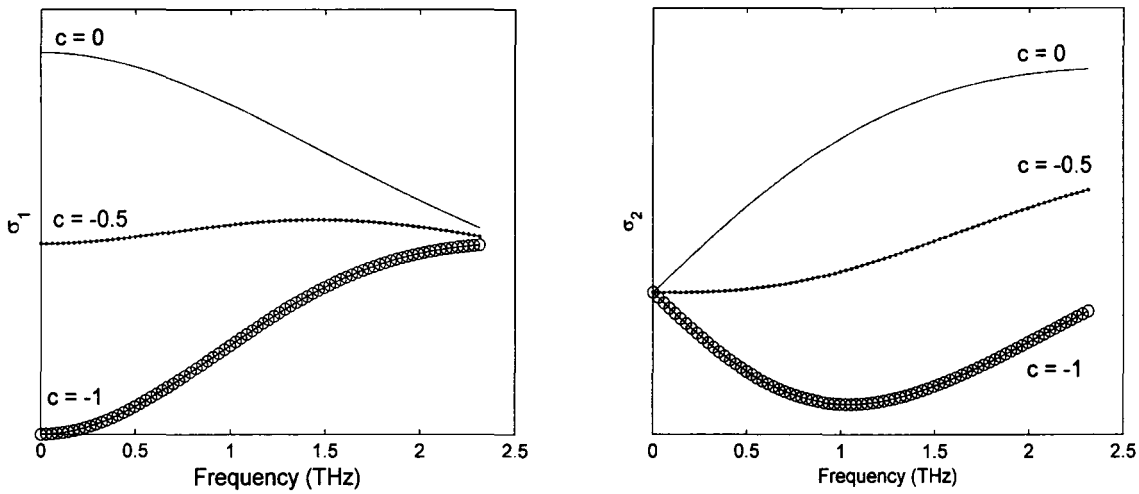

Figure 1.5 Including Smith's first expansion term in the Drude conductivity suppresses the low frequency conductivity for the real part of the conductivity as illustrated by the left figure. The figure on the right shows that in the THz regime, the higher frequencies of the imaginary part of the conductivity is affected the greatest. The theoretical conductivity used a scattering time of ~0.1 ps.

1.2 Introduction to YBCO

Optimally doped $YBa_2Cu_3O_{7-\delta}$ ($\delta \sim 0.09$) superconducts at T_c = 93.7 K.[19] The transition temperature can be lowered by increasing δ and at a doping level of $\delta \sim 0.655$ it becomes insulating and anti-ferromagnetic.[20] A schematic of the phase diagram is shown in Figure 1.6. The dotted line in the figure indicates an exotic region known as the pseudogap region.[21,22] Angle resolved photo-emission spectra (ARPES), in addition to other probes, show an energy gap above T_c in underdoped cuprates, known as the pseudogap.[23] There has been considerable speculation that this region is associated with the formation of pairs that lack the coherence to induce superconductivity.[24,25,26,27]

The crystal structure of YBCO is shown in Figure 1.7. Severely underdoped YBCO, (δ=1), has a tetragonal crystal structure with $a = b$ = 3.859 Å, and c = 11.814 Å. Increased doping results in a tetragonal to orthorhombic phase transition brought on by the formation of copper-oxygen chains. Optimally doped YBCO has an orthorhombic crystal structure with a = 3.82 Å, b = 3.88 Å, and c = 11.65 Å. It is widely accepted that the copper oxygen planes are responsible for the superconductivity in these materials[28].

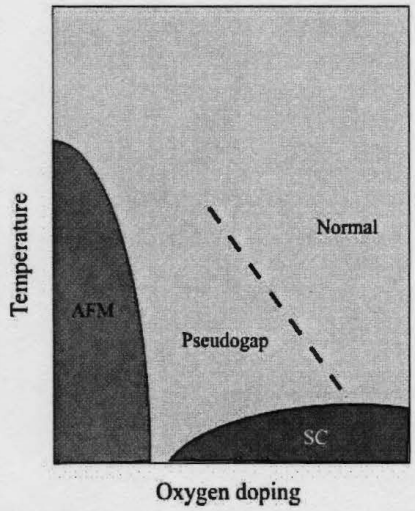

Figure 1.6 Phase diagram for YBCO. As oxygen doping increases it changes from anti-ferromagnetic to superconducting. The dashed line indicates the existence of a third phase, commonly referred to as the pseudogap.

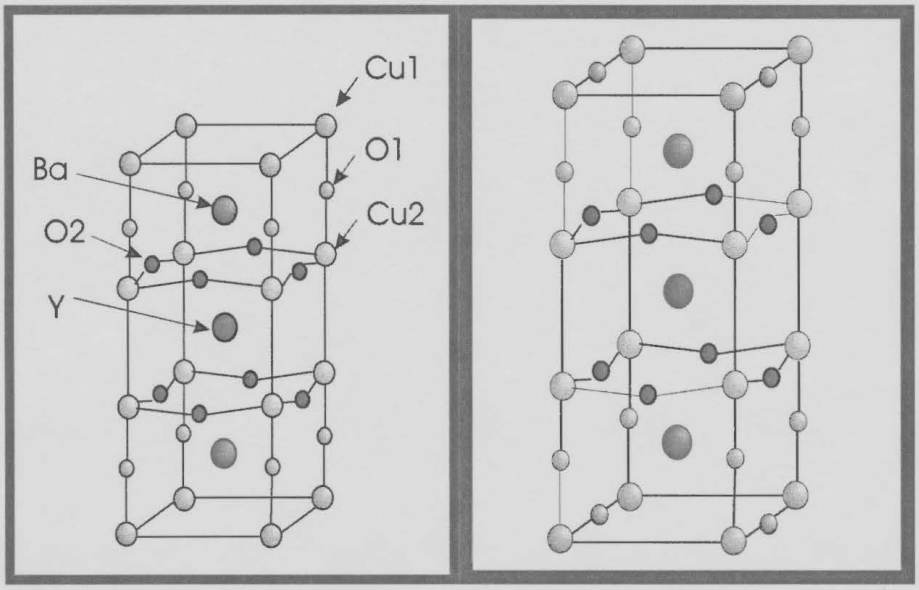

Figure 1.7 Schematics of the unit cells showing the crystal structure of $YBa_2Cu_3O_{7-\delta}$ unit cell. On the right, δ=1, and on the left δ=0.

1.3 Introduction to THz spectroscopy

Terahertz (THz) radiation is loosely defined as those wavelengths extending from 0.003 - 3 mm* (Figure 1.8). These wavelengths correspond to photons with energies on the order of an meV. This energy range is important to many electronic processes, making THz frequencies ideal for studying superconducting[29,30,31,32] and semiconducting materials,[33,34,35] as well as many biological processes.[36,37,38]

Spectroscopic and imaging techniques have been developed for most of the electromagnetic spectrum. Until recently, these techniques did not cover the THz range of frequencies. This gap is now being filled using THz transmission spectroscopy.[39,40]

---

* or alternatively, in units of wavenumbers, from 3 to 3333 cm^{-1}

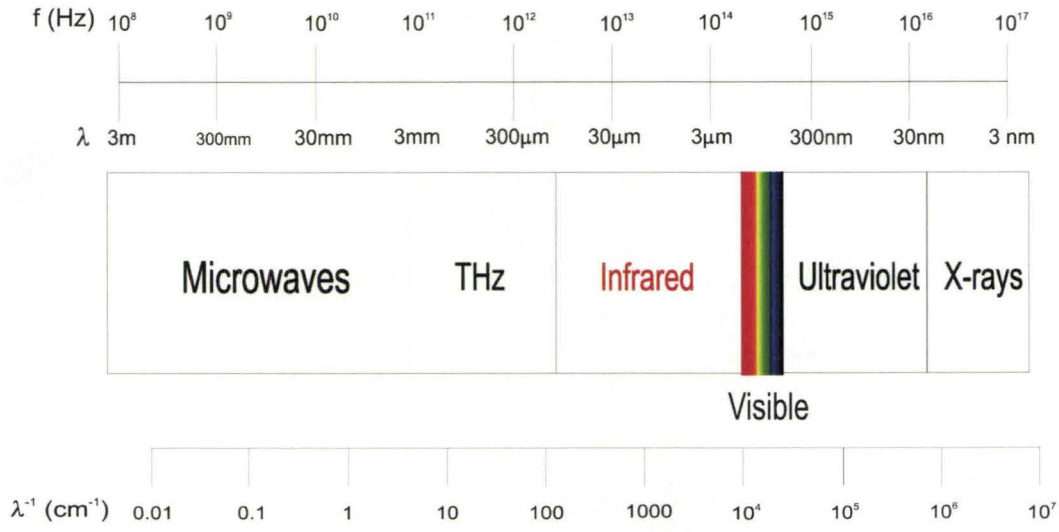

Figure 1.8 Diagram showing the THz region in the electromagnetic spectrum.

1.3.1 THz Generation

In order to gain an appreciation for this spectroscopic technique, an explanation of both the generation and detection of THz radiation is required. We generate our THz radiation using optical rectification by directing 800 nm laser pulses of width 50 fs on to a zinc telluride (ZnTe) crystal. ZnTe does not have inversion symmetry, which makes it a suitable material for the second order non-linear process of optical rectification.[41] There are numerous other techniques for generating THz radiation including: photoconductive antennas,[*42,43] free electron lasers,[44,45] synchrotron sources,[46] optically pumped gas lasers,[47,48] and frequency multipliers.[49,50] Optical rectification is suitable for the purposes of the experiments presented here, as it produces ultra broad band THz pulses.

In order to generate frequencies in the energy region of interest, we require a laser pulse width on the order of 100 femtoseconds. Obtaining such a pulse is a technically complex procedure, but the basic process involves first the creation of a weak 80 fs wide IR pulse followed by its optical amplification. The technical details are described below.

---

[*] Also known as photomixers

A titanium doped sapphire laser provides the seed pulse to be amplified. This laser, commercially available as the Tsunami, is optically pumped by a visible continuous wave (CW) laser which is in turn pumped by a diode laser. The Tsunami produces 80 fs pulses at a wavelength of 800 nm when it is mode locked. The average power of the pulses is approximately 400 mW. The Tsumani seed pulse is then sent into an optical amplifier, which is referred to as the Spitfire. The Spitfire uses an optically pumped titanium sapphire rod as the gain medium. Before the seed pulse from the Tsunami is amplified it must first be stretched to avoid the self focusing caused by the Kerr effect.[51] In non-linear materials, sufficiently high intensities of light will change the refractive index of the material. This will cause the beam to focus in the material. In this instance it is an undesirable effect, as it can lead to the damage of optical components within the amplifier. To avoid this, the seed pulse is first sent to a diffraction grating. This causes a dispersion of the frequencies in the pulse. This stretching of the pulse is achieved because the bluer frequencies will have a longer optical path length than the redder frequencies as shown in Figure 1.9. Once the pulse is stretched it can be safely sent through the Ti doped sapphire gain medium. Once the pulse is amplified it can be compressed again with a second diffraction grating, as is shown in Figure 1.10.

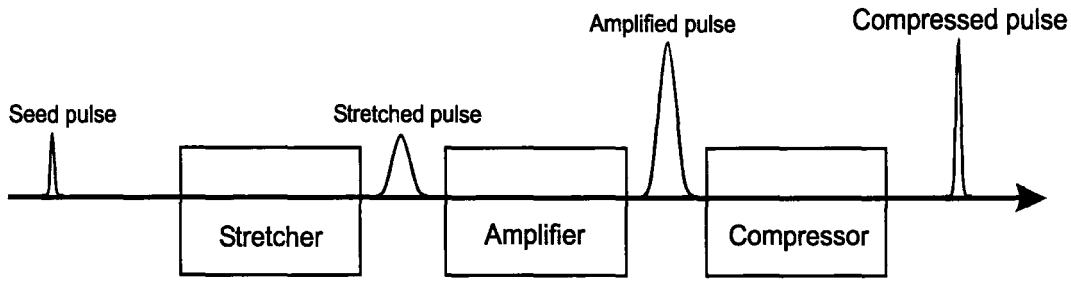

Figure 1.9 Evolution of seed pulse through the amplifier. After the stretcher, the redder wavelengths of the seed pulse lead the bluer frequencies. This allows the amplifier to amplify the seed pulse without damaging the optics.

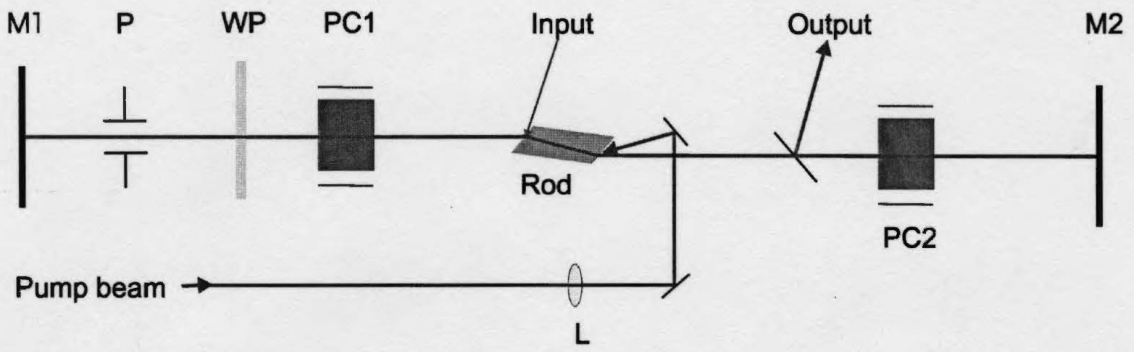

Figure 1.10 Schematic of amplifier: M1 and M2 are the end mirrors, P is a pinhole and L is a lens. WP is a quarter wave plate, PC1 and PC2 are Pockel cells. The rod is a titainium: sapphire gain medium.

The titanium doped sapphire rod is optically pumped by a Nd doped YLF laser, called the Merlin. The light from the Merlin has a wavelength of 527 nm at a power of 4 W. Timing is very important in the optical amplifier. There are two Pockels cells that are used to control the timing of the amplification of the seed pulses with respect to the optical pumping of the Ti:Sapphire rod. The Pockels cell consists of a non-centrosymmetric crystal. When no voltage is applied to the cell, the light passes through the crystal without any change in polarization. Between the first Pockels cell and the end mirror, there is a quarter wave plate. If the first Pockels cell (PC1 in Figure 1.10) is off, then the light will experience a $\lambda/2$ rotation, as it passes through and is reflected back at the $\lambda/4$ wave plate. The pulse will then pass through the Ti:Sapphire rod, undergoing a small amplification. It will then pass through the output polarizer (P1) and into the second inactive Pockels cell (PC2). It will pass through this cell unchanged as well, and then reflect back through the polarizer and the rod. As the pulse passes through the inactive input Pockels cell and quarter wave plate again, the light will be converted back to its original polarization. When it reaches the rod, it will reflect back out of the resonator chamber because the rod will not transmit light of that polarization. Thus, while PC1 is off, the seed pulses will be rejected. The PC1 can be used to ensure that the timing of the amplification of the seed pulse coincides with the optical pumping of the rod. The first Pockels cell is triggered to turn on when a pulse from the Merlin has

optically pumped the Ti:Sapphire rod. PC1 is activated after the seed pulse has left it and is traveling towards the rod. Once it is activated it acts as a quarter wave plate and serves to negate the effects of the wave plate. In this state, the output polarizer will allow the pulses to pass through them. As long as PC1 is on, and PC2 is off, the seed pulse is trapped in the resonator. After several passes through the Ti:Sapphire rod (~ 10^6 amplification), the second Pockels cell is activated. When the pulse passes through the cell twice, it experiences a $\lambda/2$ rotation in polarization. Thus, when the pulse reaches the polarizer, it is reflected out of the resonator chamber and into the chamber containing the compressor.

Once the pulse enters the compression chamber, a diffraction grating is used to compress the beam by causing the "bluer" frequencies to have a shorter path length than the "redder" frequencies. This shortens the amplified pulse. Typical pulse widths are 50 fs. The pulse can then be used to for THz spectroscopy.

The ultrafast laser pulse is sent to a nonlinear non-centrosymmetric crystal, such as <110> ZnTe where it creates a transient polarization.[52] The transient polarization in turn generates an electromagnetic pulse for frequencies ranging from $1\text{x}10^{11}$ to $3\text{x}10^{12}$ Hz as seen in Figure 1.11.

From Maxwell's equations we can see that the polarization is a source for an induced electric field:

$$\begin{aligned} \nabla \times E &= -\mu_0 \frac{\partial H}{\partial t} - \mu_0 \frac{\partial M}{\partial t} & \nabla \times H &= \varepsilon_0 \frac{\partial E}{\partial t} + \frac{\partial P}{\partial t} + J \\ \nabla \cdot H &= -\nabla \cdot M & \nabla \cdot E &= -\frac{1}{\varepsilon_0} \nabla \cdot P + \frac{1}{\varepsilon_0} \rho \end{aligned} \qquad \textbf{1.10}$$

P=polarization (positions of bound charges)

M=magnetization (motion of bound charges)

J= current density (motion of free charges)

ρ= charge density (positions of free charges)

In a dielectric medium,

$$\begin{aligned} \nabla \cdot H &= 0 \\ \nabla \cdot E &= 0 \end{aligned} \tag{1.11}$$

The inhomogeneous wave equation for the induced THz light can be derived from Maxwell's equations:

$$\begin{aligned} \nabla \times \nabla \times E_{THz} &= -\mu_0 \nabla \times \left(\frac{\partial H}{\partial t} \right) \\ \frac{\partial}{\partial t}(\nabla \times H) &= \varepsilon_0 \frac{\partial^2 E_{THz}}{\partial t^2} + \frac{\partial^2 P^{NL}}{\partial t^2} \end{aligned} \tag{1.12}$$

where P^{NL} is the non-linear polarization. Substituting for $\nabla \times \left(\frac{\partial H}{\partial t} \right)$ gives:

$$\nabla(\nabla \cdot E_{THz}) - \nabla^2 E_{THz} = -\frac{1}{c^2} \frac{\partial^2 E_{THz}}{\partial t^2} - \mu_0 \frac{\partial^2 P^{NL}}{\partial t^2} \tag{1.13}$$

Which is the familiar inhomogeneous wave equation:

$$\nabla^2 E_{THz} - \frac{1}{c^2} \frac{\partial^2 E_{THz}}{\partial t^2} = \mu_0 \frac{\partial^2 P^{NL}}{\partial t^2} \tag{1.14}$$

The induced polarization can be written as a Taylor's expansion of the form:

$$P(t) = \chi^{1'} E(t) + \chi^{2'} E(t)^2 \tag{1.15}$$

where χ^1 and χ^2 are the first and second elements of the electric susceptibility tensor, and:

$$E(t) = A(t)\cos(\omega_0 t) \tag{1.16}$$

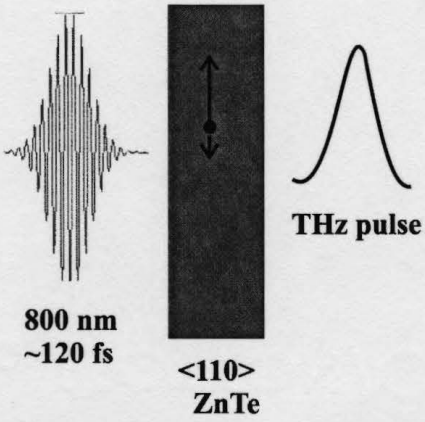

Figure 1.11 An IR pulse arrives at the non-centrosymmetric crystal, <110> ZnTe, and produces a transient polarization which in turn radiates an electric field in the THz region.

where A(t) is the time dependent amplitude and ω_0 is the angular frequency of the radiation. Note that the second term in the expansion of the polarization is present due to the lack of inversion symmetry in the ZnTe crystal. Substituting the specific form for the electric field into the expansion for the polarization leads to:

$$P(t) = \chi^{1'} A(t)\cos(\omega_0 t) + \chi^{2'}\left(\frac{A(t)^2}{2} + \frac{A(t)^2\cos(2\omega_0 t)}{2}\right). \qquad 1.17$$

The first term in the expansion is responsible for the refractive index of the material, while the final term leads to second harmonic generation. The second term leads to a polarization that follows the intensity profile of the optical pulse. For a continuous beam, this term would only result in a static polarization of the crystal, however for an ultrafast optical pulse, this term gives a transient polarization in the material as seen in Figure 1.11. This transient polarization acts as a source for a propagating electro-magnetic pulse. The spectral content of this pulse extends from DC to a frequency roughly corresponding to the inverse of the pulse duration of the original pulse incident upon the crystal. For optical pulses in the range of 50 fs, the maximum frequency is in

the range of a few THz.* This broad spectrum of frequencies contained in a single THz pulse allows for the simultaneously acquisition of time and frequency resolved information. This THz pulse can then be used as a spectroscopic probe for materials.

1.3.2 THz Detection

One of the advantages of transient terahertz spectroscopy is that optical techniques can be applied to directly measure the electric field associated with the THz pulse. This allows for amplitude and phase information to be acquired simultaneously and leads to an excellent signal-to-noise ratio.[53] The technique we employ is based on the effect of the THz field on the optical properties of a second ZnTe crystal via the Pockels effect.

The analyzer crystal is cut along the [110] direction. A schematic of the crystal is shown in Figure 1.12, where the x, y and z axes define the crystallographic directions. Due to rotational symmetry a treatment of the optical properties of ZnTe cut along the [110] direction is equivalent to a crystal cut along $[1\bar{1}0]$. The ZnTe crystal is cubic, and so in the absence of an electric field, its optical properties are isotropic. When the THz radiation, traveling along the z' direction, interacts with the crystal the optical axes are defined by x', y',z'.[54]

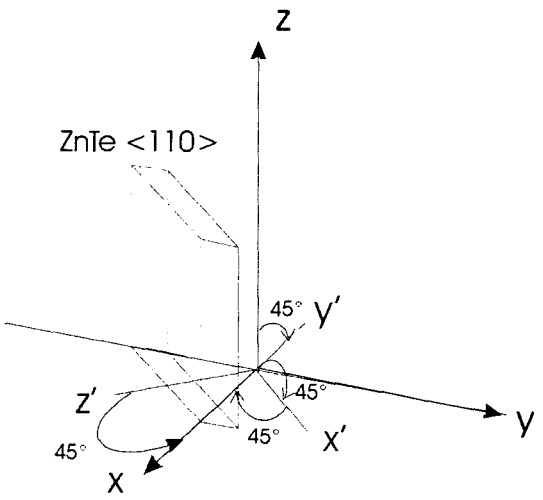

Figure 1.12 Crystallographic axes of the ZnTe detection crystal are labeled x, y and z. Modified axes rotated by interaction with THz radiation are labeled x', y', z'.

$$\begin{aligned}\hat{x}' &= \tfrac{1}{2}\left(\hat{x}+\hat{y}-\sqrt{2}\hat{z}\right)\\ \hat{y}' &= \tfrac{1}{2}\left(\hat{x}+\hat{y}+\sqrt{2}\hat{z}\right)\\ \hat{z}' &= \tfrac{1}{2}\left(\hat{x}-\hat{y}\right)\end{aligned} \qquad \textbf{1.18}$$

The THz radiation is polarized in the x'- y' plane and oriented at 45° to the x' axis. The indices of refraction modified by the THz electric field are then given by:

$$\begin{aligned}n_{x'} &= n_o + \tfrac{1}{2} n_o^{\,3} r E_{THz}\\ n_{y'} &= n_o - \tfrac{1}{2} n_o^{\,3} r E_{THz}\\ n_{z'} &= n_o\end{aligned} \qquad \textbf{1.19}$$

where n_o is the unaltered index of the refraction, r is the electro-optical constant and E_{THz} is the electric field of the THz radiation. It is important to note that the change in $n_{x'}$ and $n_{y'}$ are directly proportional to the magnitude of the electric field. This dependence is equal in magnitude for $n_{x'}$ and $n_{y'}$, but opposite in sign. As a result, the optical response of the ZnTe becomes a direct measure of the electric field passing through it.

Using the response from the ZnTe crystal as a means of detection requires the use of an optical probe beam, referred to here as the IR probe beam. The beam used is a weak 800 nm pulse that is synchronized to the interaction of the THz beam with the analyzer crystal. Due to the Pockels effect, the IR probe beam will experience a change in polarization that is directly proportional to the electric field of the THz pulse. Detecting this change in polarization is accomplished by passing the transmitted IR probe beam through a wave plate followed by a polarizing prism that splits the beam into its two orthogonal polarization components that are individually measured by photodiodes as shown in Figure 1.13.

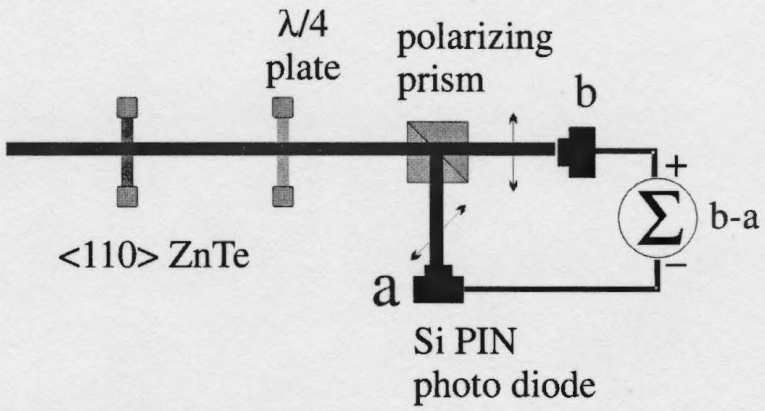

Figure 1.13 Set-up for detecting THz radiation. The horizontal and vertical components of the IR probe beam are detected by photo diodes a and b. In the absence of THz radiation at the ZnTe detector crystal, the IR probe will be circularly polarized and the difference between the signals will be zero. When THz arrives at the detection crystal coincidently with the IR probe, it will change the index of refraction of crystal and in turn change the polarization of the IR probe pulse leading to a non-zero output from the photo diodes.

The 800 nm IR probe beam, incident upon the ZnTe analyzer, of thickness ℓ, is polarized in the $\hat{z}$ direction. The electric field of the analyzer beam can be expressed in terms of the modified optical axes of the ZnTe:

$$\vec{E}'_{800} = \frac{\sqrt{2}}{2} E_o \left[-e^{-i(\omega t-\phi)} e^{i\vec{k}\cdot\vec{r}}\, \hat{x}' + e^{-i(\omega t-\phi)} e^{i\vec{k}\cdot\vec{r}}\, \hat{y}' \right] \qquad \textbf{1.20}$$

where φ is the phase. The change in the indices of refraction of the ZnTe, due to the electric field of the incident THz pulse, introduces a change in the phase for the x' and y' components of the weak IR probe beam such that,

$$\vec{E}'_{800} = \frac{E_0}{\sqrt{2}} e^{-i(\omega t)} \left[-e^{-i\frac{\pi}{\lambda}\ell n^3 r E_{THz}}\, \hat{x}' + e^{i\frac{\pi}{\lambda}\ell n^3 r E_{THz}}\, \hat{y}' \right]. \qquad \textbf{1.21}$$

The IR probe beam is then sent through a quarter wave plate, which causes the light to become elliptically polarized. A polarizing prism then splits the elliptically

polarized light into its $\hat{z}$ and $\hat{x}+\hat{y}$ components and these two components are detected with the photodiodes "a" and "b" respectively (see Figure 1.13). The signals from the individual diodes are then electronically subtracted. A null signal is obtained when THz radiation is absent as the 800 nm probe incident upon the polarizing prism is circularly polarized resulting in two equal components. When a THz signal is present the IR probe beam's polarization state will be altered resulting in a finite signal that is directly proportional to the electric field of the transmitted THz pulse.

1.4 THz Pump-Probe Spectroscopy

Terahertz transmission spectroscopy takes advantage of the spectrally broad THz pulse to obtain frequency dependant information about the sample under study. Figure 1.14 shows the THz pump-probe set-up. Three optical pulses are required, one to excite the sample into a non-equilibrium state, a second to generate the THz radiation and a third to detect the THz field. In our experiment, there are variable delay lines for both the optical excitation pulse and the IR probe pulse. The pulse used to excite the sample is split off first, passed through a delay line, and then focused onto the sample. The size of this optical excitation pulse at the sample is approximately 5 mm^2, slightly larger than the area of the THz pulse at the focal point.

A small portion of the remaining optical beam is split off to be used to analyze the THz beam. The remaining optical energy is directed at a ZnTe crystal and used to create the THz radiation. This radiation is collected and focused onto the sample using parabolic mirrors. THz radiation exiting the sample is then recollected and focused onto a second ZnTe crystal that is used in the detection set-up. The IR probe beam travels through a variable delay path and is directed at the ZnTe analyzer crystal. The THz pulse width is on the order of picoseconds, while the IR probe is approximately 50 fs wide. This allows the IR probe beam to be used to take a "snapshot in time" of the value of the electric field associated with the THz pulse as it passes through the ZnTe crystal. Thus, by varying the IR probe beam's delay path, (labeled as τ_β in Figure 1.14) the overlap

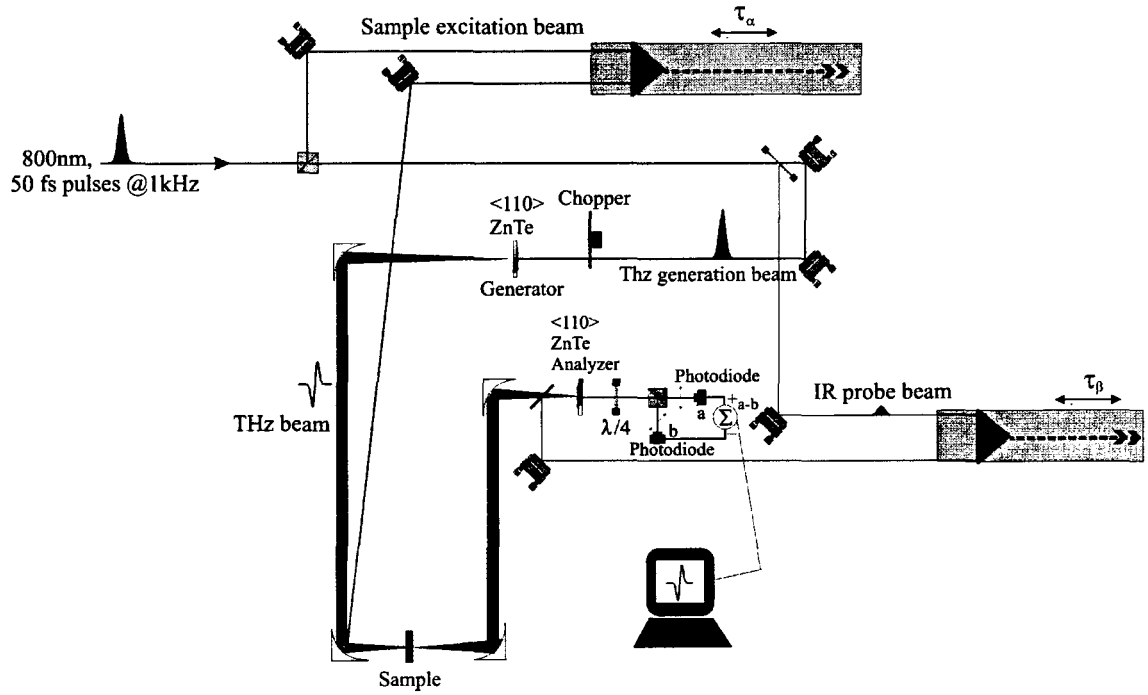

Figure 1.14 THz spectroscopy set-up in the photonics lab at McMaster

will be varied such that the entire transmitted THz pulse is mapped out. The delay associated with the sample excitation beam is also varied. This delay line, (labeled τ_a in Figure 1.14) controls the timing of the arrival of the sample excitation pulse to the sample. The IR pulse contains photons that are very energetic (~1.5eV) compared to the electronic processes within the sample. Thus, the IR pulse highly excites the sample, putting it into a non-equilibrium state. Changing τ_a allows for the THz to probe the sample at various stages of the electronic excitation by having the THz pulse arrive before, during or after the sample excitation pulse, thus allowing the transmission of THz to be determined as a function of time.

1.5 Timescales associated with pump-probe experiments

Superconductors simultaneously exhibit both metallic behaviour and behaviour associated with gapped electronic states. As a result it is useful to consider the response of metals and semiconductors to optical pulses before considering the dynamics of superconductors. A metal can be thought of as a sea of electrons, with energy levels closely spaced to create a continuous energy spectrum. The absorption of light by a metal can be reasonably approximated as a direct single electron process in which the energy of a photon is completely transferred to an electron - promoting it by an energy equal to $\hbar\omega$[55] (see Figure 1.15). As a result, a short intense optical pulse can produce a highly non-equilibrium state. The description of the recovery towards equilibrium depends upon several timescales. In a metal the shortest timescale is associated with electron-electron scattering, denoted by the scattering time $\tau_{e\text{-}e}$. On timescales longer than $\tau_{e\text{-}e}$ the energetic distribution of electrons can be described as an electronic temperature elevated above the lattice, or phonon temperature. Over a somewhat longer timescale, electron-phonon scattering, denoted by $\tau_{e\text{-}ph}$, describes the relaxation of the

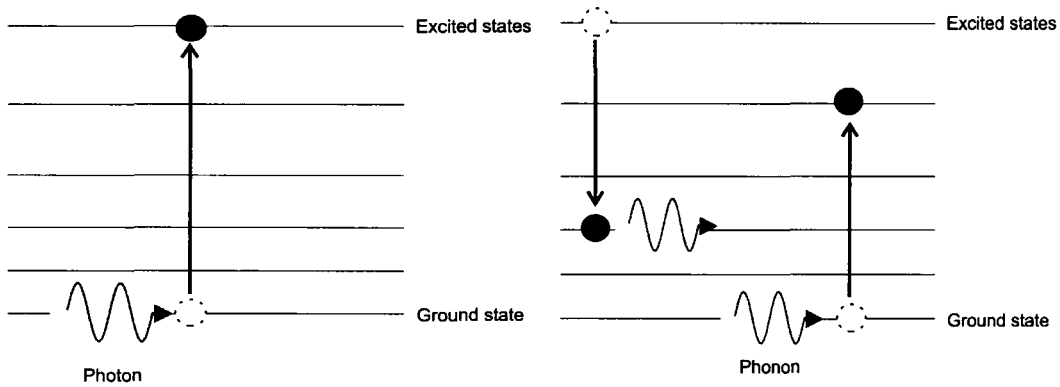

Figure 1.15 The optical excitation and recovery of electrons in a simple metal. On the left: at t=0 the laser pulse arrives at the film and the photons excite the electrons out of the normal state. On the right: Hot electrons cool, giving off phonons. These phonons excite electrons into higher states, slowing the recovery of the electronic temperature. Some phonons contribute to raising the lattice temperature.

electronic temperature towards the lattice temperature. Through this process, a new local temperature above the original ambient temperature is eventually established. Finally the phonons escape out of the metal and into the substrate. The timescale for this process, denoted by τ_γ determines the timescale for the relaxation of the local temperature towards the ambient temperature. This is illustrated in Figure 1.16.

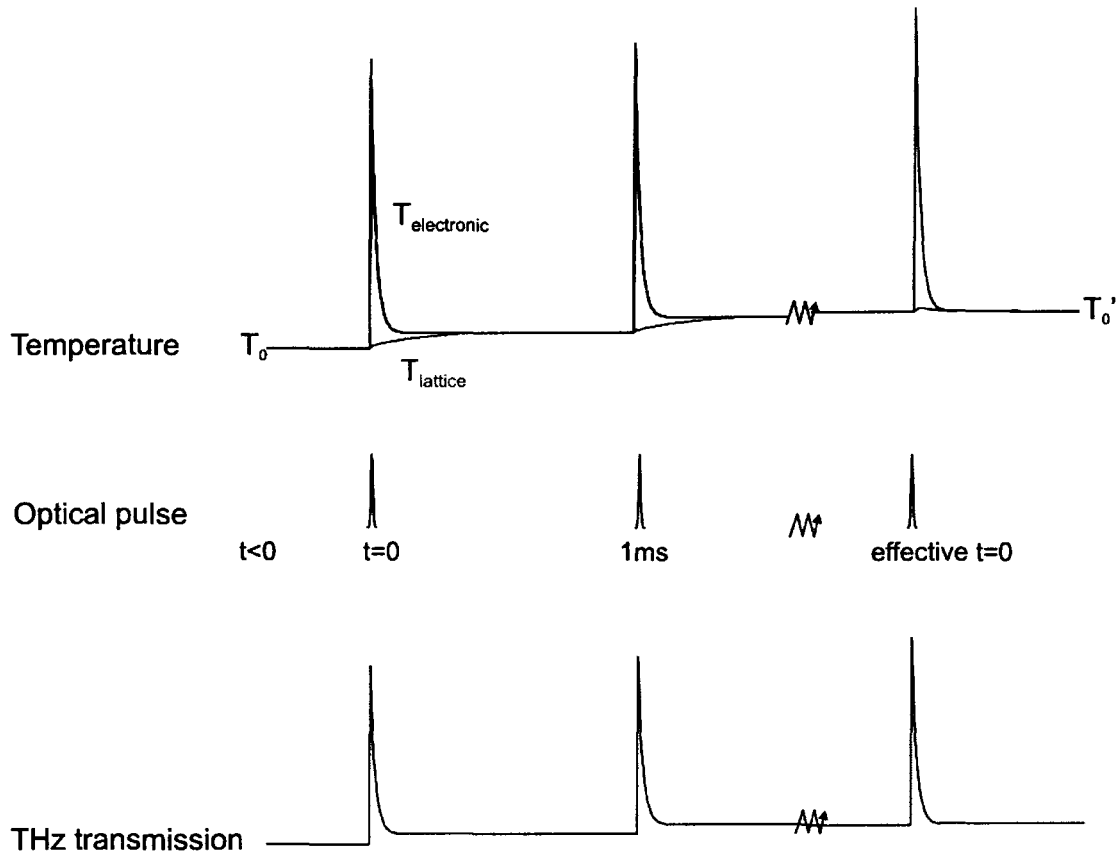

Figure 1.16 The top curve in dark blue represents the electronic temperature. The light blue curve underneath represents the lattice temperature, which is affected less dramatically by the optical excitation. The green curve represents the THz transmission of the metal. After many pulses (after the zigzag), the ambient temperature of the sample reaches a new slightly higher T_0, shown here as T_0'.

In a terahertz transmission experiment carried out on a metal, it is the low-frequency, Drude-like conductivity that determines the transmission. As a result, the transmission will reflect the evolution of the electronic temperature. The degree to which the electronic temperature is perturbed by the optical pulse depends upon the electronic specific heat of the metal. For metals with a relatively low density of conducting electrons the electronic temperature will experience a much larger perturbation.* As a result, a single pulse of light will transiently increase the THz transmission of a metal† with a rapid initial recovery as the electronic temperature equilibrates with the lattice temperature. This is followed by a much slower recovery as the sample temperature cools to the ambient temperature. It is not however, feasible to measure the response of a material to a single optical pulse. Thus, the terahertz transmission experiments in this thesis are carried out by repetitively exciting a sample by optical pulses to allow the sampling of the transmission at different stages of recovery. Under these conditions the sample does not recover completely to the original ambient temperature. Such repetitive experiments are, therefore, a close equivalent to a single pulse experiment at an elevated temperature.

Next let us consider the dynamics of a semiconductor (Figure 1.17). Unlike a typical metal, the conductivity of a semiconductor decreases as the temperature is lowered. This stems from the conductivity, which relies on the populations of electrons in the conduction band and holes in the valence band.[56] At T = 0 K, a semiconductor is an insulator as the conduction band is empty while the valence band is completely filled. The response of a semiconductor to light depends upon the energy of the photons. For photons with energies less than the band gap between the valence and conduction bands, the semiconductor will be transparent. For photon energies greater than the band gap, each photon will excite an electron out of the valence band and into the conduction band. These excess carriers will raise the conductivity of the material and in a THz transmission experiment this will be observed as a decrease in transmission. The recovery of the

---

* Of course the cuprate superconductors in their normal state have relatively low electronic specific heats.
† Since the conductivity of the metal decreases with increasing temperature.

electronic system must take part in two stages. First the hot electrons must cool to the lowest states in the conduction band through collisions and by emitting phonons, as shown in Figure 1.17. If the original photon delivered more than twice the band gap energy to the electron, then collisions can produce an avalanche effect that excites additional electrons out of the valence band. This process is known as impact ionization. Over the timescale of the electron-phonon scattering time, the electrons and holes will come into thermal equilibrium with the lattice. This process is complicated by the number of electron-hole pairs, which will typically be in excess of the number expected for a semi-conductor in equilibrium at an equivalent elevated temperature. This distribution can be modeled by assuming non-equilibrium quasi-chemical potentials for

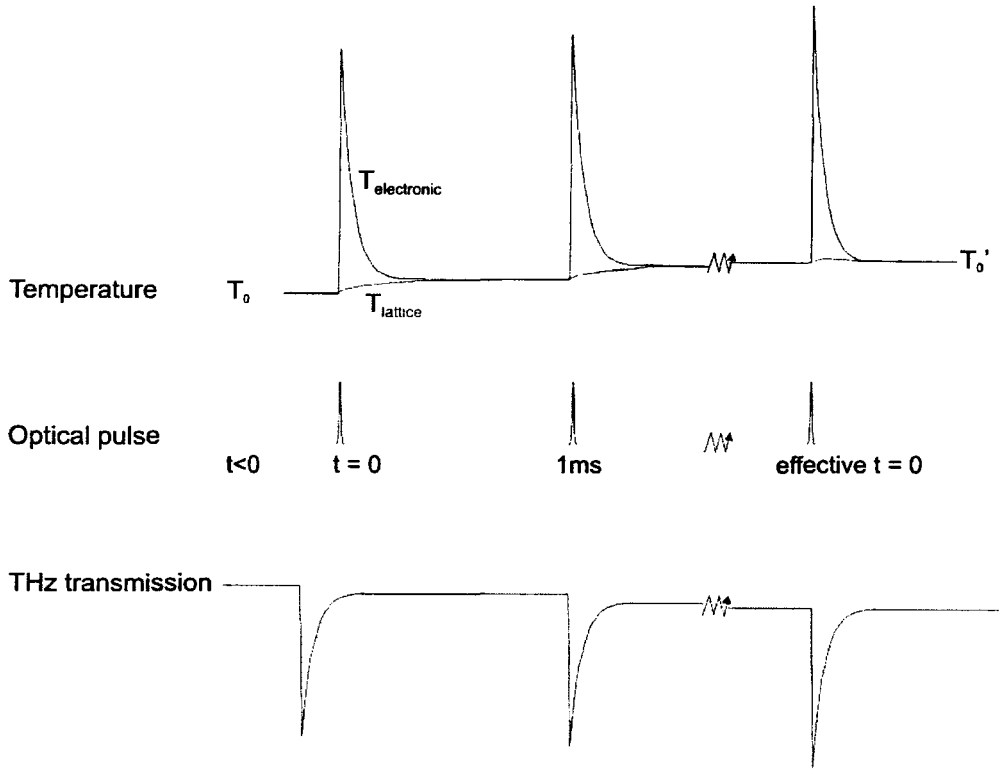

Figure 1.17 A schematic of the electrodynamics of a semiconductor. The recovery of the electronic temperature, shown in dark blue, and the lattice temperature, shown in light blue is much slower than for a metal. This is due to the presence of the semiconducting gap. Another noteworthy difference is in the transmitted THz power, shown in green. Because the conductivity of a semiconductor relies on the population of the electrons in the conduction band and holes in the valence band, the transmission decreases with increasing electronic temperature.

the carriers.* As electrons and holes recombine these quasi-chemical potentials equilibrate to eventually become a single chemical potential.

It is also possible for the phonons to be pushed out of equilibrium. This may happen when highly energetic electrons couple strongly to high energy optical phonon modes. In some cases these optical modes have a relatively slow decay into lower energy acoustic modes and thus the electronic system is maintained at an elevated temperature. This occurrence is referred to as a phonon bottleneck.[57]

The electrodynamics of a superconductor have important contributions from both the real† and imaginary‡ components of the conductivity. Within a two-fluid picture, the real part of the conductivity is associated with the normal electrons. Unlike a metal, the imaginary part of the conductivity is significant. Below the transition temperature the conductivity is dominated by the imaginary part of the conductivity. This is not surprising, as the superconducting condensate is largely responsible for the imaginary part of the conductivity. With decreasing electronic temperature, the fraction of carriers in the condensate increases, leading to an increase in the imaginary conductivity and a decrease in the real component of the conductivity.

In an ideal s-wave superconductor the gap is independent of direction in k-space and the magnitude of the gap decreases with increasing temperature as is seen in Figure 1.2. When exposed to optical excitation, the Cooper pairs that make up the condensate will be broken and the resulting quasiparticles will be excited to high energies (Figure 1.18). The destruction of the superconducting condensate dramatically reduces the conductivity so that, as was in the metallic case, at $t = 0$ a sharp rise in the transmitted THz power is observed.[58] Similarly to a semiconductor, the relaxation of the highly excited quasiparticles can break more Cooper pairs, ejecting them out of the superconducting state through impact ionization. As a result of this avalanche process it is likely that significantly more than one Cooper pair will be broken for each incident

---

* Relative to the initial chemical potential, the electron quasi-chemical potential will be displaced towards the conduction band while the hole quasi-chemical potential will be displaced towards the valence band.
† In phase with the electric field.
‡ Out of phase with the electric field.

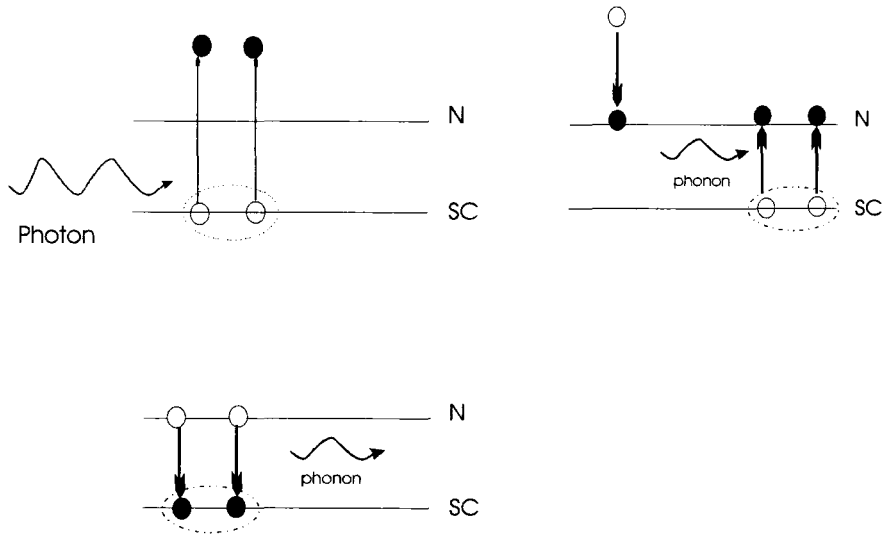

Figure 1.18 Top left: An optical photon excites a Cooper pair out of the superconducting state, labeled SC. Top right: Looking at an excited quasiparticle, it returns to the lowest energy state in the normal regime by giving off a phonon, which in turn excites a Cooper pair out of the superconducting condensate. Bottom: The Cooper pairs reform by giving off a phonon of energy 2Δ.

photon. The excited carriers will thermalize through electron-electron and electron-phonon processes. However, the final recovery of the condensate ultimately requires a pair of quasiparticles to reform into a Cooper pair somewhat analogous to recombination in a semiconductor. Finally phonons with energies of 2Δ or more can be produced both during the initial thermalization of the quasi-particles or during the Cooper pair reformation process. Both the Cooper pair reformation process and possible phonon-bottleneck effects can slow down the recovery of the superconducting condensate.

The net result of the discussion above is that the recovery of the transmitted THz power is slower in a superconductor than in a normal metal. As a superconductor is metallic above Tc, this comparison is observable within one sample. Within a few picoseconds following excitation, the quasiparticles have thermalized to a region in the vicinity of the superconducting gap.[32] We can then use the THz radiation to follow the decay of these excess quasiparticles as the Cooper pairs reform and the condensate is

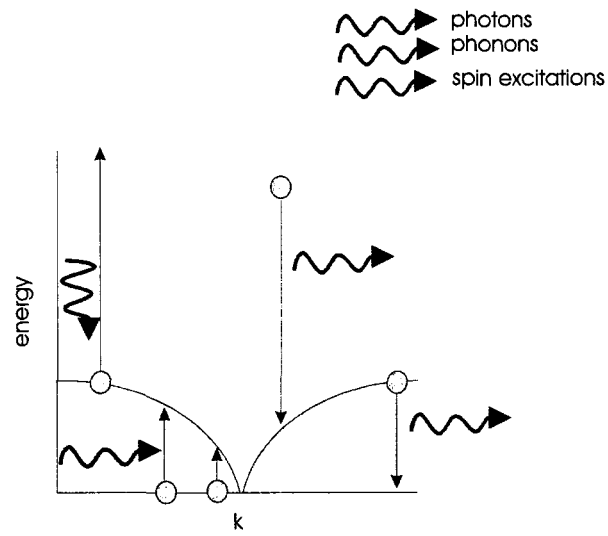

Figure 1.19 This schematic shows the many processes that can occur in a d-wave superconductor. The yellow region represents the d-wave gap.

restored. Excess phonons can lead to a phonon bottleneck, delaying the reformation of the condensate.[59,60,61,62]

For d-wave superconductors such as the cuprates, the process above is complicated by the fact that the value of the gap varies with direction in momentum space, as seen in Figure 1.19. The process where phonons* break Cooper pairs is enhanced in momentum directions where the gap goes to zero.† Additionally, it is not merely phonons that can be generated during the relaxation process as seen in Figure 1.19. This process generally only takes a few picoseconds until the electronic and lattice temperatures equilibrate. Of course the full recovery of the sample to the initial temperature requires the transport of all the deposited energy out of the irradiated region. In our experiments, this timescale is longer than the repetition time of the laser. This leads to a small but significant rise of the effective ambient temperature of the sample.

---

* This refers mainly to phonons created through the relaxation process of excited quasiparticles.
† In an s-wave superconductor, the energy of the phonon must exceed twice the gap energy to destroy superconductivity.

1.6 Introduction to optical conductivity and the thin film approximation

In order to understand the dynamics of the superconducting state in a superconducting thin film it is not sufficient to study only the transmitted THz power. The transmitted power can give an indication of the time-scale of recovery of the film, but it gives no spectral information. Both the superconducting state and the normal states contribute to the change in transmissivity due to optical excitation. Without spectral information, it is difficult to separate the recovery of the superconducting condensate from the relaxation of the normal state. The superconducting state exhibits a well defined $1/\omega$ dependence of the imaginary part of the imaginary conductivity. With this spectral information it is possible to further probe the recovery of the superconducting condensate. In this section I will derive the optical conductivity from the transmission through thin films and discuss the characteristics of the optical conductivity for a superconductor.

The optical conductivity should give insight into the behaviour of both the normal and superconducting states. We can obtain the optical conductivity directly from the transmission using the film approximation for the optical conductivity taken from Tinkham [63]

$$\sigma = \frac{(n+1)}{Z_0 d}\left(\frac{1}{t} - 1\right) \qquad \textbf{1.22}$$

where n is the refractive index of the substrate, d is the film thickness, Z_0 is the impedance of free space, and t is the frequency dependent transmitted electric field through the film and substrate normalized by the transmitted electric field through the bare substrate. To use the form of the optical conductivity described by Equation 1.22 the film must be thin enough that $\frac{n_f \omega d}{c} << 1$. This restriction will be addressed later in the derivation.

First a theoretical expression for the transmission through the film must be determined. Taking into account multiple reflections the transmission of the electric field through the film to the substrate is given by[64]:

$$\frac{E_0}{E_3} = \left(\frac{t_{12}t_{23}}{1 + r_{12}r_{23}e^{\frac{2in_f\omega d}{c}}} \right) e^{\frac{in_f\omega d}{c}} \qquad \textbf{1.23}$$

where t_{ij} is the Fresnel transmission coeffiecient describing the transmission from medium i to j and r_{ij} is the Fresnel reflection coefficient. These are defined as:

$$t_{ij} = \frac{2n_i}{n_i + n_j} \qquad r_{ij} = \frac{(n_i - n_j)}{n_i + n_j} \qquad \textbf{1.24}$$

where n_i is the index of refraction in medium i. Substituting these coefficients into equation 1.23 and where n_f is the index of refraction of the film and n is the index of refraction of the substrate yields:

$$\frac{E_0}{E_3} = \frac{\left(\frac{2}{1+n_f}\right)\left(\frac{2n_f}{n_f+n}\right)e^{\frac{in_f\omega d}{c}}}{1+\left(\frac{1-n_f}{1+n_f}\right)\left(\frac{n_f-n}{n_f+n}\right)e^{\frac{2in_f\omega d}{c}}} \qquad \textbf{1.25}$$

This equation simplifies to:

$$\frac{E_0}{E_3} = \frac{4n_f}{(1+n_f)(n_f+n)e^{\frac{-in_f\omega d}{c}} + (1-n_f)(n_f-n)e^{\frac{in_f\omega d}{c}}} \qquad \textbf{1.26}$$

In order for the thin film approximation to hold, $\frac{in_f\omega d}{c}$ must be small, in other words $\frac{n_f\omega d}{c} << 1$. In this scenario, it is valid to use the exponential approximation: $e^{ix} \approx 1+ix$ in equation 1.27, giving:

$$\frac{E_0}{E_3} = \frac{4n_f}{(1+n_f)(n_f+n)\left(1-\frac{in_f\omega d}{c}\right)+(1-n_f)(n_f-n)\left(1+\frac{in_f\omega d}{c}\right)} \quad \textbf{1.27}$$

This equation simplifies to:

$$\frac{E_0}{E_3} = \frac{2}{1+n-\frac{i\omega d}{c}\left[n+n_f^2\right]} \quad \textbf{1.28}$$

Using the relation between the complex index of refraction of a film and its optical conductivity:

$$n_f^2 = 1+\frac{4\pi i\sigma}{\omega} \quad \textbf{1.29}$$

equation 1.28 can be re-written as an expression of the optical conductivity of the film. It is given by:

$$\frac{E_0}{E_3} = \frac{2}{1+n-\frac{i\omega d}{c}\left[n+1+\frac{4\pi i\sigma}{\omega}\right]} \quad \textbf{1.30}$$

Expanded this equation can be written as:

$$\frac{E_0}{E_3} = \frac{2}{1+n-\frac{i\omega d}{c}+\frac{4\pi\sigma d}{c}-\frac{i\omega d}{c}n} \quad \textbf{1.31}$$

Since our films are generally 50 – 100 nm thick, and the THz generated ranges from 0.2 - 2.5 THz, $\frac{\omega d}{c} << 1$, and therefore the approximation can be made:

$$\frac{E_0}{E_3} = \frac{2}{1+n+\frac{4\pi\sigma d}{c}} \tag{1.32}$$

Equation 1.32 describes the electric field of a THz pulse that has travelled through a thin film as it enters the substrate. Taking into account the effect of traveling through a substrate of thickness x:

$$E_4 = \frac{2}{1+n+\frac{4\pi\sigma d}{c}} e^{\frac{in\,\omega x}{c}} \tag{1.33}$$

And the effect of the transmission at the substrate/air interface:

$$E_{transmitted,\,film+substrate} = \left(\frac{2}{1+n+\frac{4\pi\sigma d}{c}} e^{\frac{in\,\omega x}{c}} \right) \left(\frac{2n}{1+n} \right) \tag{1.34}$$

To get the transmission through the film without the substrate, t, equation 1.34 must be normalized by the electric field transmitted field of a bare substrate. The electric field through a bare substrate is given by:

$$E_{transmitted,substrate} = \frac{4n}{(1+n)^2} e^{\frac{in\,\omega x}{c}} \tag{1.35}$$

Normalizing equation 1.34 by equation 1.35 we have:

$$t_{transmitted,film} = \left(\frac{2}{1+n+\frac{4\pi\sigma d}{c}} e^{\frac{in\,\omega x}{c}} \right) \left(\frac{2n}{1+n} \right) \left(\frac{(1+n)^2}{2n} e^{\frac{-in\,\omega x}{c}} \right) \quad \textbf{1.36}$$

which simplifies to:

$$t_{film} = \frac{1+n}{1+n+\frac{4\pi\sigma d}{c}} \quad \textbf{1.37}$$

Solving for the optical conductivity, we get the Tinkham thin film approximation:

(mks)
$$\sigma = \frac{c}{4\pi d}(1+n)\left(\frac{1}{t}-1\right) \quad \textbf{1.38}$$

(SI)
$$\sigma = \frac{(1+n)}{Z_0 d}\left(\frac{1}{t}-1\right)$$

This form for the thin film conductivity facilitates a frequency dependent study of the optical properties of YBCO without the need for Kramers-Kronig extrapolation. The dynamic optical conductivity can be determined by measuring the film at various stages of recovery following optical excitation.

1.7 Summary

In this thesis, the dynamic response of the conductivity for optimally and underdoped YBCO to optical excitation will be probed using THz spectroscopic methods. The fundamental parameters of the optimally doped film, such as the scattering time and penetration depth will be extracted from a fit of the data to the hydrodynamic two-fluid model.

Chapter 2. Previous work and motivations

2.1 Optical properties of cuprates in equilibrium

The intrinsic electronic properties of cuprate superconductors.[65,66,67] are still of significant interest to condensed matter physicists. Of the cuprate superconductors, YBCO and $Bi_2Sr_2Ca_nCu_{n+1}O_{2n+6-d}$ (BSCCO) are the most studied. It is typically presumed that superconductivity in the cuprate materials has a common origin, and it is observed that they share many interesting properties. They can, however, exhibit dissimilar behaviours which are sometimes due to intrinsic electronic properties and sometimes due to the practical aspects of sample preparation.

High quality YBCO thin films can be grown with excellent control of the oxygen doping making them an excellent choice for optical measurements that require samples with large areas. Conversely BSCCO crystals cleave easily, making them ideal for surface sensitive measurements such as scanning tunneling microscopy (STM) and angle resolved photoemission (ARPES). As discussed in the previous chapter, THz spectroscopic techniques specifically probe the conductivity of the sample over a broad range of frequencies below the gap. In YBCO, a broad peak in the conductivity as a function of temperature has been observed in YBCO[32,68,69,70] which stems from a combination of a decreasing scattering rate and a decrease in the normal quasi-particle population decreases below T_c. Below T_c, the imaginary part of the conductivity shows a strong $1/\omega$ dependence, increasing as the condensate grows with decreasing temperature. The quasi-particle scattering rate has been estimated from the conductivity.[39,69,71] Wilke *et al.* concluded that the dielectric function of optimally doped c-axis YBCO ($T_c = 85$ K) is consistent with the generalized two-fluid model. They observed a resonance in the dielectric function below 0.5 THz, which may be attributed to the excitation of a Josephson plasma resonance.[72]

Studies of the optical conductivity of BSCCO by Corson *et al.*[73] indicate that the conductivity does not follow the two-fluid model for THz frequencies. Additionally, it is

not expected that the two-fluid model would be appropriate for underdoped YBCO, as it does not properly account for the pseudogap.[32] However, the steady-state conductivity for optimally doped YBCO can be modeled for any temperature above or below T_c using the temperature dependent superconducting fraction, and the quasi-particle scattering time within the two fluid framework.[74]

2.2 Dynamic optical properties of YBCO and BSSCO

Several techniques have been used to probe the quasi-particle dynamics of YBCO and BSCCO. This chapter will concentrate on three techniques: i) THz emission spectroscopy, ii) optical pump optical probe reflectance spectroscopy, and iii) optical pump THz probe spectroscopy. Each technique has its own strengths and drawbacks. THz emission spectroscopy uses radiation emitted from a superconducting antenna to infer the time-dependent currents that results from optical perturbation, but does not yield frequency resolved information. Optical pump optical probe spectroscopy has the best temporal resolution of the three, but does not directly probe the low frequency conductivity, thus information concerning processes with energies comparable to the gap must be inferred. Optical pump THz probe spectroscopy directly probes energies comparable to the gap energy, and yields both temporal and spectroscopic information about the dynamics of the conductivity, however it has the poorest temporal resolution of the three approaches.[75] However, due to the fact that it is directly measuring quantities of interest, optical pump THz probe spectroscopy is perhaps the best technique for probing dynamics that are slower than a few picoseconds.

2.2.1 THz emission spectroscopy

A significant body of work has concentrated on the dynamics of YBCO as determined by THz emission spectroscopy.[76,77,78,79] In THz emission spectroscopy, the superconducting thin film is patterned into a dipole antenna which is then optically

excited by a probe pulse. The THz frequencies emitted depend upon the initial state of the superconducting antenna. Thus, by controlling the time delay between an initial optical excitation pulse, and the optical probe pulse the lifetimes associated with film recovery can be determined. Tounouchi *et al.*[77] have extensively looked at the THz emission from optically excited cuprate antennas, and from this, reported a quasi-particle recombination time to be on the order of 5 ps.[78] THz emission spectroscopy is limited in that it is difficult to obtain spectral information about the conductivity of the film.

2.2.2 Optical pump optical probe spectroscopy

Previous studies[62,80,81,82] of the dynamic optical response of cuprate thin films to femtosecond optical excitation show the recovery to be two-fold - a fast transient response followed by a slow recovery lasting tens of picoseconds. Prior studies of the dynamic optical conductivity have generally concentrated on early timescales.[81,83] Gedik *et al.*[58] used optical pump optical probe spectroscopy to study the reflectance of underdoped single crystal YBCO. They determined that the decay rate of the optical reflectance of the crystal increased with increasing temperature, and decreased with decreasing intensity of the optical excitation beam. The link between the reflectance change at optical frequencies to the dynamics at much lower energies is not straightforward. Optical techniques indirectly measure condensate dynamics, as they detect the residual effects of changes in the quasiparticles dynamics that persist to high frequencies. Gedik *et al.* note that infrared measurements on YBCO have shown that spectral weight is shifted from the condensate δ function to frequencies on the order of 100 meV,[84] which is a good deal higher than the maximum gap value. The Kramer-Kronig relations can be used to demonstrate that a small tail associated with this spectral weight shift will remain up to 1.5 eV. These considerations also imply that optical probes are insensitive to shifts in the spectral weight between the condensate and low energy nodal quasiparticles.

In another publication from the same group, Sergre *et al.*[62] claim this effect follows two-particle kinetics where strong optical excitations excite the quasi-particles, which leads to a fast component recovery followed by a thermal recovery, whereas in the case of weak optical excitation, the excitation density is smaller than the thermal population, thus slowing the recovery of the crystal. They observe a decay of $\Delta R/R$ that is on the order of a picosecond – much faster than the argued recombination timescale. They reconcile this by arguing that the optical reflectivity measurement is sensitive to a thermalization of the sample, rather than a direct measurement of the quasi-particle recombination.

2.2.3 Optical pump THz probe spectroscopy

As discussed in Chapter 1, the greatest strength of optical pump THz probe spectroscopy is that it can provide temporally resolved spectral information of both the real and imaginary components of the conductivity provided that the processes involved are sufficiently slow. Although typical THz probes cannot match the time resolution of optical reflectance and THz emission techniques, they do have the novel advantage of making accessible the temporal evolution of spectral processes associated with energies directly relevant to superconductivity in the cuprates.[85] A two-component decay similar to the one observed with optical techniques has also been observed using THz probes. Demsar *et al.* observe a plateau at long timescales in the recovery of the imaginary conductivity for optimally doped 50 nm thick YBCO.[86] They postulate that the source of the plateau is an increase in temperature, due to the optical excitation ($F \sim 120\ \mu J/cm^2$), and predict the temperature increase to be 40 K.

The change in optical conductivity of BSCCO at 5 K due to optical excitation at a probe frequency of 1.3 THz was measured by Carnahan *et al.*[87] They observe a two-component decay consistent with other results. They also show that by 60 ps, the imaginary part of the conductivity has not recovered to the initial value observed at equilibrium prior to optical excitation.

Averitt *et al.*[32] have studied the effect of both weak and strong perturbations of the condensate. For an optical pump fluence of 10 $\mu J/cm^2$, the conductivity seems to have fully recovered to the steady-state conductivity of an optimally doped film within 10 ps of optical excitation. However, the fact that the conductivity at 10 ps resembles the steady-state film at the background ambient temperature indicates that the condensate is only weakly perturbed at that fluence. They concluded from a comparison to the recovery of $Y_{0.7}Pr_{0.3}Ba_2Cu_3O_7$ that the slower recovery of the conductivity above T_c was indicative of the pseudogap.

A careful review of the work by Demsar *et al.*[86] and Averitt *et al.*,[32] reveal some interesting anomalies in the frequency dependence of the conductivity during recovery. Averitt *et al.*'s data shows a dip in the imaginary part of the conductivity for an underdoped film (T_c = 50 K) 50ps following excitation. Although only low frequencies are shown, it appears as though the lowest frequencies recover last, which will be shown to agree with the experimental results shown in this thesis. They explain the suppression as a delay in the thermal recovery due to the presence of excess phonons. Demsar *et al.* also show conductivities in which the recovery appears to be frequency dependent.

2.2.4 The role of the phonon bottleneck in dynamic YBCO

When studying longer timescales, an important issue to be resolved in these experiments is the possible role of the phonon bottleneck in delaying the reformation of the condensate.[59,61,62,88] In conventional s-wave superconductors, the gap has a single value. As Cooper pairs reform, the excess energy can generate a non-equilibrium phonon as illustrated in Figure 1.19. This non-equilibrium phonon is capable of breaking a second Cooper pair. As a result, the measured recovery time of the condensate is not necessarily the intrinsic pair formation time, but can be the timescale associated with the removal of excess phonons, in which case the phonon removal rate bottlenecks the process. The phonons can be removed from the process either by anharmonic decay to phonons with lower energy or by propagating out of the sampled volume. Studies have

shown that the relaxation times of single crystal cuprates and films do not vary with film thickness which indicates that if a bottleneck exists it is associated with anharmonic decay.[86]

For d-wave superconductors, any bottleneck process is complicated by the fact that the value of the gap varies with direction in momentum space, as is illustrated in the schematic shown in Figure 1.19. Arguably, the d-wave nature of the gap may mitigate the phonon bottleneck process,[89] as there are more low energy states available for phonon interaction.

In most studies on the cuprates, the dynamics for longer timescales have been considered to be thermalization slowed by the presence of a phonon bottleneck[32,62,80,86] However, the existence of a phonon bottleneck in YBCO has been called into question. Gedik *et al.* report that the dependence of the decay rate seen in $\Delta R/R$ upon the optical pump power indicates that the phonon bottleneck effect is absent in YBCO[89] for their timescales (25 ps). They observe that if a phonon bottleneck were present, one would expect a decay rate that is not dependent upon quasi-particle density.[60] They postulate that cuprates may have a tendency to not form phonon bottlenecks, either because thermal equilibrium is reached after the quasi-particle density decays to a fraction of its initial value or because the time associated with phonon escape is faster than the time associated with pair recombination.

2.3 Experimental Objectives

2.3.1 Understanding the dynamics of YBCO at long timescales

The objective of the research presented in this thesis is to investigate the response of YBCO to optical excitation for energies comparable to the superconducting gap at long timescales. The 800 nm light used to excite the sample has sufficient energy per photon to break Cooper pairs and excite the quasiparticles well above the Fermi energy. One of the relaxation processes available to these highly energetic particles is to break

further pairs through impact ionization. Within a few picoseconds, however, the quasiparticles have thermalized to a region in the vicinity of the superconducting gap. We can then use the film's response to THz radiation to follow the decay of these excess quasiparticles as the Cooper pairs reform and the condensate is restored.

There has been strong debate whether phonons or some other process, such as spin fluctuations, mediate pair interaction in the cuprates. Conversely, most studies of the dynamics following optical excitation have concluded that the slow component of the recovery is purely thermal.[61,81,86] On general grounds, one would anticipate that in the formation of a Cooper pair, the energy would be transferred to the mode responsible for binding the pair together. For example, if the pairing is due to spin fluctuations, then a spinon would be emitted. Based on this consideration, the slow recovery of YBCO bears closer inspection. The spin degrees of freedom raises the potential for new bottleneck processes which would slow the escape of the energy out of the electronic degrees of freedom.

Here we present the long timescale effects of optical excitation for both low power optical excitation and high power excitation. It will be shown that although the time dependence of the THz response of a YBCO thin film at long timescales is consistent with a purely thermodynamic picture, when the low frequency components of the optical conductivity are analyzed a more complex explanation must be sought.

2.3.2 Looking for pre-formed pairs

The origin of the pseudogap in underdoped cuprates is still a matter of debate. If the pseudogap is associated with the formation of uncorrelated pairs, this may be possible to discern via pair breaking. Kaindl *et al.*[90] observed a two component decay to the change in the mid-IR reflectivity* of underdoped YBCO. They suggest that this may be indicative of two pair breaking processes: a 5 ps process which arises from the recovery of the condensate and is only observable below T_c, and a 700 fs process which relates to

* 60-180meV

the recovery of uncorrelated pairs and can be observed up to T* (i.e. the onset temperature of the pseudogap). A spectroscopic analysis of the dynamic THz conductivity of underdoped YBCO above T_c could yield information about the pseudogap[32] if this pair recombination time is not faster than the temporal resolution. It is not expected that a sharp spectral feature would be observed, as the probe energies available are smaller than the pseudogap.[91] Thus, only a broad suppression of the conductivity would be expected. If no spectral signatures indicative of the pseudogap are observed above T_c, then either the recovery process is too fast to capture, or there is no pair breaking.

2.3.3 Inhomogeneity in Cuprates

Cuprates have an intriguing propensity towards the development of spatial structures. Vortices,[92,93,94] stripes,[95,96] and inhomogeneities in the gap[97,98] have been observed. Phase inhomogeneity in underdoped YBCO arising from spontaneous self organization has been predicted by Emery *et al.*[99] and discussed by Demsar *et al.*[83] Evidence of striped conduction phases have been clearly seen in many cuprate systems. It has been suggested[91,100] that the presence of the pseudogap in underdoped YBCO makes these films intrinsically inhomogeneous. In BSCCO, scanning tunneling microscopy (STM) experiments show nanoscale inhomogeneities in the local density of states (LDOS) that are not due to surface defects.[98] Indeed, a study of the effect of impurities on the background inhomogeneity of BSCCO suggests that the inhomogeneities are intrinsic.[97] Lang *et al.* report evidence of granular superconductivity in BSCCO, where microscopic superconducting domains of higher hole concentration manifest in low doped crystals[101]. This would lead to an inhomogeneous material exhibiting two states: superconducting and non-superconducting. Josephson tunneling could couple the domains of superconductivity. Spatial inhomogeneity in the steady-state conductivity of YBCO has been observed with THz imaging techniques by Brucherseifer *et al.*[102]

Based on the tendency towards inhomogeneity in equilibrium, it is reasonable to look for signatures of spatial structure during the recovery of films following optical excitation. If the recovery of the condensate is not spatially uniform, there might be important contribution in the temporal response. Separating such a contribution from a bottleneck process would be problematic. However, since THz probes are also able to extract the frequency content of the conductivity, there is the potential to look for spectroscopic signature of the spatial structure.

Chapter 3. Precision time resolved THz spectroscopy

3.1 Introduction

Until recently, spectroscopy at THz frequencies had been a long standing challenge. THz frequencies lie between the optical and microwave regions of the electromagnetic spectrum, where conventional optical and microwave techniques are both ineffective. New approaches to THz generation and detection became available with the advent of ultra short optical pulses. Generation typically involves the optical generation of a short current pulse which radiates at THz frequencies, while detection involves optical sampling of the electric field associated with the THz radiation. A sample scan is shown in Figure 3.1. It is possible to capture both the transmitted amplitude and phase shift of the THz pulse both with and without the sample. This allows the real and imaginary components of the optical conductivity to be extracted

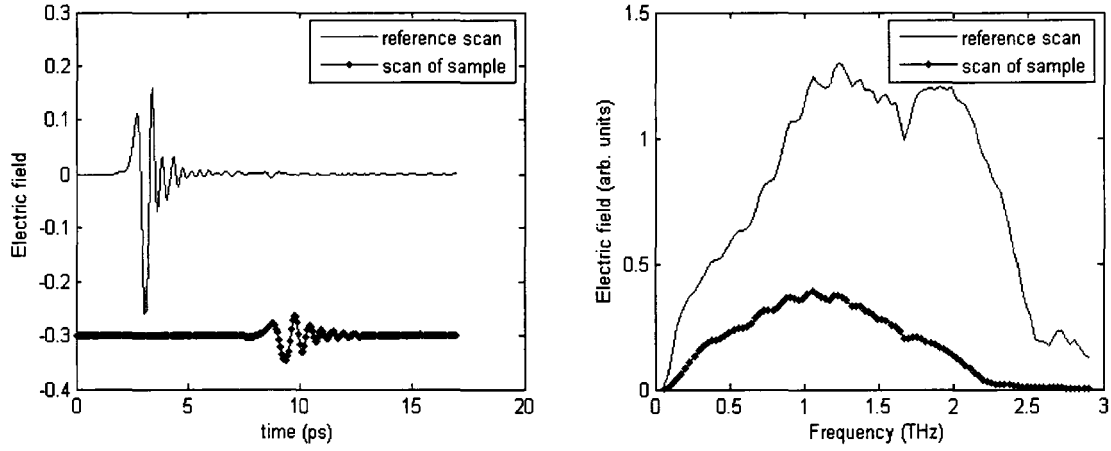

Figure 3.1 a) On the right is shown the measured electric field transmitted through a sample in the time domain. The dotted scan is vertically offset for clarity. Each point in the scan is obtained by changing the delay between the IR detection beam and the THz pulse as it arrives at the detector crystal. The reference scan is shown to illustrate the time delay that is introduced by the sample and substrates's refractive indices. It is the relative time shift, rather than the absolute position of the peak that is interpreted as phase information.
b) On the left is shown the amplitude of the electric field in the frequency domain. This is obtained using a FFT of the raw data in the temporal domain. The sample reflects most of the incident THz pulse, resulting in a weaker amplitude, as can be seen above.

without Kramers-Kronig analysis. These new approaches have had a transformative effect on experimental capabilities at THz frequencies. Now, not only can frequencies spanning the entire THz region be generated and detected sensitively, but the THz radiation is generated as a broadband burst lasting on the order of a picosecond. This offers the tantalizing potential for simultaneously gathering very sensitive spectroscopic and time resolved information.[103]

In this thesis, we will present spectrally resolved information about the dynamics of the recovery of the superconducting condensate following optical excitation using optical pump THz probe spectroscopy. However, this method requires careful consideration of the impact of experimental limitations on analyzed results - in particular avoiding conditions that produce false artefacts. The following sections will discuss the varied experimental considerations, and examine which features of the analyzed data are robust to subtle experimental changes, such as small alterations to the index of refraction of air. Additionally, the long wavelengths involved in THz spectroscopy give rise to many of the same challenges facing microwave spectroscopy. For example, the minimum size of the focal spot is significantly larger than the focal spot of an IR beam, and the long THz wavelengths are capable of leaking around samples if the edges are not sealed. Optically generated THz radiation typically has an extremely broad bandwidth. This means that careful consideration must be given to the alignment and stability of the system, as dispersion of the THz pulse due to optical elements means that the various wavelengths of the pulse will not necessarily follow the same beam path. Perhaps most importantly, care must be taken whenever temporal information is extracted using broad band pulses. Since the electric field is measured in the temporal domain, careful consideration must be given to extracting the frequency dependent transmission for a sample where the optical properties are also changing with time. Finally, since both the detection and generation are tied to the original optical pulse, then the impact of any instabilities in that pulse are magnified in the final result. Indeed much of the work associated with this thesis project has been dedicated to improving and understanding the experimental idiosyncrasies of the THz system at McMaster.

In the following sections three crucial issues in data acquisition and analysis will be discussed. First, the power spectrum obtained from the Fourier transform of the amplitude of the electric field will be investigated. Potential sources of artefacts in the power spectrum are water absorption lines, clipping effects, and sample defects. The effect of humidity can be mitigated by purging the THz set-up with dry N_2. Since the location of the absorption lines are well known, persistent peaks can be filtered at the analysis stage. Clipping can be avoided through proper alignment, and film defects can be identified and avoided through inspection under a microscope. A more insidious issue arises from artefacts due small path length changes in the system between the reference and sample measurements. The phase shift associated with these changes can be erroneously interpreted as real optical properties of the sample. The sources and solutions to these path length changes will be discussed, and it will be shown that the imaginary part of the conductivity of a superconducting film is robust to the introduction of small changes in the path length. Finally, the temporal limitations of a spectrally resolved broadband measurement will be discussed in detail.

3.2 Artefacts in the power spectrum

Spectral artefacts can be caused by a variety of sources. Sharp absorption peaks, like the ones found in water spectra, are especially troublesome as the data is collected in the time domain. Other sources of spectroscopic features are diffraction caused by clipping, and imperfections on the film surface. Optimum alignment will improve the signal-to–noise ratio and reduce the effect of pointing instability. Monitoring laser stability is crucial, as any changes in the system between sample and reference measurement may be interpreted as a real change in the optical properties of the sample. For this reason it is also crucial that the substrate's optical properties be identical for measurements of both the film/substrate and the bare substrate.

3.2.1 Effect of Humidity

Humidity levels are a concern in THz spectroscopy as water exhibits sharp absorption peaks in the THz regime,[104] as shown in Figure 3.2. Water vapour introduces three problems into the data acquisition and analysis: (i) absorption peaks in the frequency domain, (ii) a humidity dependent change in the index of refraction of the air, and (iii) a ringing in the temporal domain. The phase shift due to the changing index of refraction will be discussed in section 3.3, and the effect of ringing on the temporal resolution will be discussed in section 3.4.

The absorption bands of water are strong enough to produce artefacts in the optical conductivity. The frequencies of the absorption lines are well known, and can thus be readily identified and filtered from frequency dependent measurements. It is better, however, to reduce the humidity levels. Figure 3.3 shows the absorption spectrum of water for various levels of relative humidity. The humidity was adjusted through a controlled high purity nitrogen purge. Figure 3.4 shows the Plexiglas box constructed to enclose the THz system for the purge. A latex collar attached to the cryostat fits over the front of the box allowing the cryostat to be translated into the beam without compromising the purge. The relative humidity levels within the box are monitored with a hygrometer.

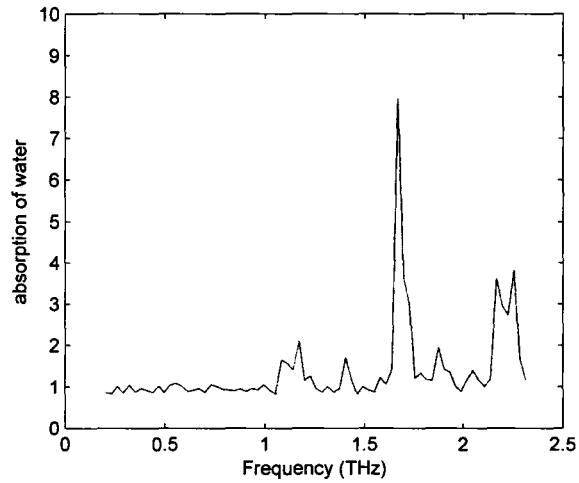

Figure 3.2 Water absorption lines in the THz regime, found taking the ratio of the electric field transmitted through dry air to the electric field transmitted through humid air.

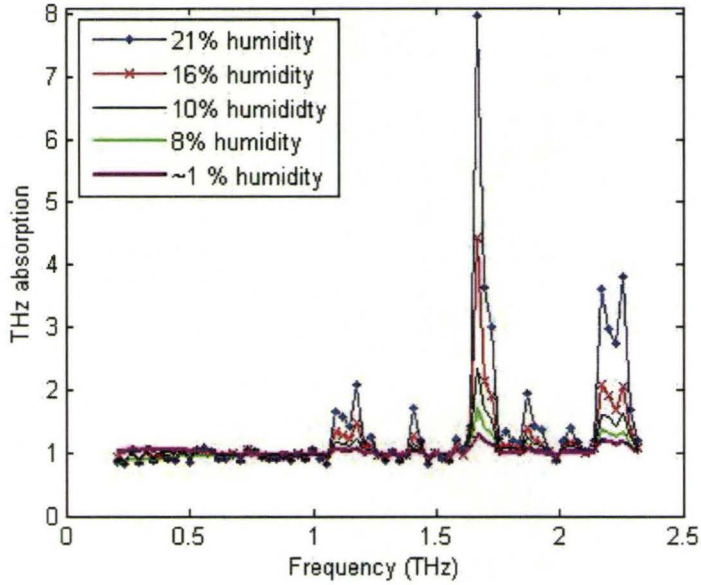

Figure 3.3 Transmission through air for 21-1 % R.H. (relative humidity). Note that the peaks are significantly decreased below 8% R.H.

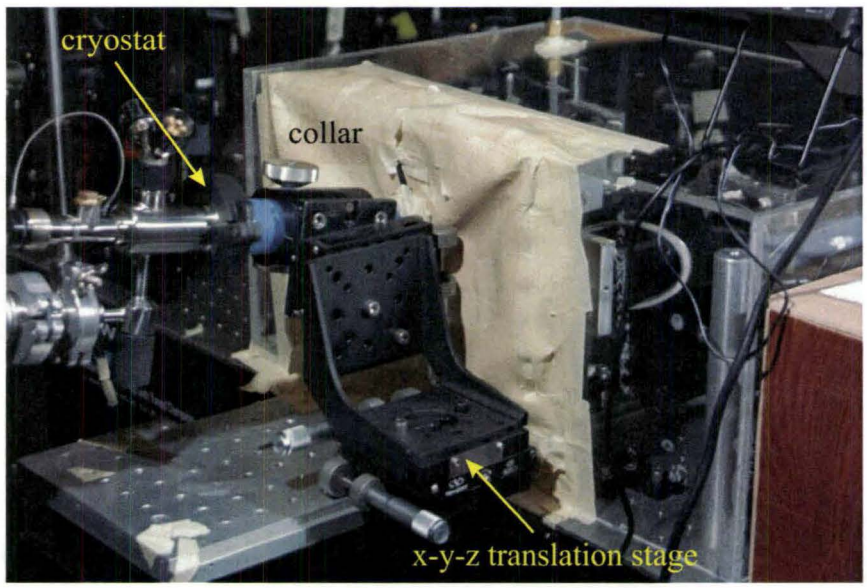

Figure 3.4 A plexiglass purge box is used to control the humidity of the THz set-up. The cryostat is collared with latex, and mounted on an x-y-z translation stage for sample alignment.

3.2.2 Artefacts caused by beam clipping

Time domain THz spectroscopy is particularly prone to spectral artefacts caused by diffraction due to the broad band nature of the THz pulses. This makes any clipping of the beam problematic, as longer wavelengths diffract more than shorter wavelengths, resulting in a THz beam that is not spectrally uniform with higher frequencies located in the centre of the beam, while lower frequencies can be found at the edges. The long wavelengths associated with the THz pulse (ranging from 100 - 1000 μm) limits the focus of the beam, which puts geometric constraints on the system.

3.2.3 Windows

Care must be taken that the windows of the cryostat and the mirrors for the IR probe are as uniformly transparent as possible across all frequencies used so as to avoid the loss of THz power and bandwidth. The window material chosen was 60 μm thick polypropylene as its transmission is relatively high with a spectral response that lacks sharp absorption features. Figure 3.5 shows the THz transmission spectra for light passed through both cryostat windows.

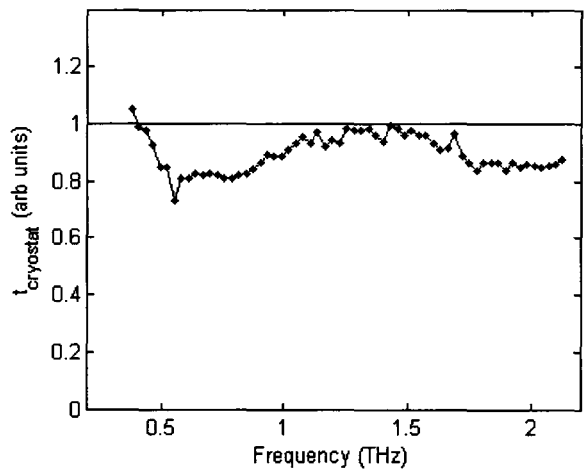

Figure 3.5 Transmission spectrum through two 60 μm thick polypropylene windows.

3.2.3 Cryostat Stability

The cryostat must be kept stable during each experiment to ensure that the sample holder and cryostat windows do not clip the long wavelengths of the THz beam. This is complicated by the significant strain put upon the cryostat by the helium transfer tube. The strains originate from both its mechanical rigidity and the significant thermal contraction which occurs as the transfer tube is cooled. Stability is given to the cryostat by a face plate fitted over the head of the cryostat and then locked into place, as shown in Figure 3.6. The face plate provides enough mechanical stability to allow the transfer tube to be inserted and removed without significantly altering the alignment.

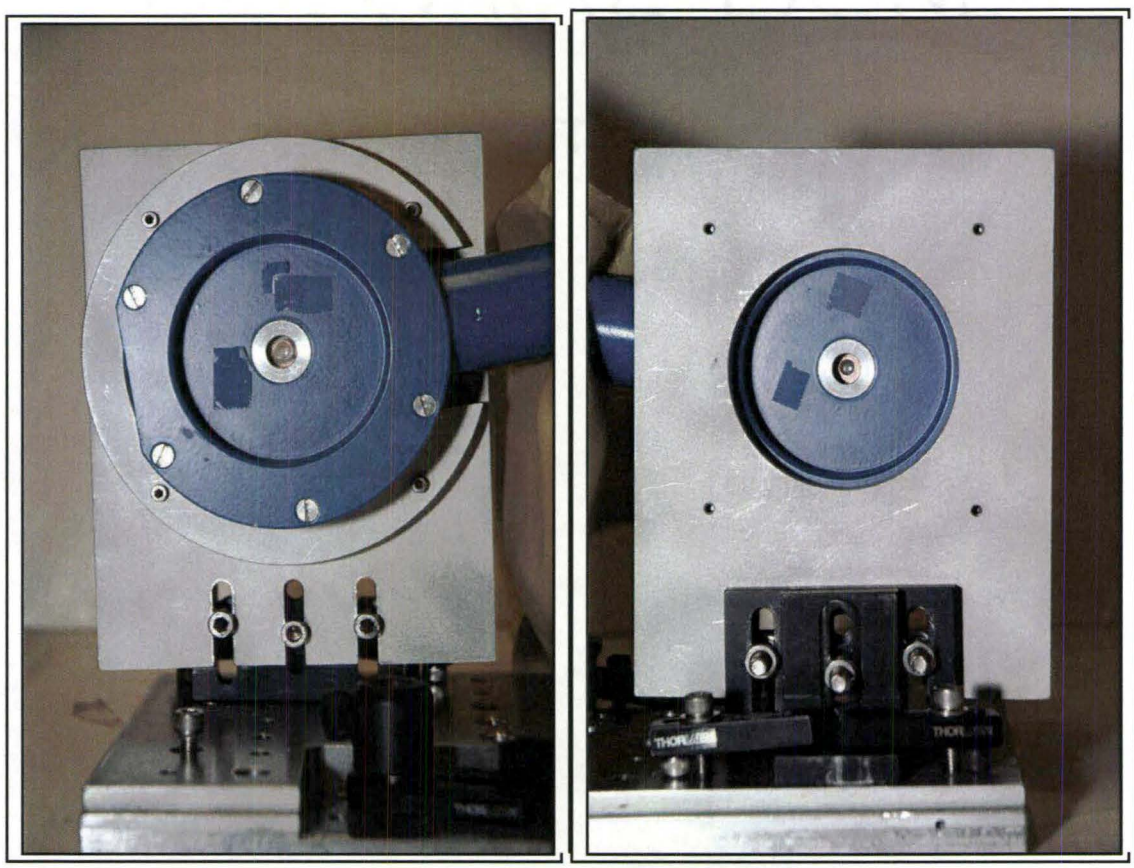

Figure 3.6 A face plate fits around the head of the microstat and screws into place on the optical table to eliminate cryostat motion during experiments.

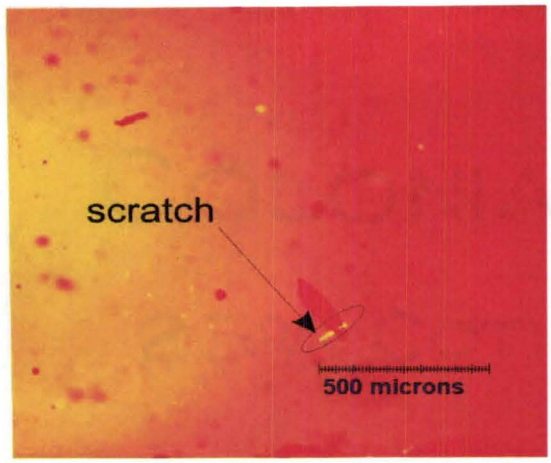

Figure 3.7 Transmission optical microscope image of ~100 μm scratch on YBCO film

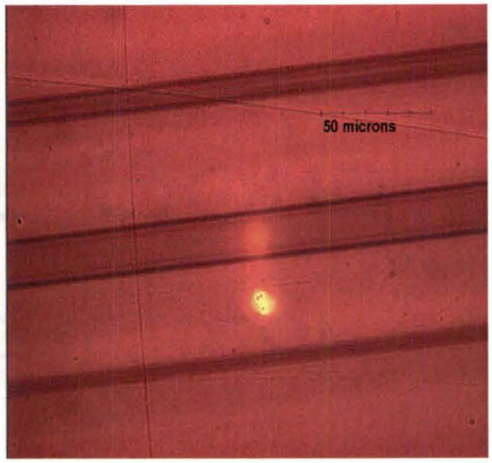

Figure 3.8 Transmission optical microscope image of an ~ 10 μm diameter pinhole. The heavy lines shown are substrate twin boundaries.

3.2.6 Spectroscopic features due to film imperfections:

YBCO thin films are quite susceptible to damage. Thus, it is important to ensure that each measurement is performed on a film that is free of scratches and pinholes. Before each experiment the films were examined for pinholes, scratches and other surface defects using an optical microscope in transmission mode. Figure 3.7 and Figure 3.8 show typical YBCO films containing scratches and pinholes. As it is difficult to deposit a completely pinhole-free film, this section will be devoted to an examination of the effect of pinholes and scratches of various sizes on the transmission of the film.

To study the effect of holes and scratches, a series of samples were made by laser machining lines and arrays of holes through aluminum foil squares, which were then epoxied onto Lanthanum aluminate (LAO) substrates. Since aluminum foil is opaque to THz frequencies, the transmitted signal must be entirely due to the machined defect. Once the spectra is obtained it is then possible to mathematically add the effect of the defect to the spectra from a pinhole–free film in order to mimic the influence a hole has on spectra obtained for a YBCO film. It was concluded that a single hole of typical size* positioned at the focus of the THz spot has an insignificant signal strength, as shown in Figure 3.9 and Figure 3.10.

* <20 μm

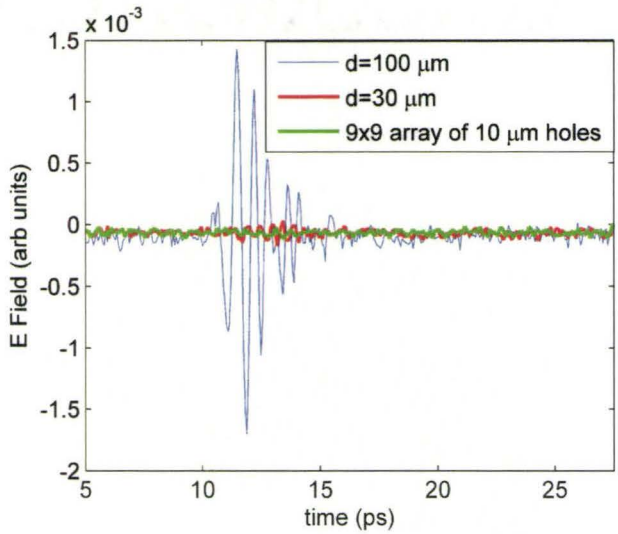

Figure 3.9 Transmission in the time domain of THz radiation through a hole of 100 μm diameter, 30 μm diameter and a 9x9 array of 10 μm holes. Note that the transmission through the 30 μm hole and the array of 10 μm holes is negligible.

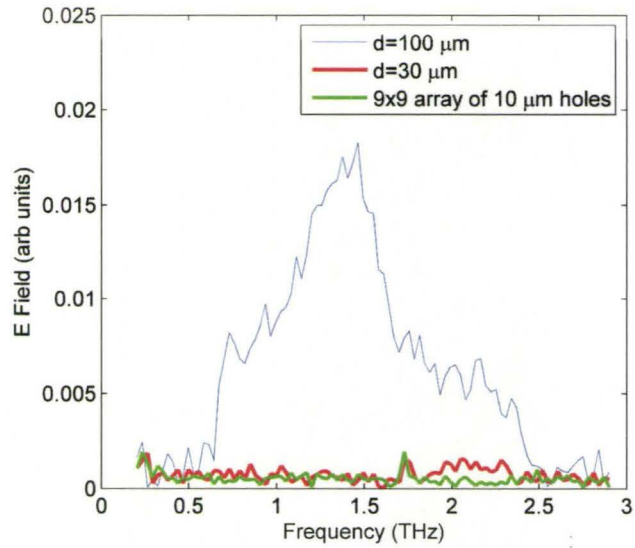

Figure 3.10 Electric field in the frequency domain of THz radiation through a hole of 100 μm diameter, 30 μm diameter and a 9x9 array of 10 μm holes. Again, it can be seen that holes 30 μm and smaller do not have a significant transmission in the THz regime.

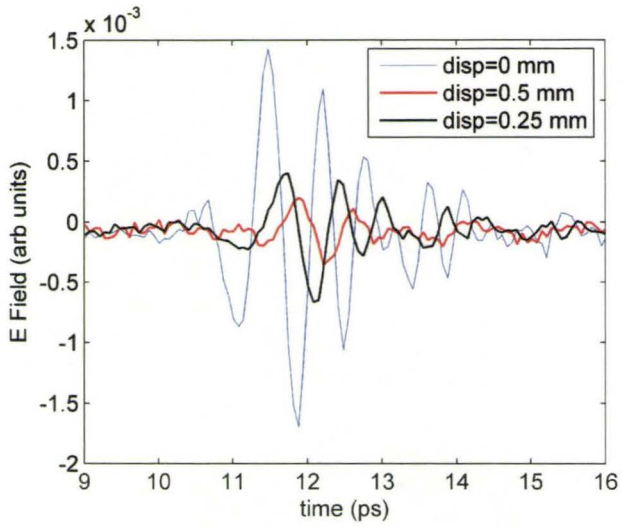

Figure 3.11 Transmission through a 100 μm hole centered on the THz beam and offset from the beam center by 0.5 mm and 0.25 mm. It can be seen that the transmission drops off significantly when the pinhole is not centered on the THz beam.

It can also be seen in these figures that if the hole size is sufficiently small, then the accumulative effect of several holes is negligible. A 9x9 array of ~10 μm holes with a spacing of 500 μm has little impact on the transmission. Figure 3.11 shows that the signal drops off considerably if the hole is not at the centre of the THz spot. At room temperature the effect of pinholes is negligible, but as the temperature decreases the transmission of the YBCO film decreases and any effect of holes or scratches becomes more important.

In order to better gauge the error associated with film defects, the effect of the defects on the optical conductivity must be investigated. This is achieved by adding the experimental results for the transmission through various holes in Al foil to the transmission of an ideal film free from holes. The measured electric field of a film with holes is given by: $E(t)=E_{film+sub}(t)+E_{hole+sub}(t)$. Thus, the conductivity becomes:

$$\sigma' = \frac{n+1}{Z_0 d}\left(\frac{1}{t_{film}+t_{pinhole}}-1\right) \qquad 3.1$$

The transmission of the film in this case is calculated using the Drude model. The Drude parameters were chosen to give a maximum transmission comparable to that of a YBCO thin film at 70 K. Figure 3.12 and Figure 3.13 show the imaginary and real parts of the optical conductivity for the film, and the film with 30 and 100 μm holes mathematically included. From this, it can be seen that the artifacts resulting from a 100 μm pinhole is not negligible, and could not be filtered out. Artifacts resulting from a 30 μm hole, on the other hand, do not seem to appreciably affect the optical conductivity. From this analysis it can be concluded that the effect of the typical pinhole[†] can be safely ignored, and that any film with a hole in excess of 30 μm should be discarded.

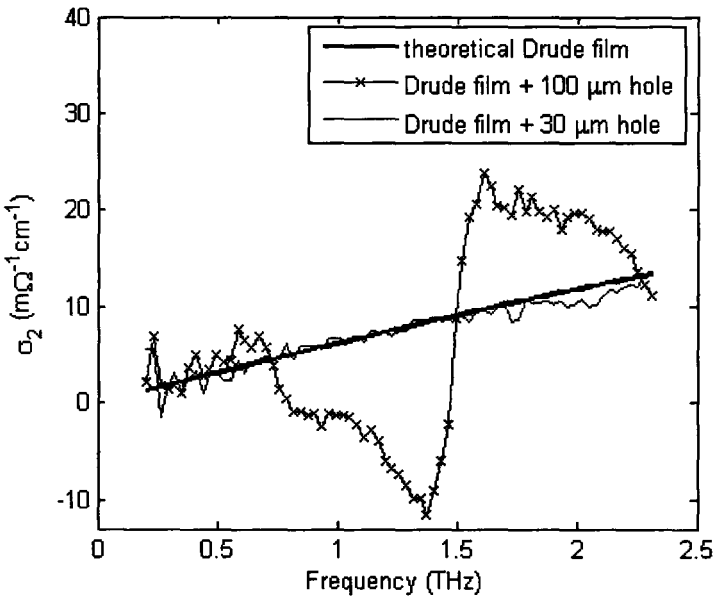

Figure 3.12 Calculated spectra showing the effect on the imaginary part of the conductivity of pinholes of 30 μm and 100 μm diameter. Note that the 100 μm hole creates a significant artifact, while the 30 μm hole does not.

[†] <20 μm

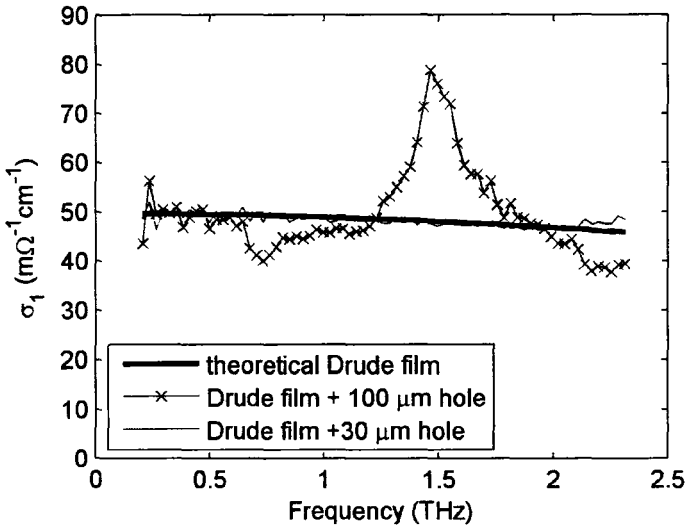

Figure 3.13 Calculated spectra showing the effect on the real part of the optical conductivity of holes of 30 μm and 100 μm diameter. Note that the real part of the conductivity is also susceptible to artefacts caused by the 100 micron hole.

3.2.7 Effect of Scratches

The impact of scratches is somewhat more pronounced than that of pinholes. As expected the transmission is highly dependent upon the orientation of the scratch with respect to the THz polarization. As the THz is horizontally polarized with respect to the lab frame of reference, the transmission through a vertical scratch is much greater than that of a horizontal scratch, as can be seen in Figure 3.14. The influence of such a scratch on the optical conductivity is determined by mathematically adding the transmission through the scratch to the transmission of an ideal superconducting film that follows the two-fluid model. A scratch, approximately 10 μm wide, oriented parallel to the THz electric field produces negligible artifacts in the imaginary part of the conductivity, as can be seen in Figure 3.15, whereas a scratch orientated 90° to the THz produces significant artifacts across the entire measured frequency range. Figure 3.16 shows a comparison of the artifacts in the real part of the conductivity for horizontal and vertical scratches.

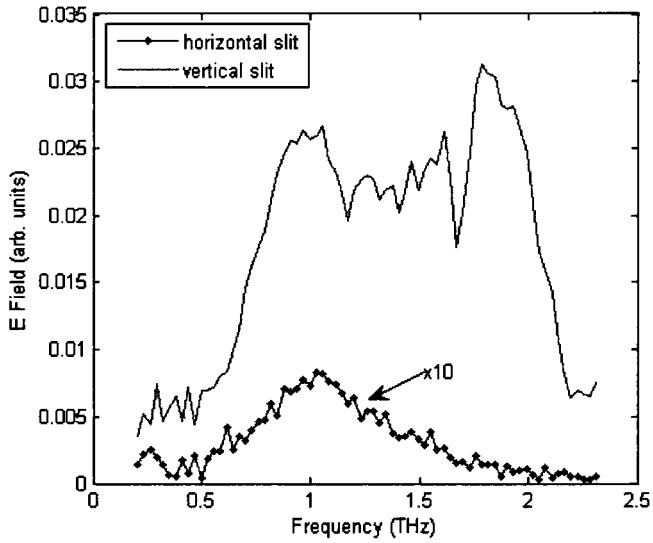

Figure 3.14 Transmission of THz through a 10 μm vertical slit in Al foil compared to the transmission through a horizontal slit. Note that of signal the transmission through the horizontal slit, which has been multiplied by 10 on the graph for clarity, is significantly weaker than the transmission through the vertical slit.

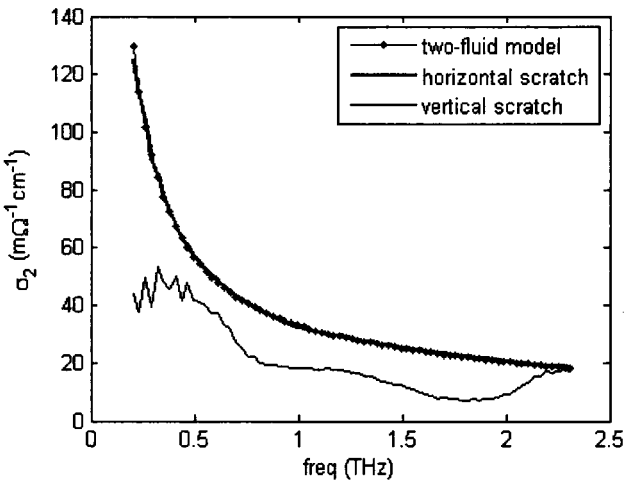

Figure 3.15 Calculated spectra showing the effect of horizontal and vertical "scratches" on the imaginary part of the optical conductivity. Note that the effect of the horizontal scratch is negligible

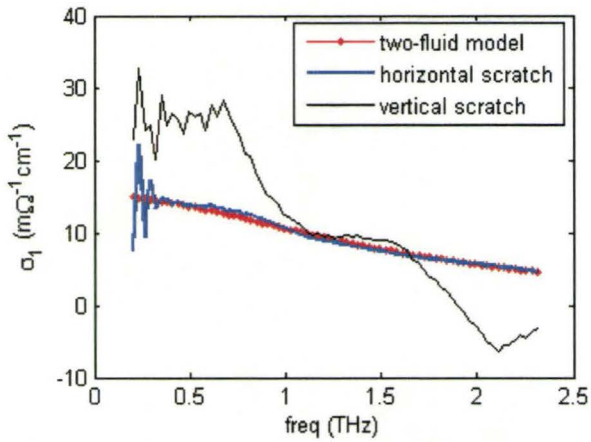

Figure 3.16 Calculated spectra showing a comparison of the effect of a vertical scratch to that of a horizontal scratch on the real part of the optical conductivity. Note that the horizontal scratch has little impact on the resulting spectra except at low frequencies.

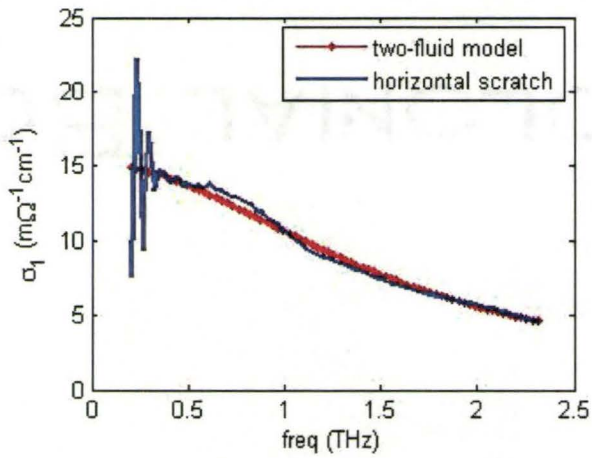

Figure 3.17 A close-up of the effect of horizontal "scratch" on the real part of the optical conductivity.

As expected, vertical scratches produce a much more pronounced effect on both parts of the conductivity. The real part of the conductivity exhibits minor artifacts due to a scratch parallel to the radiation, except at low frequencies as seen in Figure 3.17. Artifacts due to scratches were avoided by optically inspecting each film prior to measurement and discarding those films having scratches or defects.

3.3 Phase shifts and path length precision

The analysis of the experiments presented in this thesis depends upon a careful examination of the phase and amplitude changes in the THz transmission due to the presence of a sample/substrate as compared to a bare substrate reference. As stated previously, it is crucial that any changes to the system between the measurements of the sample and the reference be minimized. Otherwise systematic changes to the path length[‡] will be incorporated into calculations of the sample's optical properties and manifest as artifacts in the conductivity. To obtain the substrate reference measurements the film was removed; therefore it is not feasible to obtain the reference scan immediately following the sample scan. This section will identify and discuss the various sources and solutions to path length error that can affect the system between measurements. Path length errors can originate from a number of sources: (i) humidity changes, which alter the refractive index of air, (ii) mirror drift, which can change the path length without noticeably affecting the alignment of the beam and (iii) changes to the laser beam path associated with the pointing stability of the laser. It will also be shown that the imaginary part of a superconducting film is particularly robust to typical path length drift. Phase errors are somewhat more insidious than errors in the power spectrum as they typically affect the entire measured frequency range. Consider the effect of water vapour: the absorption peaks can be identified and filtered out, but the phase shift associated with a change in humidity is more difficult to correct. The phase shift associated with a 21% change in humidity is shown in Figure 3.3. It is non-trivial to simply correct for the phase shift at the analysis stage as the phase shift is not spectrally uniform, as shown in Figure 3.18. It is crucial that the humidity does not change during a scan, or between reference scan and film scan lest artefacts will be present. As seen in section 3.2.1, the humidity levels were kept below 5 % with a controlled nitrogen purge. It can be seen in Figure 3.18 that once the relative humidity levels are below 10 %, the index of refraction of air does not change enough to significantly affect the phase.

[‡] Due to laser drift, mirror shifts etc.

Careful monitoring of the beam path is necessary as minute path length changes do not always manifest as obvious misalignments. Even small changes in the path length can show up as phase shifts in the data: a change in path length of 10 μm is enough to show up in the phase of the THz spectrum as is shown in Figure 3.19. Beam path stability is monitored using a beam profiler which shows the profile and position of the IR spot before it enters the THz purge box. Additionally, control measurements of the THz transmission are repeated throughout the experiment. The amplitude and phase of the transmitted THz power for the control measurements are compared to verify that no significant changes have occurred in the system. A more detailed discussion of the beam path monitoring is given in Appendix 2.

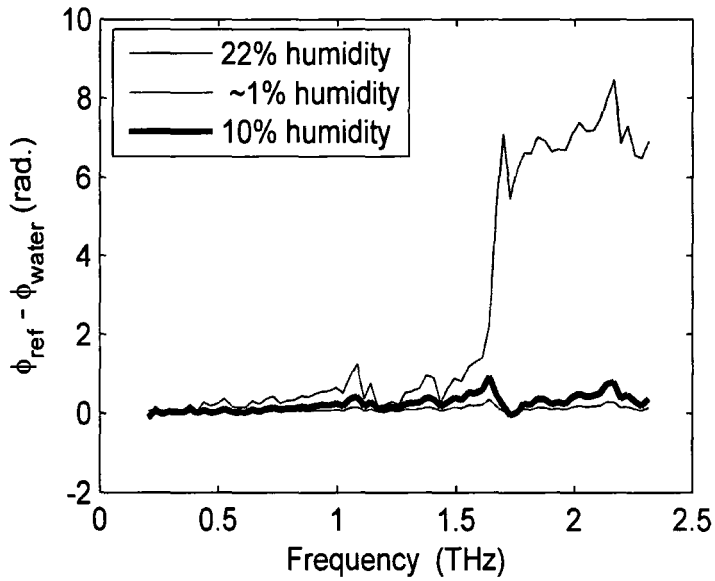

Figure 3.18 The change in phase of the THz electric field between a reference scan of dry air and humid air. Note the huge frequency dependent change in the phase for the humidity level of 22%, while the 10% humidity gives an almost null phase shift except near the 1.6 THz absorption line.

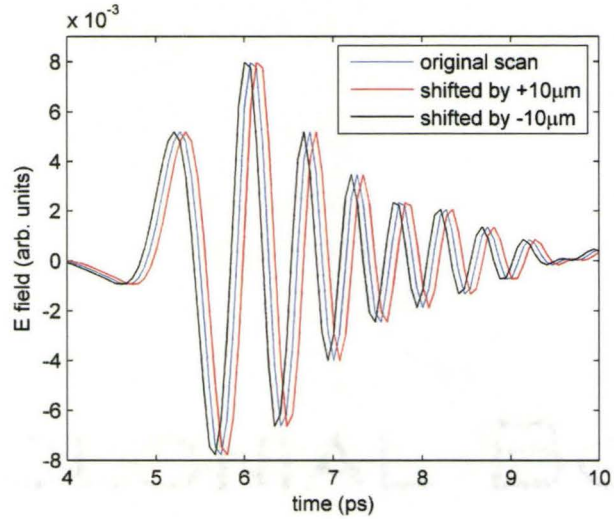

Figure 3.19 The phase change associated with artificially shifting the electric field by 10 microns in the temporal domain.

It is instructive to consider the effect of an artificial phase shift between the film and substrate measurement on the calculated conductivity. In Figure 3.19, a 10 μm phase shift was artificially added to the original transmitted electric field through a film-substrate in the time domain. This figure shows an obvious error in the phase shift (also see Figure 3.20) between THz transmitted through a film/substrate and a bare substrate in the frequency domain. This corresponds to shifting the data array by 1 data point in the raw scan of the electric field, as the step size for the delay line is 10 μm. The effects of this 10 μm shift on the conductivity will give a general sense of the maximum possible error associated with minor path length changes. The relationship between the phase and the conductivity is better understood by re-writing the thin film conductivity as:

$$\sigma = \frac{(n_s + 1)}{Z_0 d}\left(\frac{|E_{sub}|}{|E_{film}|}\left(\cos(\theta_{sub-film}) + i\sin(\theta_{sub-film}) - 1\right)\right) \qquad 3.2$$

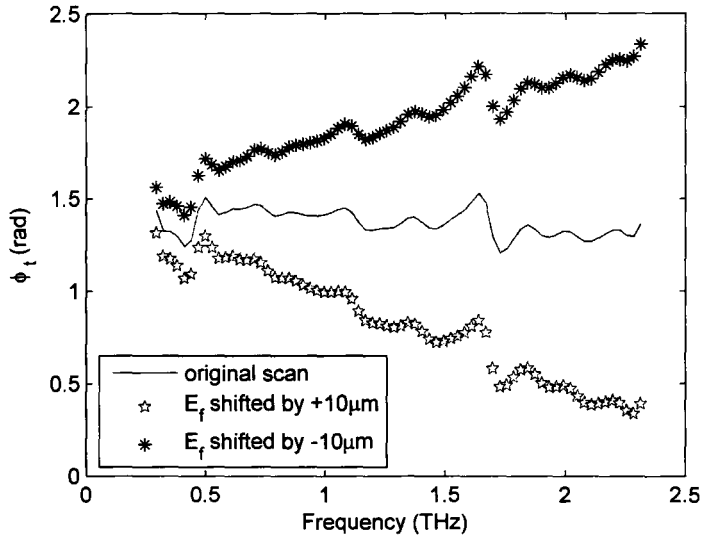

Figure 3.20 The phase of the $t=E_{YBCO}/E_{sub}$. The transmitted THz electric field through a YBCO film is artificially shifted by +/- 10 μm to give an illustrate the effect of path length changes on results.

Thus, the real part of the conductivity depends on the cosine of the phase change, and the imaginary part of the conductivity depends on the sine. It is important to note that the imaginary part of the conductivity is robust to a shift in the path length as large as 10 μm, as shown in Figure 3.21. It is also important to note that a shift this large would be spotted and corrected prior to data analysis. The real part of the conductivity, however, is much more susceptible to phase related errors below T_c. Therefore, greater weight will be placed on the imaginary part of the conductivity in the analysis presented in the following sections, as typical uncertainties in the path length do not lead to appreciable artifacts in the imaginary part of the conductivity of a superconducting film.

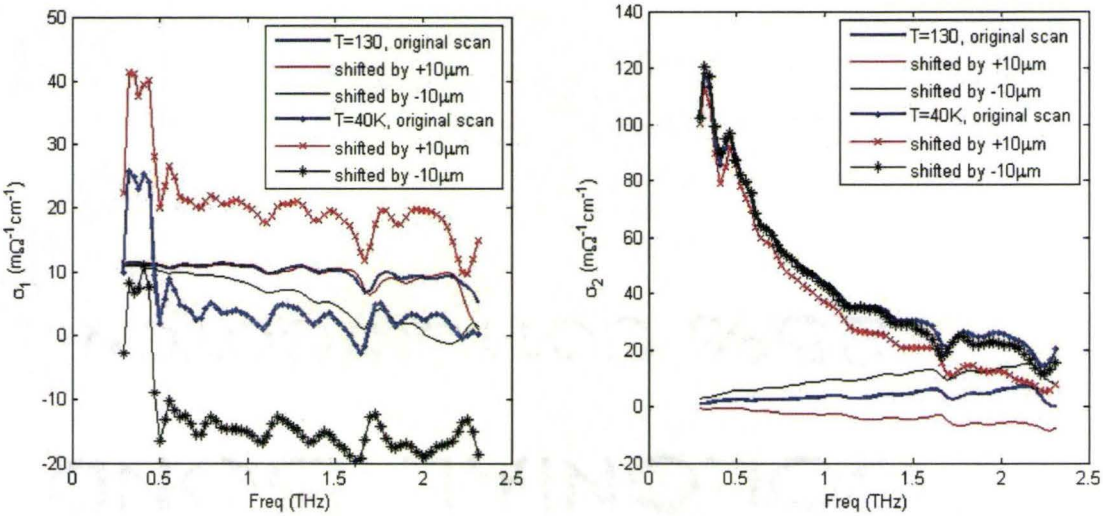

Figure 3.21 The error in the optical conductivity associated with a path length error of 10 μm.
a) On the left is shown the real part of the conductivity for T=130 K and T=40 K.
b) On the right is shown the imaginary part of the conductivity. This illustrates that for temperatures $<T_c$, the real part of the conductivity is much more sensitive to phase related errors. Above T_c, the imaginary and real parts of the conductivity seem to be similarly sensitive to errors.

3.4 Temporal limitations

It is important to consider the experimental limitations associated with temporal resolution whenever attempting to probe fast processes within a material. The typical pulse width of a pulse exiting the laser is 50 fs, which can be considered instantaneous compared to the few picoseconds associated with the initial fast recovery of the superconducting film. The THz pulse, however, is significantly longer with a duration in excess of 2 ps. This impedes our ability to accurately measure the spectral signature of processes that are on the same order of magnitude. In this section the various issues associated with temporal resolution will be discussed.

Consider the effect of humid air on the THz electric field in the temporal domain. The narrow absorption bands in the frequency domain manifest as a persistent ringing[§] in the transmitted electric field in the temporal domain. This is illustrated in Figure 3.22 and Figure 3.23. The effect of zeroing out the ringing in the temporal domain results in a

[§] Ringing in this case refers to the long lived oscillations in the electric field, *E(t)*.

spectrum that is free of sharp absorption lines. The drawback to relying on mathematically eliminating the ringing is that the resulting spectrum shows a suppression for several frequencies. From an experimental point of view, some energy loss is expected as it is impractical to capture all of the ringing by prolonging the temporal scan indefinitely. This provides yet another motivation for reducing the humidity levels.

As stated above, the THz pulse duration is lengthened considerably by the presence of water vapour, as shown in Figure 3.24. If one attempted to use this "ringing" pulse to probe an optically excited sample, the sample would likely reach equilibrium before the entire THz pulse can travel through the sample. The resulting measured THz electric field would, therefore, be a convolution of the transmitted THz field through the sample at various stages of recovery and the frequency dependence of the recovery would be intricately woven into the resulting waveform. This is obviously an extreme case that is avoided by minimizing the water content in the air, but is a useful thought experiment when considering the limits of temporal resolution.

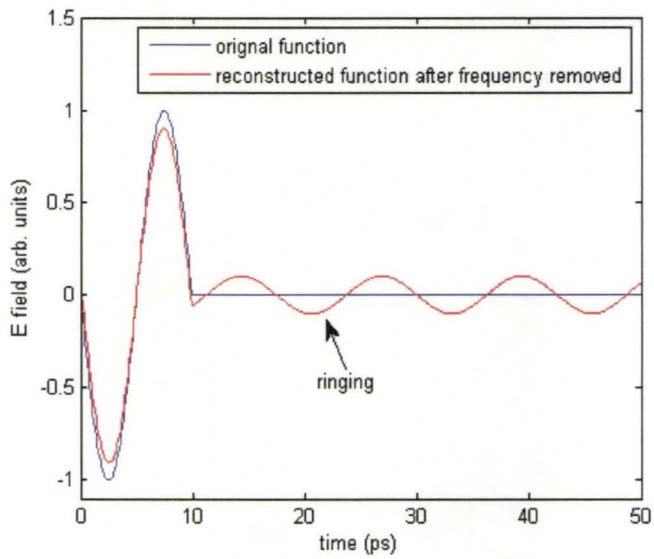

Figure 3.22 The calculated spectra (in red) showing the ringing effect in the time domain brought about by the removal of a single frequency from the original spectral function. The original function (in blue) is much shorter.

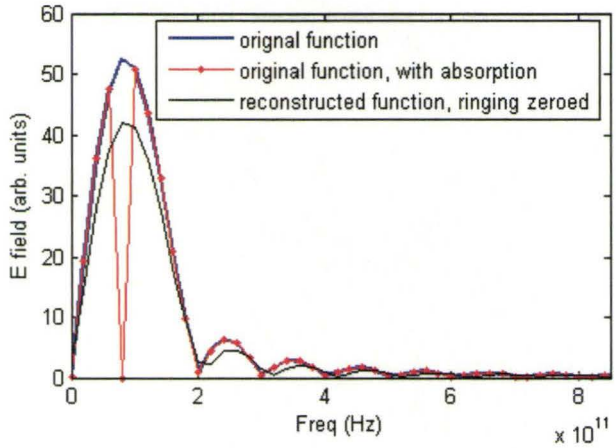

Figure 3.23 Comparison of the original spectral function with the function after a single frequency has been removed in the frequency domain, and the effect in the frequency domain once the ringing in the time domain has been zeroed.

Most of the energy in the THz pulse is contained within the first cycle of the electric field of the THz pulse, which is ~0.7 ps long. This creates significant challenges to the analysis of the recovery of the film at early timescales. The delay between the optical pump and the THz probe is held fixed, as seen in Figure 3.25, while the transmitted THz waveform is acquired.[**] The film cannot be frozen in time, and will be recovering as the THz waveform is acquired, which makes the determination of "$t = 0$"[††] nebulous, as shown in Figure 3.25. In this thesis, "$t = 0$" refers to the time at which change in transmitted THz power is largest.[‡‡] It is assumed that the transmitted THz power is maximized when the optical pump arrives at the film concurrently with the most energetic part of the THz pulse.

[**] by varying the delay between the THz pulse and the optical probe, as discussed in section 1.5.
[††] The time at which the optical pump and THz probe arrive at the sample simultaneously.
[‡‡] The transmitted THz power calculation comes from integrating over the square of the THz electric field.

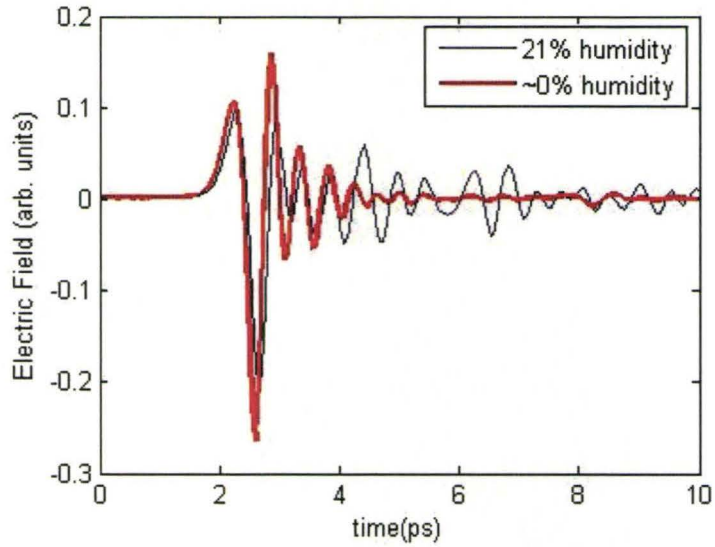

Figure 3.24 Difference in the electric field in the time domain for a THz pulse travelling through humid air and dry air. The ringing caused by the sharp absorption peaks of water creates a ringing which continues indefinitely.

The THz waveform is collected in the time domain, but analyzed in the frequency domain. This requires a fast fourier transform (FFT), which assumes that the electric field was captured under static conditions. As discussed above, taking the FFT of a waveform captured while the film is rapidly changing can lead to additional spectral artefacts. This is discussed in depth by Averitt *et al.*[75] These complications, however, are not an issue in the results reported here as we have concentrated on timescales much longer than the THz pulse duration. When the recovery of the film is not slow compared to the THz pulse duration, the transmitted THz power is not a reliable measurement of the dynamics in the film. It is for this reason that the analysis of the dynamics of the film is restricted to long timescales in excess of 10 ps for work presented in this thesis.

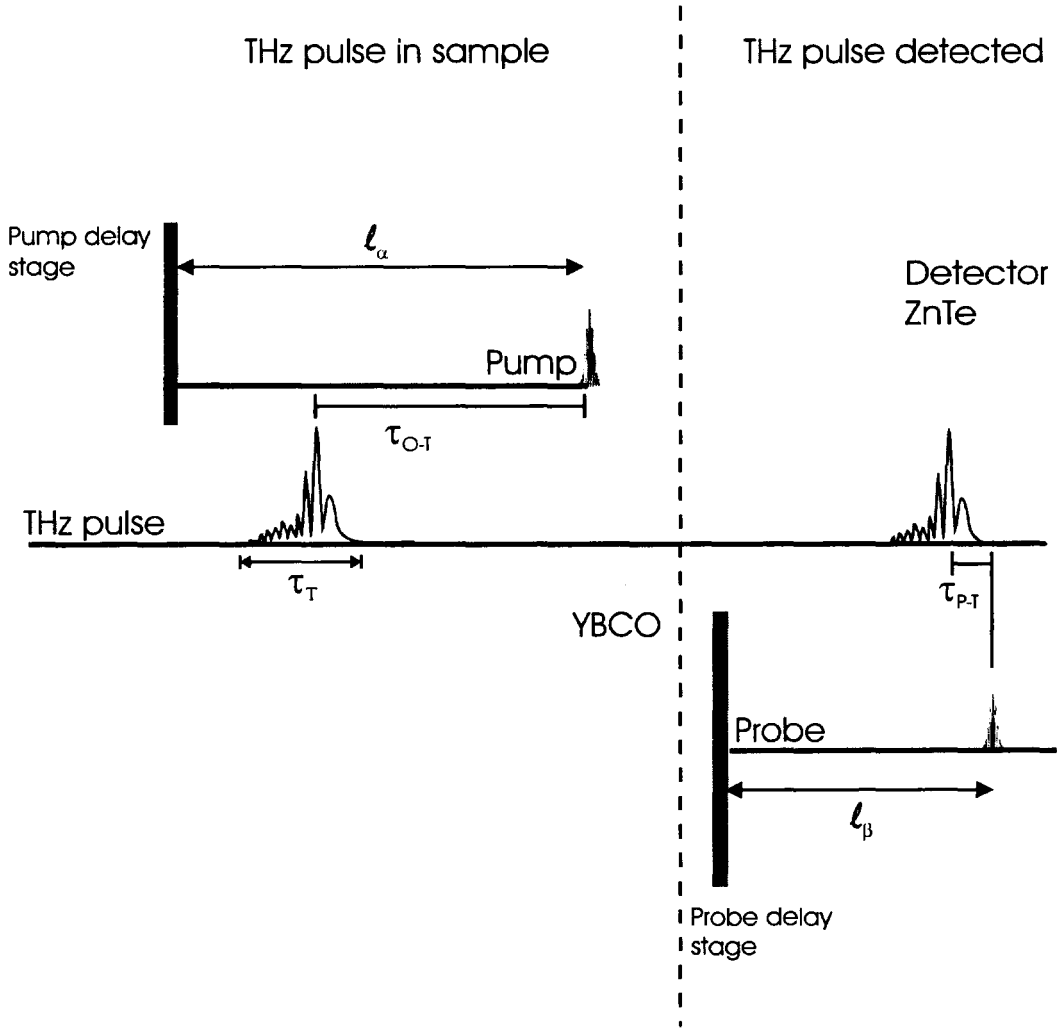

Figure 3.25 On the left is shown the relative time delay between the arrival of the optical pump and the THz probe at the YBCO thin film where τ_T is the THz pulse duration, and $\tau_{O\text{-}T}$ is the time at which the main THz peak arrives at the YBCO film following the arrival of the optical pump. The leading edge of the THz pulse will experience the film at $t = \tau_{O\text{-}T} - \Delta t$, where Δt represents the difference between the time at which the peak arrives at a given point and the time at which other portions of the THz electric field arrive. ℓ_α represents the movable delay line for the optical pump that controls $\tau_{O\text{-}T}$.

The right hand side of the diagram shows the timing associated with the detection of the transmitted THz pulse. The main peak of the THz pulse arrives at the ZnTe detector crystal at $t = \tau_{P\text{-}T}$. As the delay ℓ_β changes, the optical probe will sample different portions of the THz pulse.

The delay ℓ_α is held fixed while the transmitted THz pulse is sampled by the optical probe. Thus the measured THz pulse contains information about the sample from times $t = \tau_{O\text{-}T} - 1/2\tau_T$ to $t = \tau_{O\text{-}T} + 1/2\tau_T$.

3.5 Uniform optical excitation

Another consideration is the relative spot sizes of the THz probe and THz pump. Although the THz probe is focussed onto the sample using off-axis parabolic mirrors the spot size is limited by the long THz wavelengths. The largest wavelengths in the pulse are on the order of 3 mm. The optical pump spot size is kept large enough[§§] to irradiate the entire optically available region of the film as seen in Figure 3.26. If the spot size of the optical pump is not at least as large as the THz spot size then the transmitted THz pulse will contain information about the optical properties of both the irradiated portions of the film and the unpumped regions. As time passes the energy will dissipate across the film, but due to the long pulse duration of the THz probe this effect would be difficult to analyze. Added to this is the complication that the THz spot is not spectrally uniform. The higher frequencies are concentrated near the centre of the beam, so if the optical excitation of the film is not uniform, then there will be spectral artefacts.[105] However, by not focussing the optical pump, and by irradiating the entire optically available surface of the film the impact of these effects on the final results is negligible.

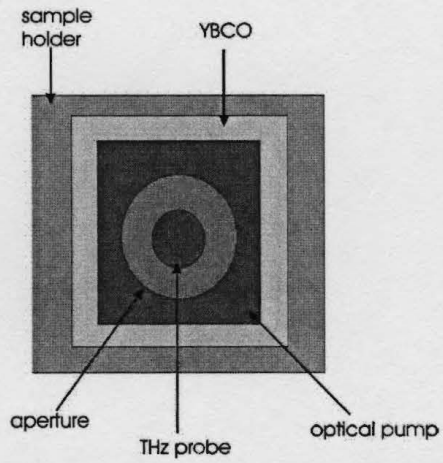

Figure 3.26 A schematic of the spot geometry of the THz radiation and optical pump. The optical pump spot is larger than the aperture of the sample holder to ensure uniform irradiation across the THz probe region.

[§§] 0.25 mm^2

3.6 Summary

In conclusion, there are numerous experimental considerations that must be taken into account when investigating the spectral dependencies of a dynamic system using a broadband pulse. The reduction and control of water vapour in the air, proper alignment, and path length monitoring ensure that spectral artefacts are minimized, and where present, identified and remedied. With care, it is possible to keep systematic changes in the spectrum to an acceptable level between sample and reference measurements. Acceptable changes to the system are generally those that produce changes in the transmitted power on the same order as the inherent noise of the data. Typically this means 4% error in the THz power. A detailed understanding of the relationship between experimental uncertainties, such as path length changes, or temporal limitations, and the frequency dependent optical conductivity provides a high level of confidence when analyzing results.

Chapter 4 Sample preparation and experimental procedures

4.1 Film growth

The thin films used in these experiments were grown in-house using the pulsed laser deposition (PLD) technique.[105,106] In this technique, laser pulses are used to ablate (i.e. vapourize) material from a stoichiometric polycrystalline YBCO target, which lands upon a heated substrate. The process takes place in a deposition chamber[107] (see Figure 4.1) which maintains an oxygen pressure of 200 mTorr. The excimer laser outputs UV pulses at a repetition rate of 10 Hz with a 20 ns duration and a wavelength of 248 nm. For YBCO, the plume of material ejected from the superheated target surface is essentially identical in composition to the target material. As a result, by carefully controlling the composition of the target while maintaining a high level of cleanliness in the chamber, films of high purity can be produced. When the plume of yttrium, barium, copper and oxygen reaches the substrate, the atoms orient themselves to create unit cells of YBCO, provided the substrate is at an appropriate temperature. Substrate heating is required to provide mobility to the atoms landing on the substrate surface so that YBCO unit cells can form. It is important not to elevate the temperature high enough that the copper evaporates from the surface of the film, leaving it deficient in this element. If, on the other hand, the temperature is too low, then the film's transport properties diminish

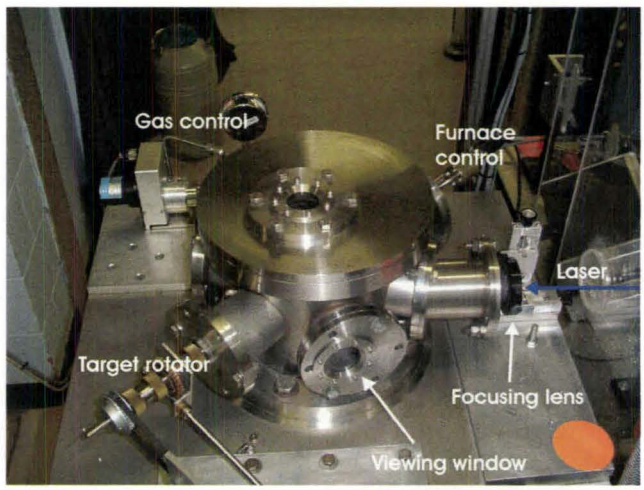

Figure 4.1 The growth chamber used for PLD at McMaster. [107]

dramatically due to poor microstructure. For temperatures below 650 K, the c-axis growth gives way to an a-axis orientation of even poorer quality. The optimum temperature for c-axis YBCO film growth varies considerably for various deposition techniques and growth conditions, but is typically in the 700-850 °C range.[108]

The substrate used in the deposition must be carefully chosen so that its lattice matches as closely as possible to the lattice parameters of YBCO. For a c-axis thin film, the substrate must match to the a- and b-axes of YBCO. Recalling that a = 3.82 Å and b = 3.89 Å, the quality of the lattice match to various candidate substrates can be determined from Table 4.1. Additionally, for the purpose of the experiments described here, it is required that the substrate be transparent in the THz region, with no sharp spectral features. Untwinned crystals are also preferred, as it reduces defects in the film and avoids spectral complications due to mixed crystal orientations of the substrate. This effect will be discussed in the latter part of this chapter. The films analyzed in this thesis were grown on LSAT.

Substrate	Lattice parameter (Å)
$LaAlO_3$: (LAO[109])	3.79
$SrTiO_3$ - (STO[110])	3.89
$SrLaGaO_4$: (LSGO[111])	3.84
$NdGaO_3$: (NGO[112])	3.86
MgO[113]	4.21
$(LaAlO_3)_{0.3}(Sr_2AlTaO_6)_{0.7}$ (LSAT[114])	3.87

Table 4.1- List of the various substrates commonly used in the deposition of c-axis thin films of YBCO, as well as their acronym, and lattice parameters. The lattice parameters should be compared to the a- and b-axis lattice parameters of YBCO (a = 3.82 Å , b= 3.89 Å)

As previously mentioned, the superconducting properties of YBCO can be altered dramatically by varying the oxygen content within the film. In terms of PLD film growth, YBCO is always grown in an oxygen deficient state. If cooled in an oxygen ambient environment, the film will uptake more and more oxygen as it is cooled until the rate at which it acquires oxygen is slower than the cooling rate. At this point the process becomes too slow to be effective. Thus, by controlling both the level of oxygen within

the chamber and the cooling rate it is possible to alter the oxygen content in the film. To obtain the optimally doped material, the film is cooled in a 1/2 atmosphere of oxygen as it cools from the growth temperature to room temperature in period of two hours. To obtain a transition temperature near 60 K the film is cooled in 200 mTorr of oxygen as it cools to 200 °C in a period of 45 minutes. At this point, the deposition chamber is filled with helium in order to cool the film to room temperature as fast as possible. This final step allows for films with higher oxygen uniformity as it limits the oxygen uptake at these low temperatures where there is a tendency for the surface to have a higher oxygen content then the underlying material. Other transition temperatures can be obtained through variations to the oxygen cool-down procedure.

The films grown for the THz experiments typically have areas in excess of the 25 mm^2, large enough to accommodate the THz spot size, which cannot be focused as tightly as an optical beam due to the long wavelengths present in the THz pulse. The results discussed in this thesis are from three films having different levels of oxygen doping: a 40 nm thick near optimally doped film with $T_c = 86$ K, and two 100 nm thick underdoped films, one with a $T_c = 73$ K and another with $T_c = 56$ K. Figure 4.2 shows the resistivity curves for all three samples. It should be noted that the optimally doped material has a lower T_c than the bulk material, as is common for extremely thin films[115].

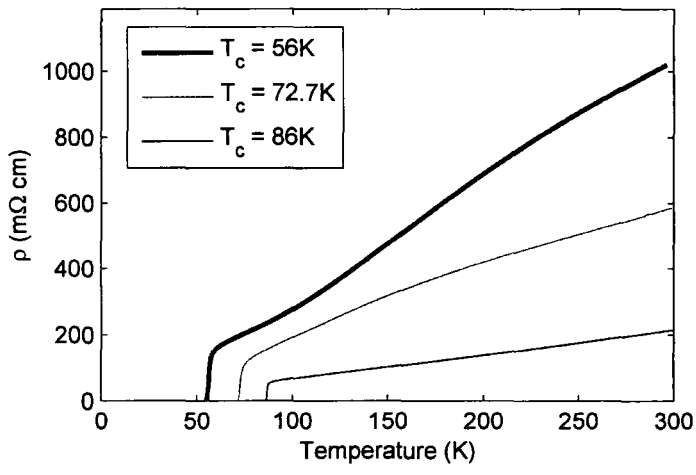

Figure 4.2 Resistivity of three samples with different values of T_c. The optimally doped sample with $T_c = 86$ K exhibits a linear resistivity above T_c, while the underdoped samples have a kink associated with the pseudogap.

4.2 Sample preparation

Quality control of samples is imperative. The resistivity of the sample must be measured to ensure that the film is a good superconductor. For optimally doped YBCO the superconducting transition should be sharp. A broad transition could be indicative of a film that is not uniformly doped. The resistivity above T_c should be linear. For an underdoped film, the temperature dependence of the resistivity should exhibit the kink (see Figure 4.3) above T_c indicative of a pseudogap, as well as a sharp superconducting transition at a lower temperature.

Each film needs to be visually inspected for cracks, holes and defects using an optical microscope in transmission mode. Any films with numerous* or large† pinholes were discarded due to the potential for artifacts as discussed in Chapter 3. Figure 4.4 shows a typical image.

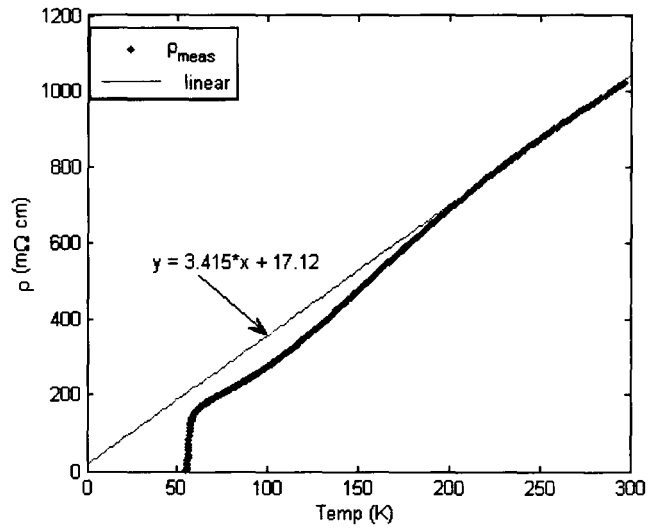

Figure 4.3 Resistivity of an underdoped YBCO thin film with a T_c of 56 K. Note that the normal state resistivity of the film deviates from a linear behaviour. The resulting "kink" in the resistivity near 175 K is evidence for the opening up of the psuedogap.

* More than 10 pinholes in the region of interest.
† >30 μm

Figure 4.4 Optical transmission image of a good quality 50 nm thick YBCO film.

Once an appropriate film has been chosen it is mounted on the sample holder, which is made of copper to ensure excellent thermal coupling to the cold finger. Silver paint is used both to "glue" the sample to the holder and to provide additional thermal coupling. A ring of silver paint placed between the film and the holder prevents THz leakage around the sample. Although the YBCO films produced typically have an area in excess of 25 mm^2, and are at the focus of the THz spot during the experiments, the long wavelengths of the THz are still capable of leaking around the edges of the sample. This is illustrated in Figure 4.5 where the leakage around aluminum foil is measured to be non-zero. Once the sample is mounted, it is checked again for any new defects that may have been caused during the mounting process. When the sample was not in use it was stored in a dessicator as long term exposure to the water vapour in air is known to be detrimental to YBCO.

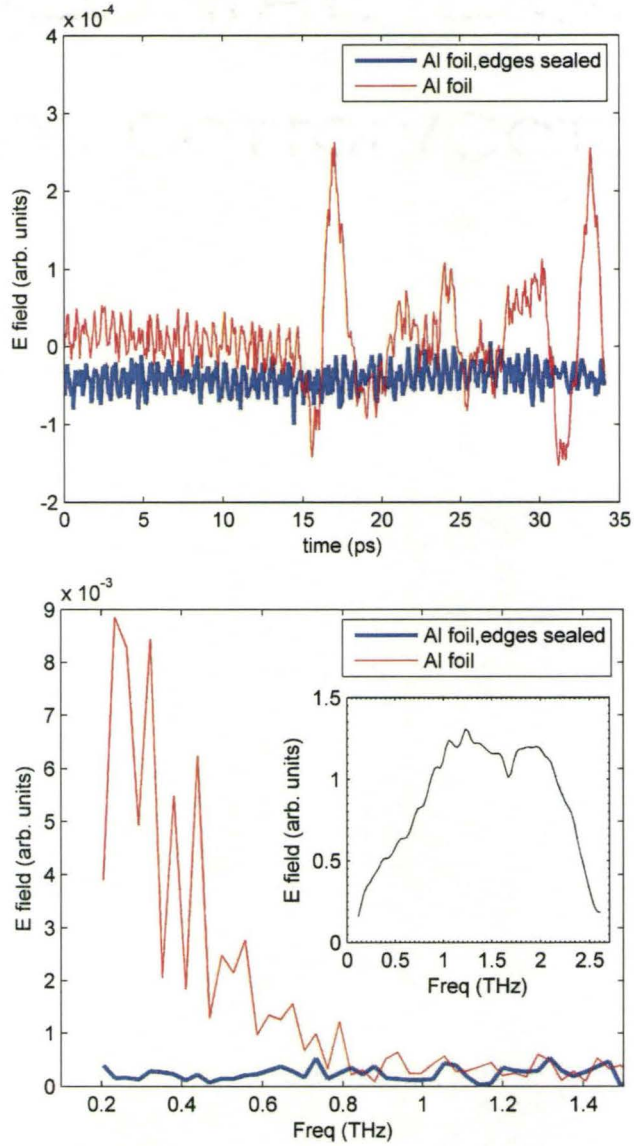

Figure 4.5 The leakage around the edges of an aluminum foil "sample" that has been tacked down at the corners is shown in red. The blue line shows that when the edges of the foil are sealed with silver paint, the leakage is blocked. On the top is shown the electric field in the temporal domain, on the bottom is shown the electric field in the frequency domain. It is the long wavelengths associated with low frequencies that can leak around the edges of an Al foil sample. The inset shows the spectrum with no foil present, for reference.

4.3 Experimental procedures of the THz system

In this section, the experimental protocols necessary to prepare for an optical-pump-THz-probe experiment will be outlined. Quality control measures will be briefly discussed, and the procedures for alignment of the IR beam and the sample will be shown.

4.3.1 Laser power monitoring

At the beginning of any experiment the bandwidth and power of the seed pulse exciting the oscillator are measured and recorded. Thus, the initial beam characteristics can be maintained, which ensures consistency throughout the experiment. At the output of the laser system, a combination of a quarter wave plate and a polarizing beam splitter is used to control the output power, as seen in Figure 4.6. The power is monitored with a 99% beam splitter and diode. The diode current is filtered and converted to an output voltage by a current amplifier. The output voltage is recorded at a sampling rate of 0.0167 Hz by a DAQ program, while a voltmeter gives an instantaneous reading of the output voltage. The wave plate is adjusted so that the power is 400 mW. This is typically 20-30% lower than the maximum power, which means that even if the power

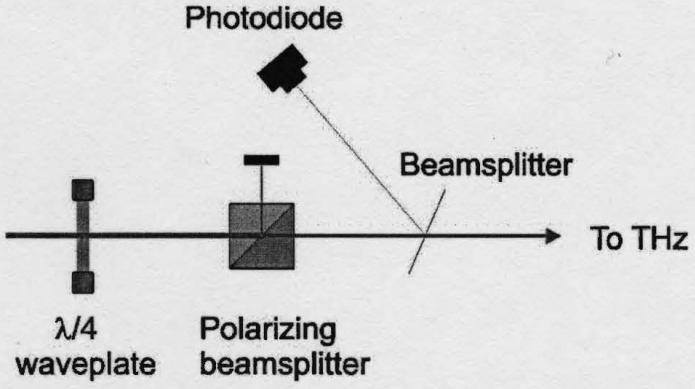

Figure 4.6 Schematic showing the optical components used to measure and control the laser power. The photodiode monitors the laser power throughout the course of the experiment and the waveplate allows for power adjustment.

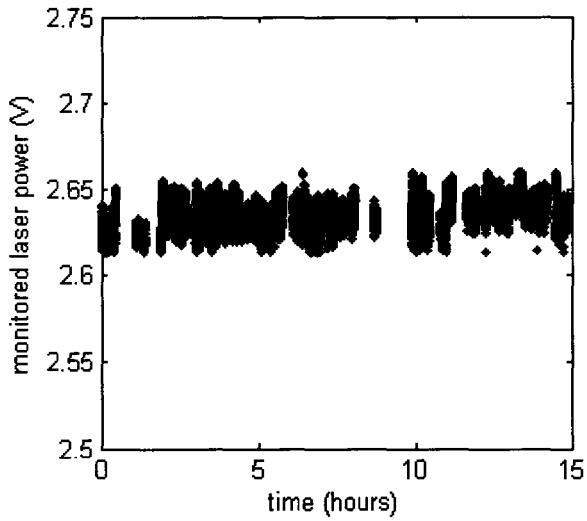

Figure 4.7 Laser power as monitored over the course of an experiment using the voltage on a photodiode. The gaps in the data correspond to times when it was necessary to block the laser output.

decreases at the output of the laser system, the input power to the THz system can be kept constant. The relationship between the THz spectrum and the laser power is discussed in more detail in Appendix 3.

Between each scan the voltage reading is checked to ensure that the amplifier output power has not drifted between measurements. Figure 4.7 shows a typical recording of the laser power over the course of an experiment. Of particular concern were power fluctuations traced to the stability of the chiller water temperature. Since the thermal cycling of the chiller water occurs on timescales similar to the time it takes to acquire a THz scan, this produced an apparent modification of the spectral content of the THz pulse. The source and mitigation of this effect is discussed in more detail in Appendix 3. Generally, with careful monitoring, the laser power fluctuations can be kept to within 2%.

4.3.2 Beam profile monitoring

The spatial profile of the optical beam was regularly recorded to monitor pointing stability and beam characteristics. A portion of the beam was captured using leakage from a mirror near the THz generation and detection delay line in order to minimize disruption to the setup and maximize the sensitivity to small changes in the beam direction. A new beam profile was recorded hourly during each experiment and visually compared to the original profile. Any drift was corrected at the output of the laser system in order to obtain a real time correction of the drift, a video camera was pointed at the display, which showed the reference and the live beam profile side by side on a video display located at the amplifier output. The beam path monitoring is discussed in further detail in Appendix 2.

4.3.3 Alignment of the THz system

Before the start of each experiment, the alignment of the THz set-up must be optimized. IR sensitive cards and an electronic IR viewer are used in conjunction with pinholes to check and adjust the three optical beams in the THz set-up: the THz generation beam, shown in Figure 4.8, the THz detection beam, and the pump beam used to optically excite the sample. The THz detection line is the most sensitive of the three beams to misalignments and thus receives the greatest attention during alignment. If the beam does not arrive at the delay stage at normal incidence the position of the IR spot on the detector crystal will change during a scan. A finer control of the alignment of the IR probe used for THz detection can be obtained by blocking one of the detection photo-diodes shown in Figure 4.9, and tweaking the beam direction to obtain maximum signal in the absence of THz radiation. After the alignment procedure, the pinhole that limits the power of the THz detection beam is adjusted to maintain an 8 V signal from the detection photodiodes. This is checked with one of the photo-diodes disconnected, as the output voltage is the difference between the two photo-diode's signals. This step ensures consistent detection from one experiment to the next.

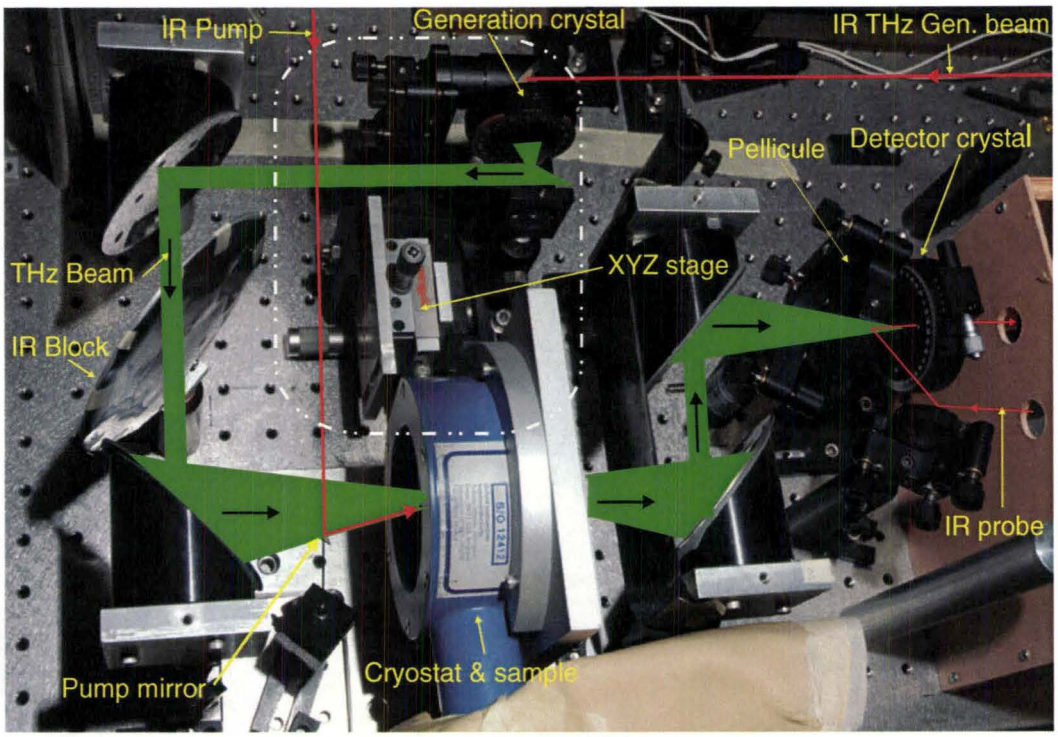

Figure 4.8 Picture of THz set-up. The generation crystal is located on an XYZ stage shown in the white dashed-dotted box. The THz beam is shown in green and the IR beams are shown in red.

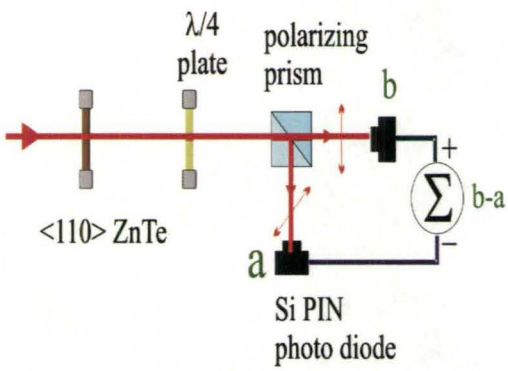

Figure 4.9 Set-up for detection of THz radiation. The IR detection beam arrives at the ZnTe detection crystal, which changes the polarization of the beam in the presence of THz radiation. Following the quarter wave plate, the IR beam is split by the polarizing beamsplitter into its horizontal and vertical components which are then detected by two photo-diodes. The recorded signal is the difference of these two measurements.

Once the IR beam lines have been optimized, the position of the THz spot on the detector must be checked. Ideally the THz spot and IR probe should overlap concentrically on the detector crystal to measure maximum signal and bandwidth. The THz spot is imaged onto the sample and the detector crystal using five parabolic mirrors which collect the THz and focus it onto the sample and the detection crystal, as shown in Figure 4.8. The THz generation crystal is mounted on an x-y-z stage to allow the focal spot to be imaged to different locations on the detector crystal as well as to change the position of the focus. The relationship between the THz signal and the alignment of the THz spot on the detector is discussed in more detail in Appendix 4. To optimize the focal position of the THz spot on the detector the following procedure was employed:

1. Find the signal strength of a major peak in the THz electric field using the lock in amplifier.
2. Translate the stage of the generation crystal by 1 μm, noting the original position.
3. Tweak the IR probe delay line to recover the THz peak. If it is larger than the initial value, continue translating the stage of the generation crystal in the same direction. If it is smaller try the opposite direction.

4.3.4 Sample alignment

The alignment of the sample requires a somewhat different approach as it is not feasible to place a pinhole at the sample position due to the physical restrictions imposed by the cryostat. The alignment procedure used relies on the measurement of the signal strength of the transmitted THz electric field. The delay of the IR probe beam is set to detect the largest THz peak in the temporal domain while the cryostat is translated through the THz beam until the signal reaches half of its maximum value. As the THz beam is symmetric, optimal alignment is at the position halfway between these FWHM points. This procedure is repeated for the vertical alignment. After the cryostat has been

aligned, it is securely fastened to the optical table with a plate that fits over the cryostat's head. This ensures that the cryostat will not move during the experiment.

Inserting or removing the cryostat transfer tube is a procedure which can put considerable physical stress upon the cryostat, which, without proper care, can disrupt sample alignment. Thus, the peak THz voltage is monitored throughout this procedure to ensure stability. Additionally, a reference scan is taken before and after the transfer tube is inserted or removed so that it can be verified that the alignment of the cryostat has not changed significantly. If changes to the alignment are detected appropriate measures are taken to remedy the situation.

4.3.5 Optical pump alignment

After sample alignment, the tiny pump mirror (shown in Figure 4.10) must be aligned to direct the pump beam onto the sample. The pump beam is centered over this mirror to ensure that the spot is uniform, which is then adjusted so that the IR pump illuminates the sample. This is verified by observing the beam spot with an IR card once

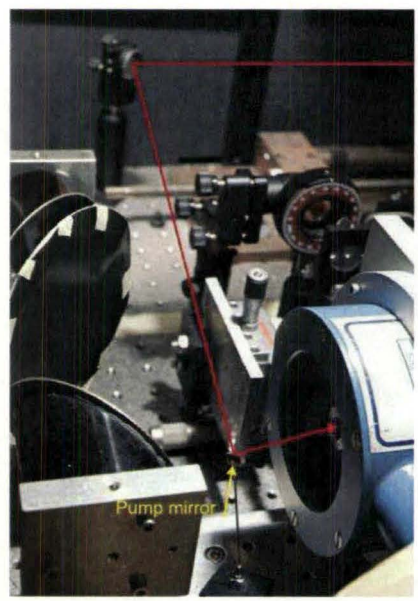

Figure 4.10 The pump mirror directs a beam into the cryostat which is large enough to irradiate the sample area. Note that the THz beam is directed onto the sample by the parabolic mirror located immediately behind the pump mirror.

it has exited the cryostat. The pump power is measured at the cryostat's front window by temporarily placing a detector in the beam path. The transmitted optical pump is also measured after the cryostat to give a rough estimate of how much energy is absorbed by the film. After the alignment is complete, the purge box is placed over the THz set-up, sealed and then purged with N_2 until the relative humidity is lowered to less than 5%.

4.4 Data acquisition

As previously stated in Chapter 2, the focus of the experiments presented in this thesis is to determine the spectral evolution of YBCO thin films during the film's recovery following optical excitation. Due to the destructive nature of the process used to obtain reference measurements (i.e. removing the film from the substrate), the dynamic and steady-state measurements on the film must be completed prior to the reference measurements. The long times required for data acquisition make it unfeasible to obtain all the necessary measurements on a single film in one day. As a result, a dataset is acquired in two stages. The first stage consists of measuring the response to optical excitation above and below T_c. The transmitted THz electric field through the film following optical excitation can be used to calculate the dynamic optical conductivity. This calculation will be discussed in greater detail in Section 4.5. In the second stage of the experiment, the steady-state transmission of the film-substrate combination is recorded for several temperatures. These measurements are followed by reference measurements of the transmission through the bare substrate for each temperature of interest. From this the optical conductivity of the steady-state film can be calculated.

4.4.1 First Stage: Optical Excitation

In order to provide an estimate of the temperature increase caused by optical excitation, the temperature dependence of the steady-state transmission through the film was recorded as a guide (see Figure 4.11). To improve accuracy of the measured curve, it is important to keep the temperature increment sufficiently small[‡] when the THz transmission is changing more rapidly with temperature. The repetitive nature of the optical excitation causes the equilibrium temperature of the film to rise. In order to improve the accuracy of the measured temperature of the film, an estimate of the background heating must be obtained. This estimate is obtained by comparing the transmitted THz power at $t < 0$ ps[§] to the temperature trend of the unexcited film. Figure 4.12 shows a plot of the typical background heating.

The temperature trend must be recorded during the same session, as the transmitted THz power is sensitive to changes to the system that occur from one day to

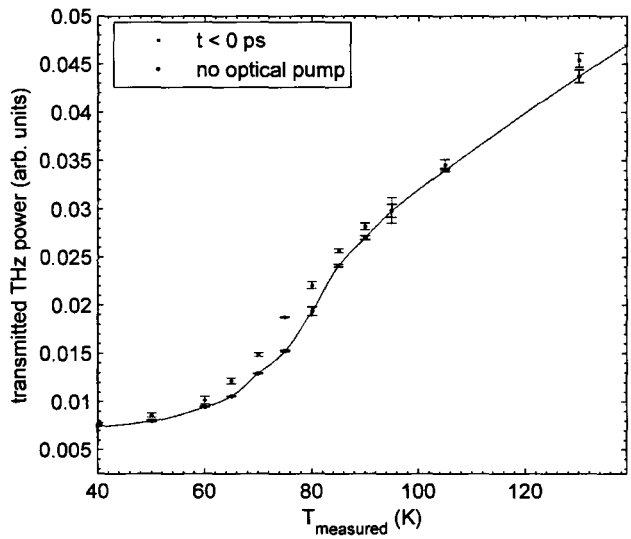

Figure 4.11 A comparison of the temperature trend of an unexcited optimally doped film to a film that is optically excited at 1 KHz.

[‡] 5K-10K

[§] Prior to the arrival of the optical excitation pulse.

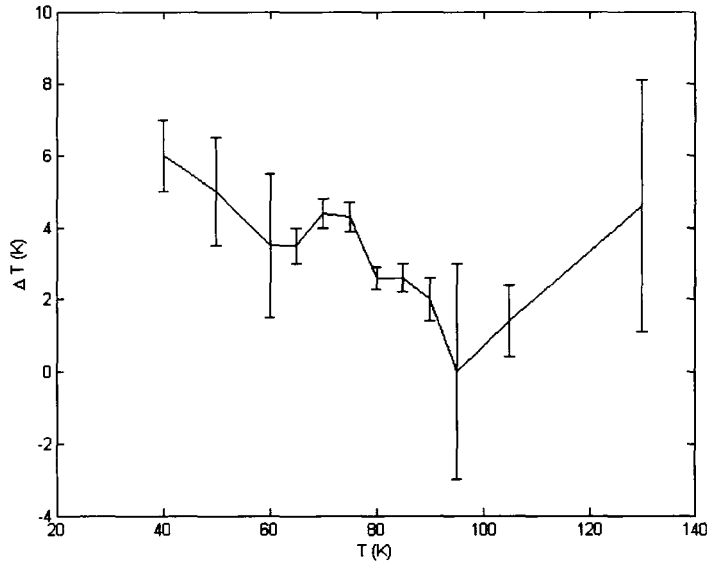

Figure 4.12 Change in the temperature due to the repetitive optical excitation (1 KHz) of a 40 nm thick YBCO film with a T_c of 86 K.

the next, such as shifts in the overlap between the THz beam and the IR probe on the detector crystal. THz power measurements, therefore, act as an effective first order detector of the long term system stability (i.e., over the course of an experiment). The transmitted THz power for a convenient temperature is measured repeatedly at regular intervals throughout the experiment. By comparing the total transmitted THz power and the power spectrum for these control measurements, quality control of data can be ensured.

4.4.2 Second Stage: Steady-State and Reference

The purpose of the second stage of the experiment is to record the data necessary to calculate the optical conductivity of a YBCO film in equilibrium for several temperatures above and below T_c. The steady-state measurements should be taken for the same range of temperatures as were used for the dynamic measurements so that a comparison between the steady-state and excited films may be made. The comparison of

the transmitted THz power for an excited film to the temperature trend of the THz transmission may be used to determine which additional temperatures are useful for data analysis. The temperature increment between steady-state measurements needs to be small enough such that the dynamic optical conductivity at various times after optical excitation may be compared to the steady state optical conductivities. Additionally, a small temperature increment improves the resolution for the temperature trends of the scattering time and the superconducting fraction, f_s.

Once the steady state measurements of the film-substrate are complete, the cryostat is heated back to room temperature. It is important that the cryostat and transfer tube are allowed to warm up before the vacuum seal is broken, otherwise condensation may collect inside the cryostat.

The next step in stage two of the experiment is devoted to the measurement of the substrate's optical properties. In order to do this, the YBCO film is first removed from the substrate with a weak solution of citric acid. Even though this destroys the film being studied, it is preferable to using a new bare substrate since it prevents the introduction of artifacts to the calculated conductivity of the film due to variations between individual substrates.

The film removal process is performed without removing the sample from the sample holder in order to maintain optical alignment of the substrate. A bead of citric acid larger than the aperture of the sample holder is placed onto the film's surface. After a few minutes the acid is removed with a dry cotton swab. This procedure is then repeated to ensure that the YBCO had been completely dissolved. A distinct colour change will be apparent when the film has dissolved, as the film-substrate combination is a dark grey while the bare substrate is pink. To remove the citric acid residue and clean the sample, the process is repeated with distilled water after which the sample surface is gently swabbed with methanol.

It is not necessary to collect substrate reference scans at the same thermal resolution as for YBCO. As seen in Figure 4.13 and Figure 4.14, the substrate's optical properties do not change drastically with temperature. Generally, a 10 K step size is used for the substrate measurements. The substrate's index of refraction is not strongly dependent upon temperature for the thermal region of interest, therefore it is a reasonable approximation to find the index of refraction for a representative temperature in the middle of the temperature range covered, rather than for each temperature measured. For optimally doped YBCO the underlying substrate's index of refraction at 70 K is calculated. For an underdoped film with a $T_c = 56$ K, the index of refraction at 40 K is used.

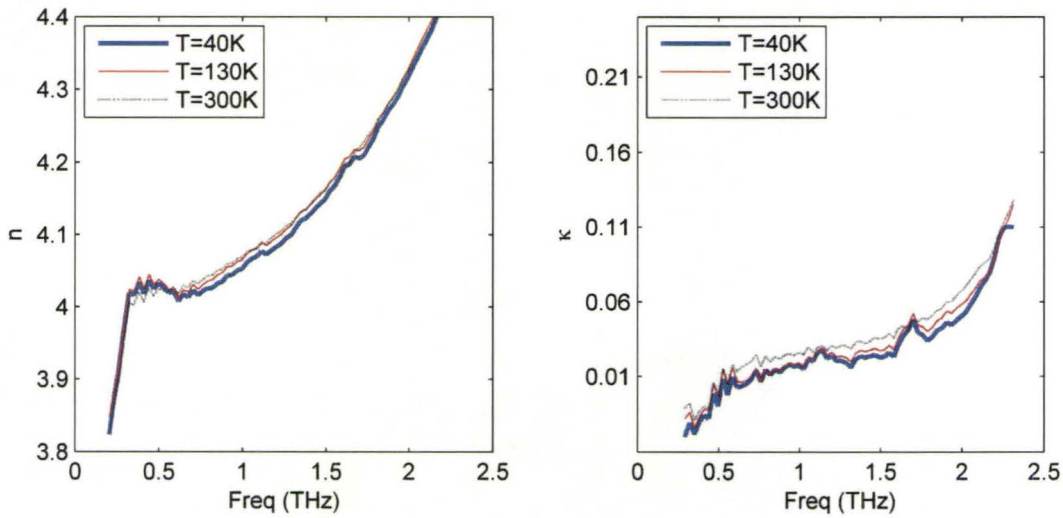

Figure 4.13 On the left is the index of refraction of LSAT in the THz region at room temperature, T=40 K and T=130 K. On the right is the extinction coefficient for the same temperatures. Note that neither shows a significant temperature dependence.

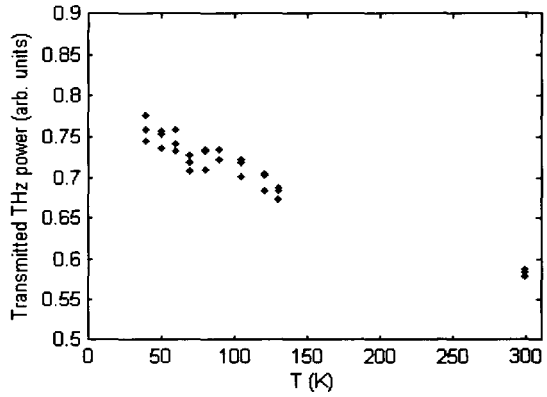

Figure 4.14 The transmitted THz power through LSAT as a function of temperature. As expected the relationship between the THz power and the substrate temperature is near linear.

4.5 Data analysis

In order to analyze the dynamic conductivity from experiments that span several days, a correction factor must be included to account for spectral changes caused by minor differences in the system from one day to the next. The optical conductivity is calculated using t^*, the ratio of the transmitted electric field through the bare substrate to the transmission through the film-substrate. The optical conductivity of a sample is an inherent property that will not change from one experiment to the next for the same film. This fact is used to correlate measurements done under similar conditions and temperatures from one day to the next. The substrate reference measurement $E_{sub}(\omega,T)$ needed for t^* is often taken on a separate day from the dynamic measurements of the sample. Including the correction factor to eliminate artifacts, the new substrate reference becomes:

$$E'_{sub}(\omega,T) = E_{sub}(\omega,T)\frac{E'_{film}(\omega,T)}{E_{film}(\omega,T)} \qquad 4.1$$

where $E_{film}(\omega,T)$ represents the measurement of the steady-state film-substrate taken during the same experiment as $E_{sub}(\omega,T)$, and $E'_{film}(\omega,T)$ represents the measurement of the same steady-state film-substrate on the day of interest. It is assumed that any

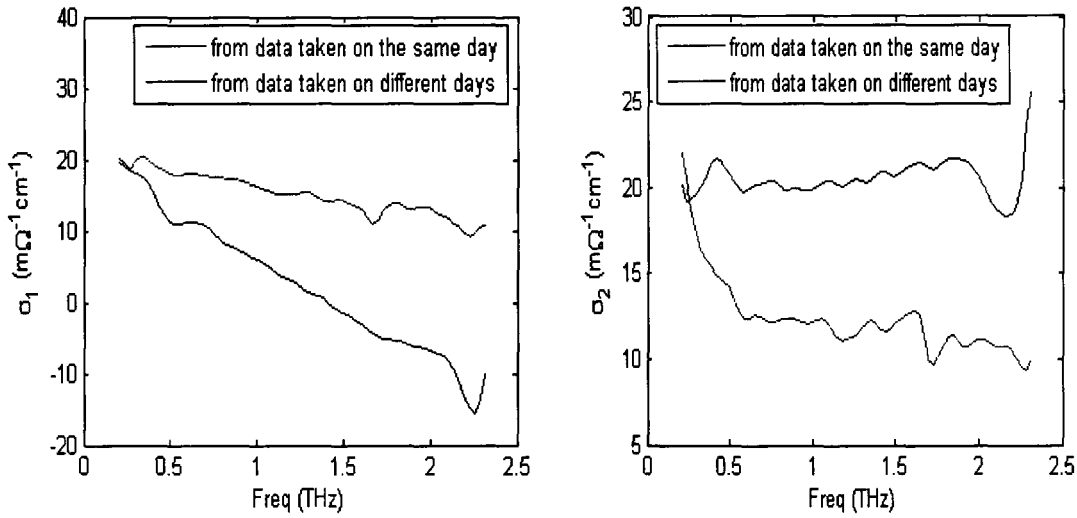

Figure 4.15 Plots of the frequency dependence of the real (left) and imaginary (right) parts of the optical conductivity. The red line denotes an optical conductivity that was calculated using a reference and sample measurement from the same day. The blue line denotes the conductivity calculated using measurements taken on different days. Thus, it is important to make appropriate corrections to account for changes in the THz system that would otherwise be incorrectly interpreted as contributions to the optical conductivity.

differences in THz transmission through the film-substrate from one day to the next are due to small changes in the system which can be simulated in the extracted THz transmission of the substrate using this method. Figure 4.15 demonstrates how artifacts can arise in the conductivity if these corrections are neglected. With this correction factor, the steady-state optical conductivity calculated using the extracted reference and the corresponding film-substrate measurement will be identical to the original calculated conductivity, as shown in Figure 4.16. The substrate is not affected by the optical pump, and so it is valid to use the calculated reference to find the optical conductivity for an optically excited film. Thus, when calculating the optical conductivity for a non-equilibrium film, the changes observed in the conductivity are due to changes in the optical properties of the film and not due to changes in the THz system.

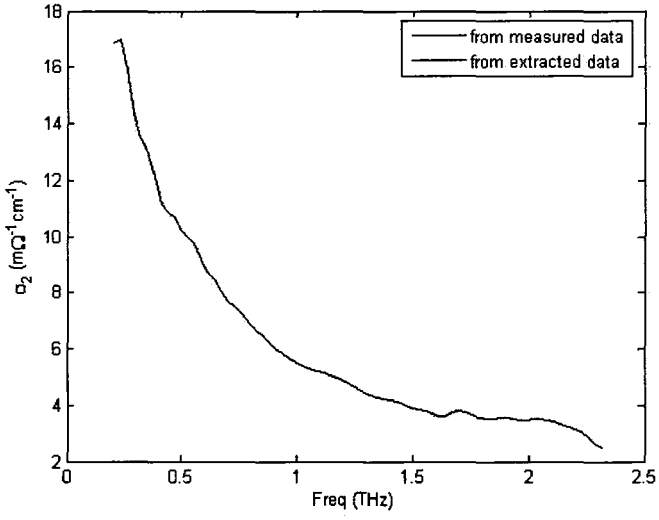

Figure 4.16 Comparison of the optical conductivity when the electric field transmitted through the film-substrate and bare substrate reference are measured during the same day, and the calculated conductivity when the substrate reference is taken on a separate day, but corrected to account for changes to the system. This can be considered an "extracted" substrate measurement. As expected, the optical conductivities are identical for both calculations.

4.6 Testing the system

Gold has been studied in depth using almost every technique.[116,117,118,119,120] Because it is well understood, it is ideal for testing new systems and experimental techniques and analysis procedures. A study in gold was conducted to test the accuracy of conductivities generated from our new THz system. Thin gold films were sputtered onto a $MgAl_2O_4$ substrate. Figure 4.17 shows t^*, the ratio of the THz transmission through the bare substrate to the THz transmission through a 45 nm gold film. At this thickness, the gold is still partially transparent to intense light. Figure 4.18 shows the real and imaginary parts of the optical conductivity of gold calculated from the THz transmission using the thin film approximation. This can be seen to agree tolerably well with the Drude model for a gold film with a DC conductivity of 35.7 $mOhm^{-1}cm^{-1}$ and a scattering rate of 38.5 THz, values which are in close agreement with those reported in the literature.[121]

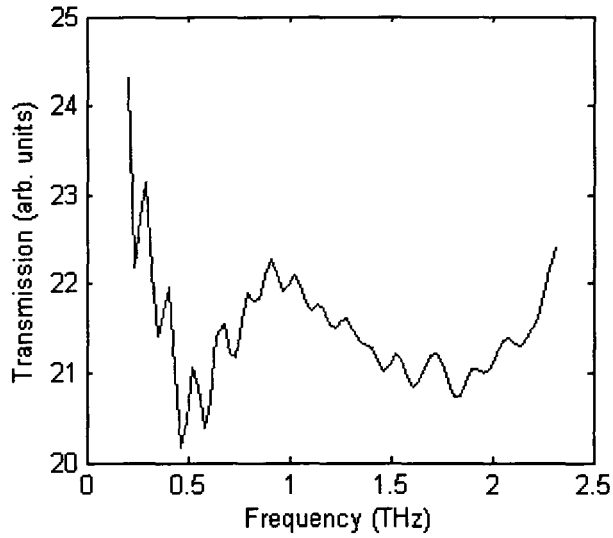

Figure 4.17 The ratio of the THz transmitted through a bare $MgAl_2O_4$ substrate normalized by the transmitted THz electric field through a 45 nm thick gold film.

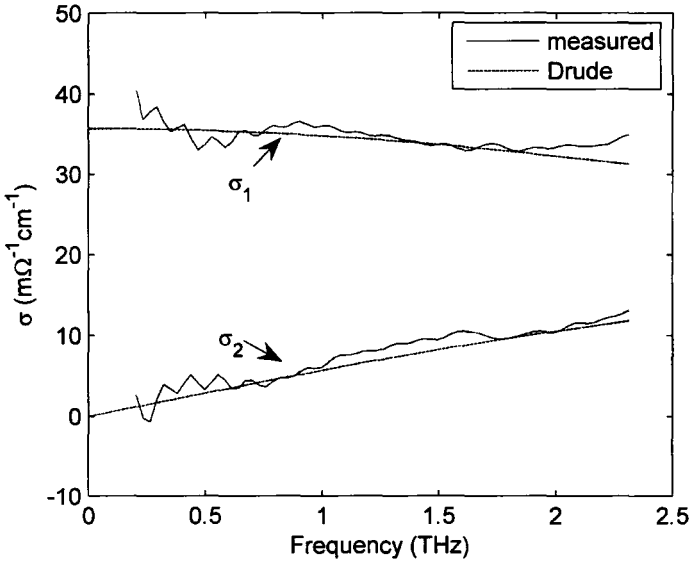

Figure 4.18 Optical conductivity of gold calculated using the thin film approximation. The dashed line shows the Drude conductivity.

4.7 Substrate characterization

4.7.1 $LaAlO_3$

Special care must be taken when choosing a substrate for THz measurements. The substrate must be transparent in the THz regime and be devoid of any major spectroscopic features within the region of interest. At the same time, it must promote excellent film quality for the material under study. For the THz experiments on YBCO presented in this thesis, LAO was initially chosen as a substrate as it has a good lattice match and promotes the formation of highly oriented epitaxial *c*-axis films. It was later discovered, however, that this substrate was not well suited to THz experiments.

The primary reason LAO is a less desirable substrate for the spectroscopic experiments in the THz regime is that it is heavily twinned, as seen in Figure 4.19. Diffraction can occur because the long wavelengths associated with the THz radiation have similar length scales as the twin domain spacing. This is a minor effect, however, when compared to the effect of birefringence of LAO. For a further discussion, see Appendix 6. In Figure 4.20, the birefringence of LAO can be seen. As the crystal

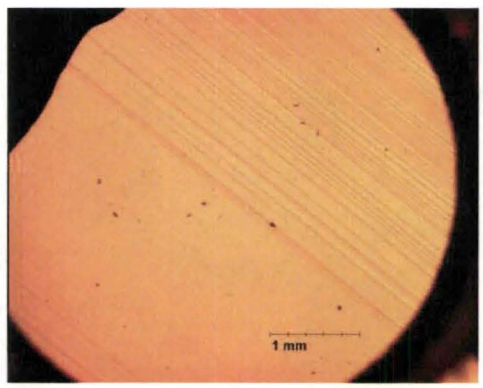

Figure 4.19 LAO twinning shown using an optical microscope in transmission mode.

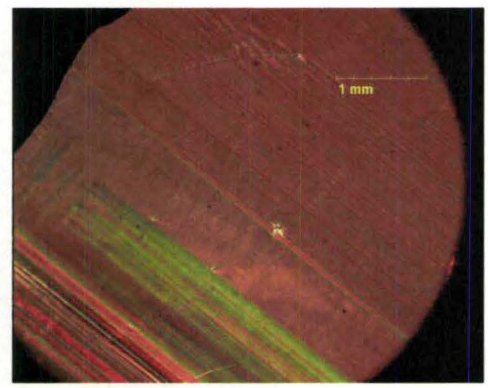

Figure 4.20 LAO birefringence in twin domains is shown using crossed polarizers with an optical microscope in transmission mode. The red and green regions illustrate the change in crystal orientation from one twin region to the next.

orientation changes with respect to the polarized light, the appearance of the twin domains changes from red to green under the microscope. The presence of different orientations of birefringent crystal domains in the substrate creates drastic artifacts in the calculated optical conductivity of the film as seen in Figure 4.21. If the orientation of the substrate changes between the transmission measurement of the film-substrate and the measurement of the bare substrate, there will be a discrepancy in the polarization of the transmitted THz radiation. This discrepancy will appear as a gain or loss of THz signal and will show up in the conductivity as the considerable anomaly shown in Figure 4.21. One possible remedy is to remove the film from the substrate while leaving it mounted. This ensures that the substrate orientation does not change for the reference measurements. This measure, however, is not sufficient as heavy twinning means that different crystal orientations are present in the THz probe region even without rotating the sample. Thus, any beam wander could change the ratio of one crystal orientation to the other, causing artifacts in the conductivity. The best solution is to avoid the use of LAO for THz transmission experiments. If for some reason LAO must be used, then it is best advised to use only those substrate areas which contain one uniform twin domain.

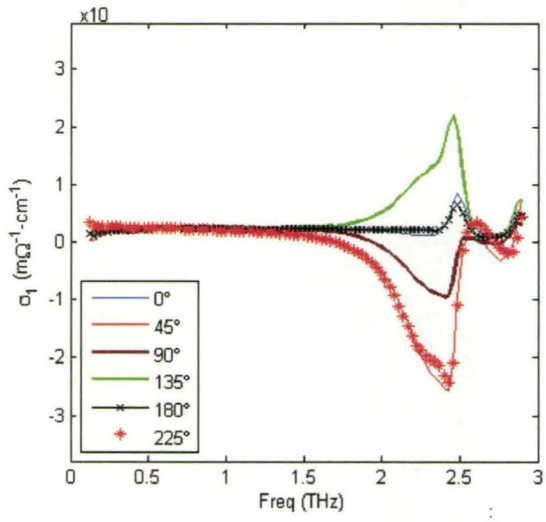

Figure 4.21 YBCO optical conductivity data showing a large artifact above 2 THz which is caused by the birefringence of LAO. The different curves illustrate the angular dependency of the artifact. The angle quoted represents the angle of rotation of the bare substrate reference, as compared to the orientation of the film-substrate.

4.7.2 Calculating the index of refraction

The index of refraction of the substrate must be known in order to calculate YBCO's optical conductivity using the thin film approximation. A rough estimate of the index of refraction can be made using the phase shift of the main THz peak. This, however, does not give a frequency dependent index of refraction, but it can be calculated from the phase (ϕ) of the transmission through the substrate using:

$$n = \frac{c\phi}{\omega d} \tag{4.2}$$

where c is the speed of light, and d is the thickness of the substrate. The extinction coefficient (κ) can also be calculated starting from the Fresnel equations. The Fresnel transmission for the substrate is given by:

$$t_{sub} = \frac{4(n+i\kappa)}{(1+n+i\kappa)^2} e^{\frac{-\omega d(\kappa - in)}{c}} \tag{4.3}$$

Then using the index of refraction, n, and assuming that $n>>\kappa$ the extinction coefficient can be calculated[**] from:

$$\kappa = \frac{-c}{\omega d} \log\left(|t_{sub}| \frac{(1+2n+n^2)}{4n} \right) \tag{4.4}$$

4.7.3 Possible substrates

In the search for a suitable substrate for YBCO films the optical properties of $NdGaO_3$ (NGO), $SrTiO_3$ (STO), $SrLaGaO_4$ (LSGO), and $(LaAlO_3)_{0.3}(Sr_2AlTaO_6)_{0.7}$ (LSAT) were measured. STO is not suitable for THz applications, as it does not transmit above 0.8 THz as can be seen in Figure 4.22. The index of refraction and extinction coefficient of LSGO, and NGO is shown in Figure 4.23. The absorption of LSGO and NGO is high for low THz frequencies and thus would make a less than ideal substrate choice for measurements where low frequencies are of interest.

[**] the contribution of κ is negligible to the amplitude of t_{sub} if κ is small.

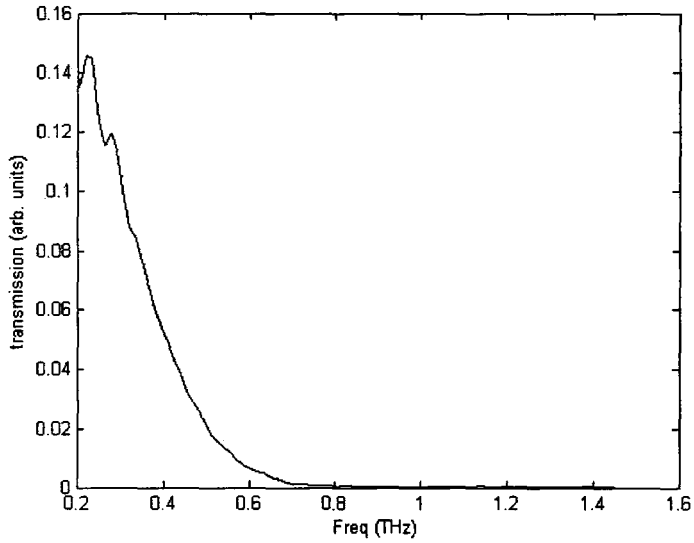

Figure 4.22 Transmission of STO for THz frequencies. The low transmission makes it unsuitable for THz measurements.

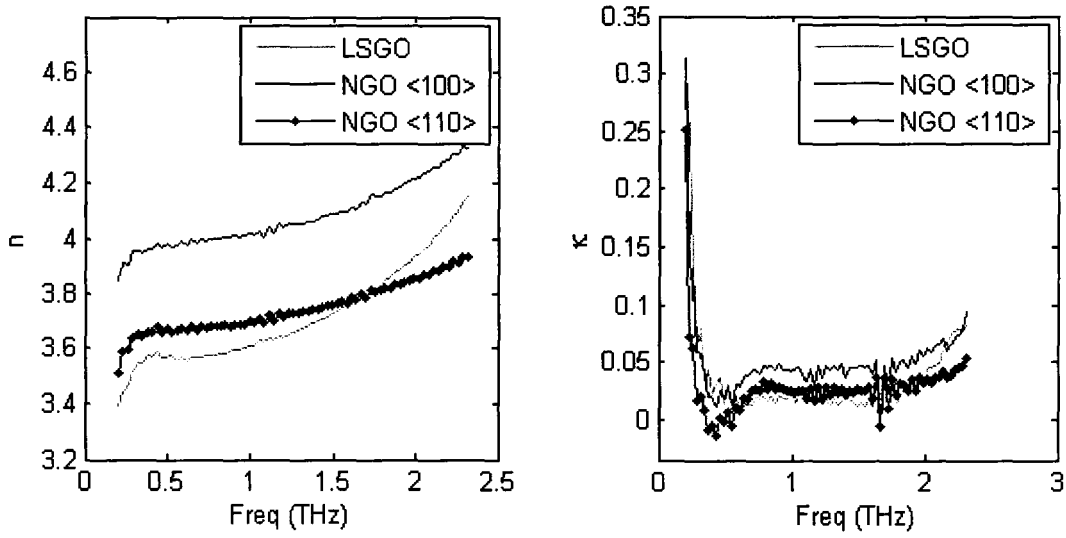

Figure 4.23 On the left is the index of refraction for LSGO and NGO. On the right is the extinction coefficient. The low frequency absorption makes both these substrates less ideal for THz measurements.

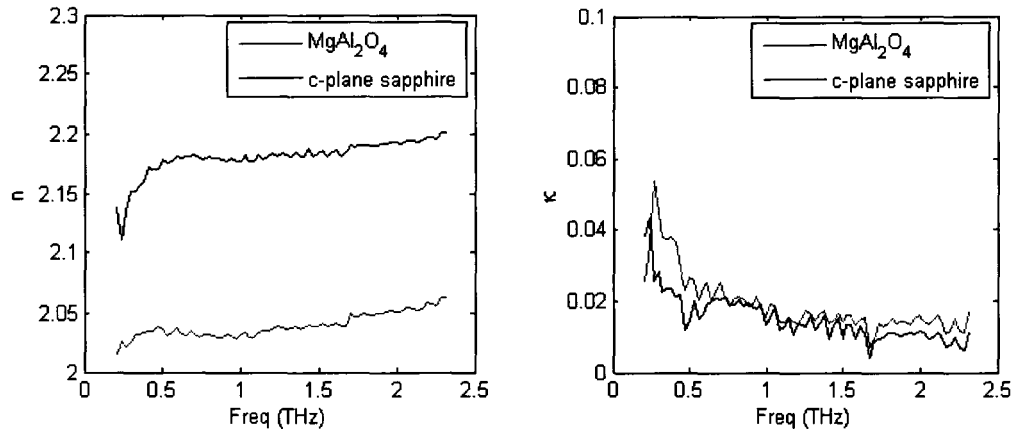

Figure 4.24 a) On the left is the index of refraction for $MgAl_2O_4$, and c-plane sapphire. b) On the right is the extinction coefficient for $MgAl_2O_4$ and c-plane sapphire. These materials are quite transparent to THz radiation, but are unable to support the epitaxial deposition of high quality YBCO thin films.

Other materials less suitable for YBCO film growth were also characterized. The THz transmission of $MgAl_2O_4$ (spinel), and c-plane sapphire was measured, as shown in Figure 4.24. Spinel and sapphire are used as substrates in many applications,[122,123,124] but make poor substrates for YBCO film growth.

Ultimately, the preferred substrate for YBCO thin films was found to be LSAT. The lack of twinning domains and high transmission in the THz regime makes LSAT suitable for THz experiments, and it is possible to grow quality films on LSAT. Also, the index of refraction is relatively flat over the region of interest, (see Figure 4.25) and the absorption is negligible. The contribution of the extinction coefficient to the optical conductivity is negligible as shown in Figure 4.26, therefore only the real part of the index of refraction is used in the conductivity calculations.

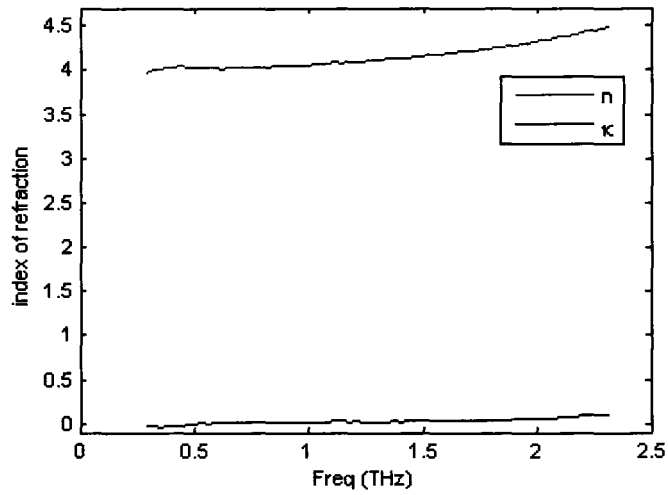

Figure 4.25 The frequency dependence of the real and imaginary parts of the index of refraction for LSAT at T = 70 K.

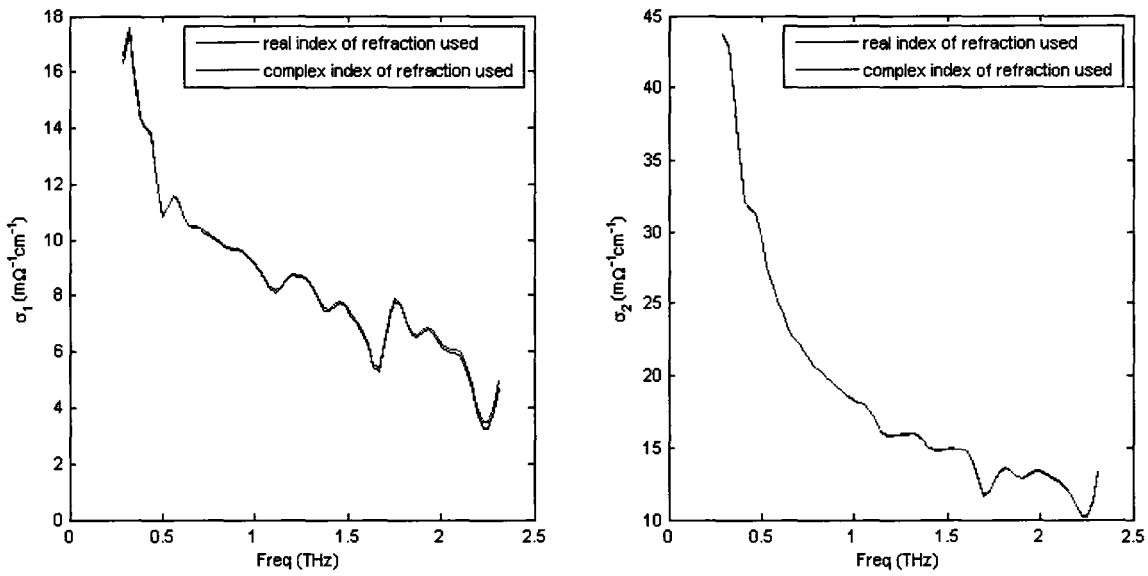

Figure 4.26 The effect of including (red line) and excluding (blue line) the extinction coefficient (κ) of LSAT on the calculated optical conductivity of YBCO. Note that there is little difference between the red and blue curves for both the real part of the conductivity shown on the left, and the imaginary part of the conductivity shown on the right.

4.8 Summary

In this chapter, the experimental procedures for the THz experiments reported in this thesis have been outlined. Experimental considerations important to reproducibility such as beam path monitoring, laser output monitoring, and various control measurements were discussed. A study of the various THz optical properties for candidate substrate materials was presented. It was concluded that LSAT was the preferable choice due to its transparency, lack of twinning domains and its ability to act as an excellent template for the deposition of epitaxial YBCO films. The capability of THz spectroscopy to determine the optical properties of materials has been demonstrated using a gold film, and various substrate materials. The data acquisition and analytical procedures for determining the steady-state and non-equilibrium conductivity of YBCO have been outlined. The results of these experiments will be presented in the following chapter.

Chapter 5. Results

5.1 Study of YBCO thin films

The unique ability of THz time domain spectroscopy to give both temporal and spectral information allows us to dynamically probe the superconducting condensate. To understand the dynamics of YBCO, the steady-state properties must first be examined. Figure 5.1 shows the resistivity of a near optimally doped 40 nm thick YBCO thin film. The resistivity is essentially linear above T_c, and the transition is sharp, which is typical of a high quality film. The fact that the superconducting transition is observed at a temperature somewhat lower than what is observed for the bulk material is not surprising as T_c is often suppressed in very thin films.[115] The temperature dependence of the total transmitted THz power through the film follows the resistivity, as is seen in Figure 5.2. As the temperature decreases, the film becomes a better metal (i.e. its conductivity increases) and as a result becomes more opaque to THz radiation. As the temperature drops through the transition temperature, the THz transmission decreases more rapidly due to the formation of the superconducting condensate. Below T_c, the transmitted THz power is dictated by the penetration depth. Thin superconducting films are used in the experiments so that the transmission is not negligible at low temperatures. Figure 5.3

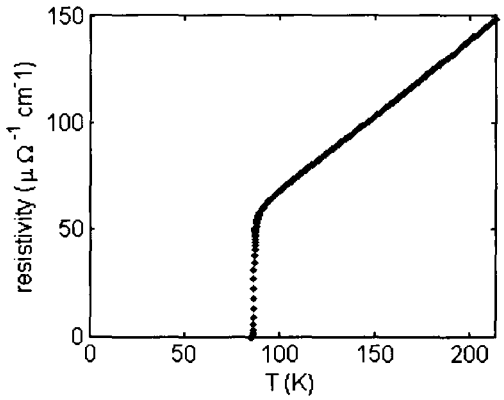

Figure 5.1 The resistivity of a 40 nm thick optimally doped YBCO thin film, T_c = 86 K.

shows the temperature trend of the transmitted THz power for three samples with $T_c = 86$ K, 73 K, and 56 K. The presence of the pseudogap in the underdoped samples increases the THz transmission above T_c. It is interesting to note that unlike the optimally doped case, there is no observed change in the transmitted THz power near T_c for the underdoped films.

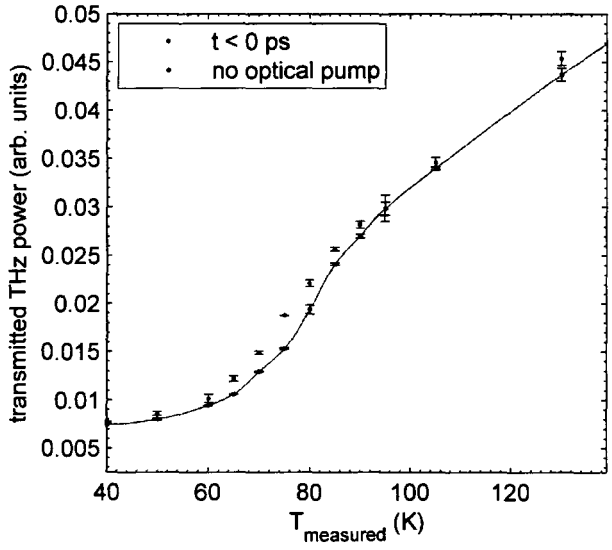

Figure 5.2 A comparison of the temperature trend of the total transmitted THz power spectrum through a steady-state optimally doped film (denoted "no pump") to the film when optically excited with a repetition rate of 1 KHz. The increase in temperature due to a repetitive optical excitation is apparent.

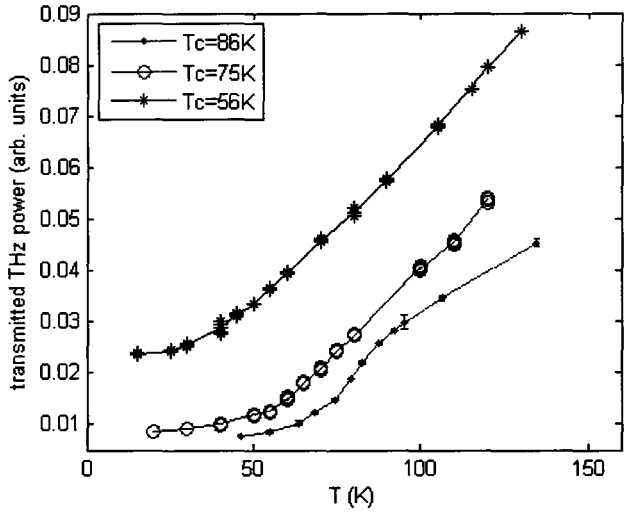

Figure 5.3 The temperature trend of the transmitted THz power for 3 samples: underdoped YBCO, T_c = 56 K , T_c = 73 K, and optimally doped YBCO T_c = 86 K.

The optical conductivity gives valuable spectral information about the steady-state properties of a YBCO thin film. Figure 5.4 shows the real part of the optical conductivity above T_c, while the imaginary component is shown in Figure 5.5. The shape of the real and imaginary parts of the optical conductivity in these figures is consistent with the Drude model. Above T_c, the real part of the conductivity increases as the temperature is decreased due to a reduction in the scattering rate. The imaginary part also increases, consistent with the Kramers-Kronig relations.[125] The imaginary part of the conductivity follows the integral of the real part of the optical conductivity weighted by the square of the frequency:

$$\sigma_2(\omega) = \frac{-2\omega}{\pi} P \int_0^{\infty} \frac{\sigma_1(\omega')d\omega'}{(\omega'^2 - \omega^2)}, \quad \sigma_1(\omega) = \frac{2}{\pi} P \int_0^{\infty} \frac{\omega'\sigma_1(\omega')d\omega'}{(\omega'^2 - \omega^2)} \qquad 5.1$$

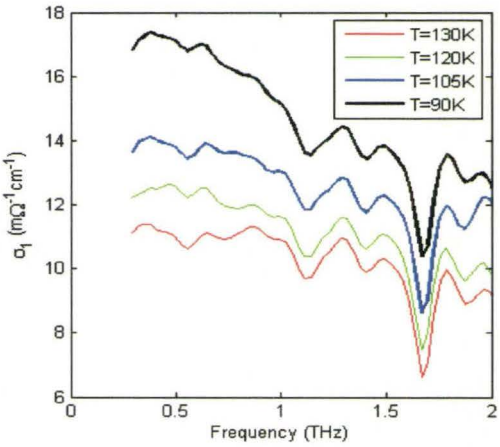

Figure 5.4 The real part of the conductivity for an optimally doped YBCO thin film (T_c= 86 K) in the normal state. Above T_c, the real part of the conductivity decreases with increasing temperature. The dip at 1.7 THz is a water absorption line.

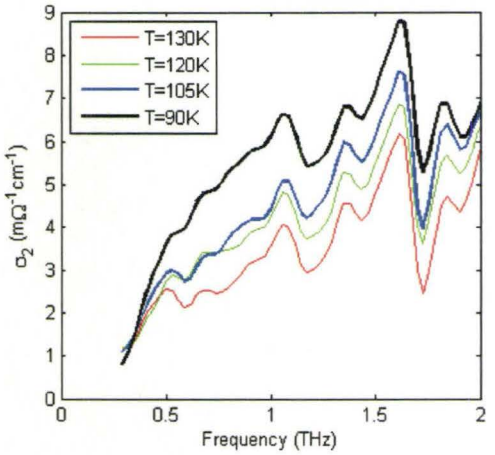

Figure 5.5 The imaginary part of the conductivity for an optimally doped YBCO thin film (T_c = 86 K) in the normal state. Above T_c, the imaginary part of the conductivity is small, and decreases with temperature. The dip at 1.7 THz is a water absorption line.

where P denotes the Cauchy principal value of the integral. Thus, if the real part of the optical conductivity is flat, one would expect the imaginary part to have a shape similar to that shown in Figure 5.5.

For temperatures below T_c, the imaginary part of the optical conductivity changes dramatically due to the formation of the superconducting condensate, as seen in Figure 5.6. A comparison of the measured THz conductivity to the measurements taken by other groups[32,39,67,69] is shown in Figure 5.7. The perfect conductivity of the condensate leads to a delta function at zero frequency in the real component of the conductivity. THz spectroscopy cannot measure this delta function directly but from the Kramers-Kronig relations and London equations it can be shown that the delta function leads to a $1/\omega$ dependency of the imaginary part of the optical conductivity. Below 60 K, the transmitted THz power is not strongly dependent upon the temperature (see Figure 5.6). This is due to the penetration depth levelling off to the $\lambda(0)$ value as the temperature decreases.

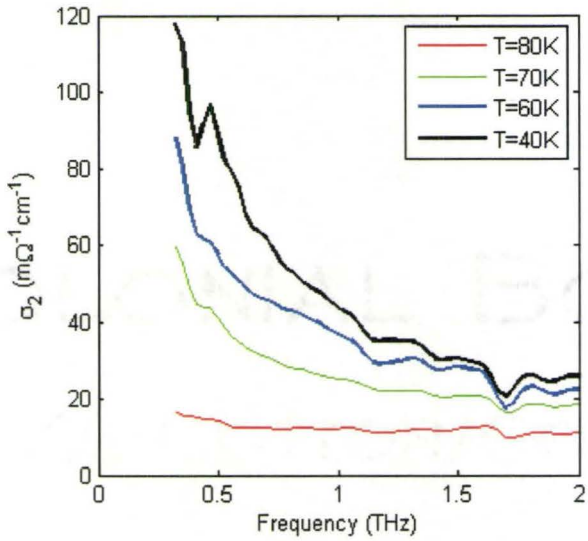

Figure 5.6 Imaginary part of the steady-state conductivity below T_c for an optimally doped YBCO thin film having T_c = 86 K. The 1/ω dependency of σ_2 due to the superconducting condensate can be seen clearly. As the temperature decreases the conductivity is enhanced by the opening up of the superconducting gap.

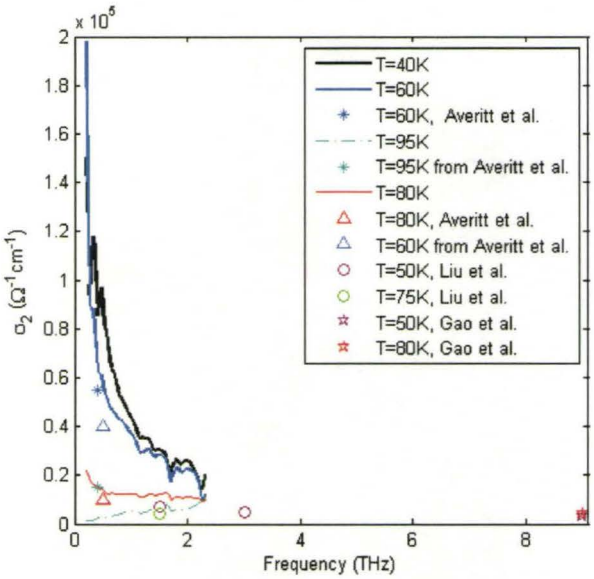

Figure 5.7 A comparison of the imaginary part of the conductivity measured by various groups to the measured THz conductivity[32,39,67,69] for an optimally doped film in equilibrium.

The imaginary part of the conductivity is dominated by the superconducting superfluid, but at non-zero frequencies the real part depends entirely on the normal quasiparticles. Figure 5.8 shows that the real part decreases to almost zero as the temperature decreases. This indicates that as the temperature decreases the superconducting fraction increases and the number of quasi-particles in the normal state decreases. The temperature dependence of the real part of the conductivity is less dramatic than it is in the imaginary part, and there is no drastic change in the frequency dependence of the real part of the conductivity going through the transition temperature.

Figure 5.9 shows the temperature dependence of the real part of the conductivity at 0.7 THz. This is consistent with previous studies of the conductivity.[29,32,69,126] The peak below T_c is not related to the NMR Hebel-Slichter peak, which is absent in D-wave superconductors.[127,128,129,130] The increase in conductivity above T_c is due to the increase in the scattering time with temperature. However below T_c, the normal fraction also decreases as the temperature decreases due to the formation of the superconducting condensate. At low enough temperatures this overwhelms the effect of an increasing τ

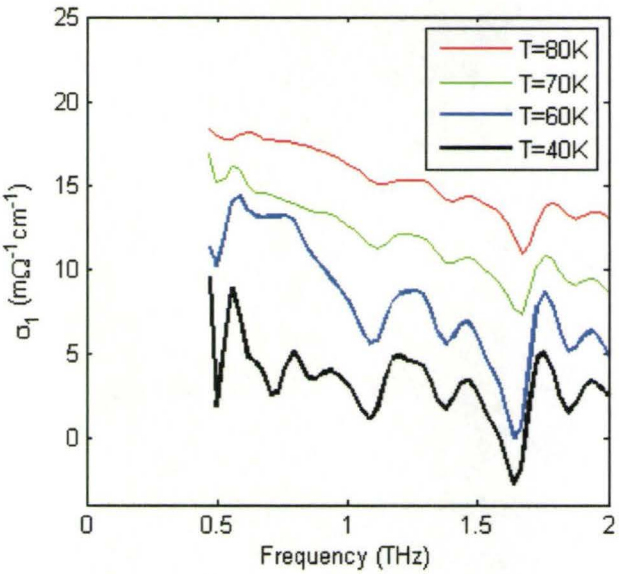

Figure 5.8 Real part of the steady-state conductivity below T_c for an optimally doped YBCO thin film, T_c = 86 K. Note that as the temperature decreases, the real part of the conductivity goes to zero.

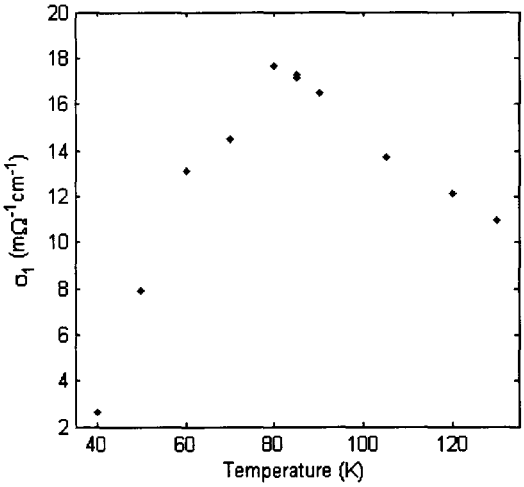

Figure 5.9 The temperature dependence of the real part of the optical conductivity at 0.7 THz for an optimally doped film, T_c = 86 K. This temperature trend is consistent with previous reports.[29,69,126]

and leads to a diminishing σ_1 with temperature. Overall, the evolution of the real component of the conductivity with temperature is less dramatic that for the imaginary contribution and does not present a clear signature coinciding with the onset of the condensate formation.

5.2 Steady-state optimally doped YBCO

This section will discuss a two-fluid analysis of the steady-state optical conductivity of an optimally doped YBCO thin film. Through this analysis, the temperature dependence of the scattering time, and the superconducting fraction can be determined allowing an estimate of the optical conductivity at intermediate temperatures. This will allow one to determine if there exists non-thermal features in the conductivities for photo-excited samples. A simple Drude model is used above the transition temperature, and was found to be a reasonable approximation for the conductivity for the measured frequency range. The DC component of the Drude conductivity can be found by extrapolating the real part of the measured conductivity to zero as seen in Figure 5.10. The discrepancy between the projected σ_{DC} and the conductivity calculated from the

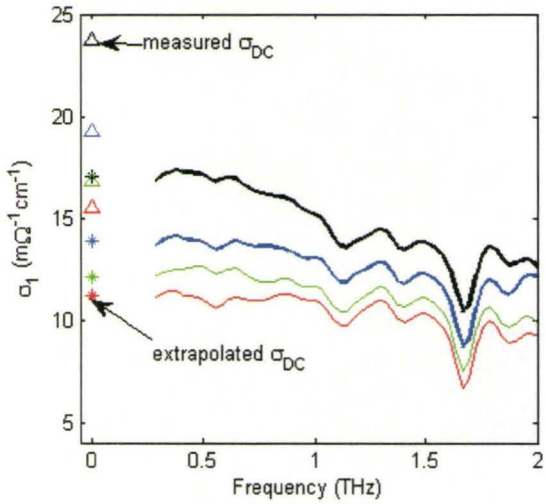

Figure 5.10 Shown here, is the σ_{DC} extrapolated from the real part of the conductivity obtained from THz measurements on a steady-state optimally doped YBCO film compared to the $\sigma_{DC}(T)$ obtained from resistivity measurements (triangle symbol) for the same film at T = 130, 120, 105 and 90 K (starting from the bottom). The DC conductivities obtained from resistivity measurements are consistently 28% higher than the conductivity obtained from THz measurements.

resistivity measurement at each temperature is about 28%. Such a discrepancy is not surprising, as the resistivity measurement relied on an estimation of the shape and size of the film/contact pads.[131] In the analysis that follows, the extrapolated THz conductivity is used to obtain σ_{DC} so as to maintain consistency.

Using σ_{DC} and assuming a Drude form for the measured conductivity, the scattering time can be calculated. Taking the scattering time to be constant over the 0.5 – 2.0 THz range, a mean scattering time can be determined after filtering out the water lines* (shown in Figure 3.3). The result of this analysis is shown as a function of temperature in Figure 5.11. The number density of quasiparticles can then be found using the scattering time and the DC conductivity: $n = \frac{m\sigma_{DC}}{\tau e^2}$. The number density of quasiparticles is shown in Figure 5.12. Making the assumption that the total number of quasi-particles is independent of temperature, n_0 is found to be $1.20 \times 10^{27} \pm 0.03 \times 10^{27}$ m^{-3}. The fit to the conductivity is shown in Figure 5.13.

* Frequencies filtered out due to water absorption are: 1.05 - 1.26 THz, 1.38 - 1.43 THz, 1.55 - 1.82-1.96 THz, and 2.1 - 2.3 THz

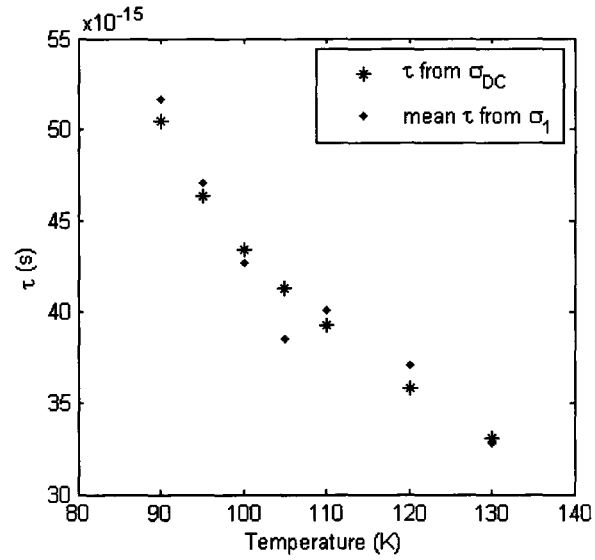

Figure 5.12 The scattering time for an optimally doped film above T_c, calculated from the real part of the Drude conductivity compared to the scattering time calculated from the DC conductivity.

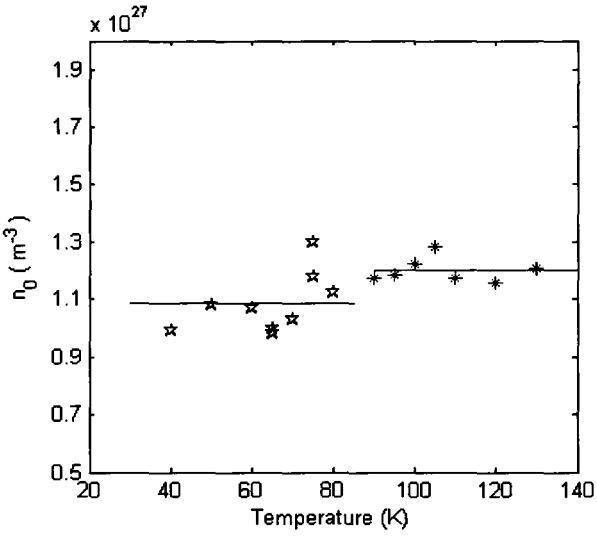

Figure 5.11 The total number density of quasi-particles calculated for each temperature for a steady-state optimally doped YBCO thin film. The calculated number of quasi-particles is fairly consistent for each temperature. The estimated number of quasi-particles found from the two-fluid model fit to the conductivities below T_c has a reasonable agreement with the above T_c values.

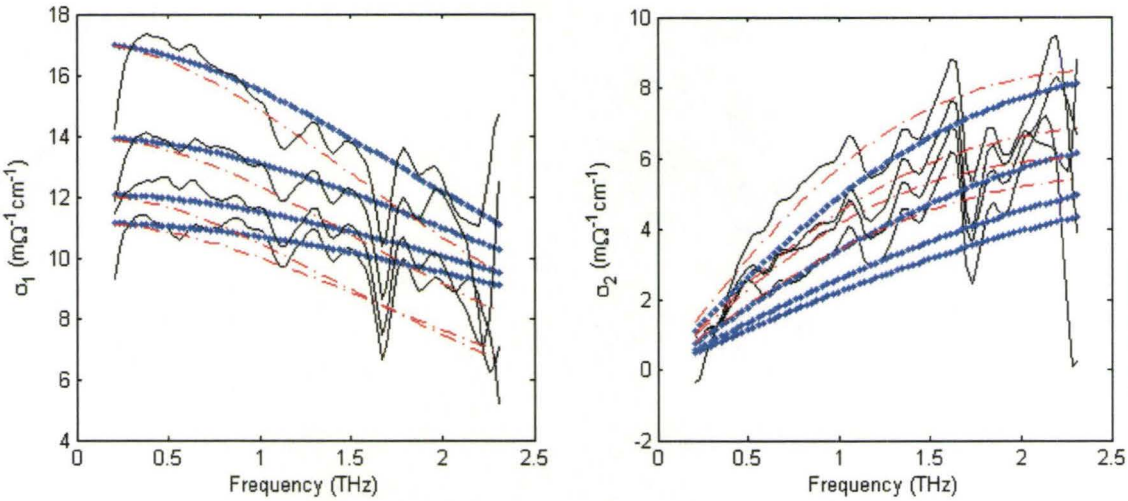

Figure 5.13 A comparison of the experimental optical conductivity of an optimally doped film Drude fits for various temperatures. The solid line shows the experimental conductivity, the dotted blue line shows the fit using τ found from the DC conductivity and the dashed red line shows the case where τ was fit using the imaginary part of the optical conductivity. The temperatures shown are from top to bottom: T = 90, 105, 120, and 130 K

5.2.1 Fitting the conductivity below T_c

Below T_c, the hydrodynamic two-fluid model is used to extrapolate between temperatures at which the conductivity was measured experimentally. In this model, the normal fraction makes a Drude-like contribution to the conductivity i.e.:

$$\sigma_n = \frac{n_n e^2 \tau}{m(1 - i\omega\tau)} \qquad 5.2$$

where n_n is the number density of normal electrons. The condensate only contributes to the imaginary component of the conductivity and is taken to be:

$$\sigma_{2s} = \frac{n_s e^2}{m\omega} \qquad 5.3$$

where n_s is the number density of superconducting electrons. Predicting the optical conductivity for temperatures below T_c requires that the scattering time, the superconducting fraction, and the total number density of quasi-particles be determined

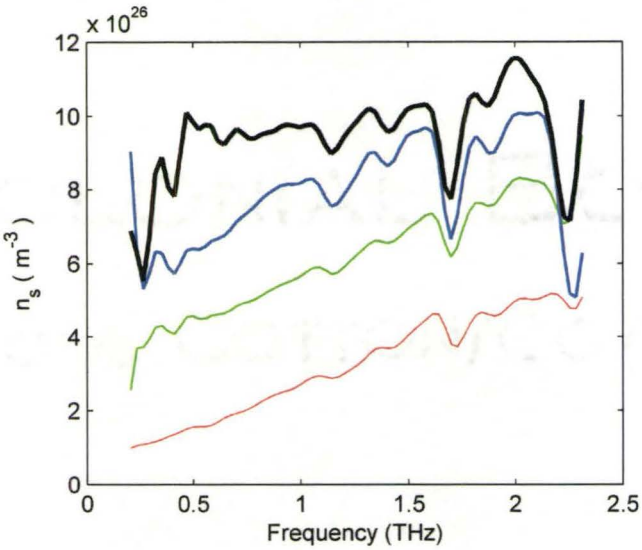

Figure 5.14 A calculation of n_s for each frequency, neglecting the normal contribution to σ_2 for a steady-state optimally doped film at T=40 (black), 60 (blue), 70 (green) and 80 K (red). The frequency dependency illustrates that the normal contribution must not be excluded.

as a function of temperature. As a first approximation, the number density of superconducting quasiparticles can be estimated by assuming a negligible contribution of the normal states to the imaginary part of the optical conductivity.[132] If this assumption is valid, then the calculated n_s should not show any spectral dependency. Figure 5.14 shows the calculation of n_s at each frequency sampled for temperatures ranging from T = 40 - 80 K. Neglecting water absorption lines, it can be seen that n_s is relatively flat for low temperatures, but as T increases a frequency dependence becomes clear, illustrating that this assumption is not valid. Therefore, the normal contribution must be included in the analysis of the imaginary part of the conductivity.

In this analysis, the imaginary part of the conductivity is fitted to σ_2 with the form taken from the full hydrodynamic two-fluid model:

$$\sigma_2 = \omega\tau\sigma_{1\exp} + \frac{n_s e^2}{m\omega} \qquad 5.4$$

using an unconstrained nonlinear optimization routine,[133] where n_s and τ are fitting parameters. Frequencies below 0.2 THz are disregarded due to the weak amplitude of the

THz pulse at these frequencies, and above 1.55 THz due to the concentration of large water absorption lines. This fit, shown in Figure 5.16, assumes a frequency independent scattering time, which is a reasonable starting point for the analysis and is sufficient for the scope of this thesis. The fit at temperatures near T_c is reasonably good, but as the temperature decreases, the fit is less satisfactory. For low temperatures, the fit of the scattering time is not reliable, since the imaginary part of the optical conductivity at low temperatures is dominated by the condensate. The number density of superconducting quasi-particles, n_s, can be seen in Figure 5.15.

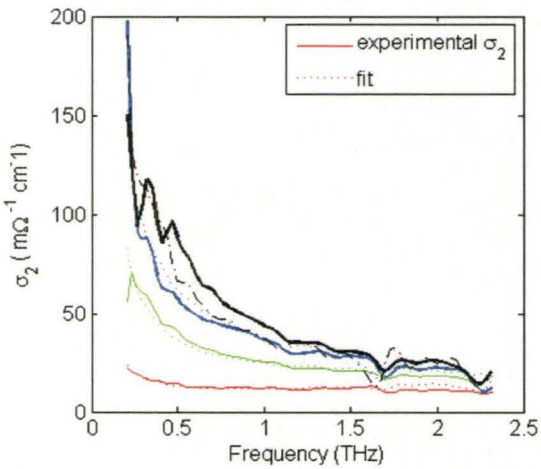

Figure 5.16 Initial fits to the imaginary part of the optical conductivity of an optimally doped film for T=40 (black), 60 (blue), 70 (green) and 80K (red). The quality of the fit is better for higher temperatures.

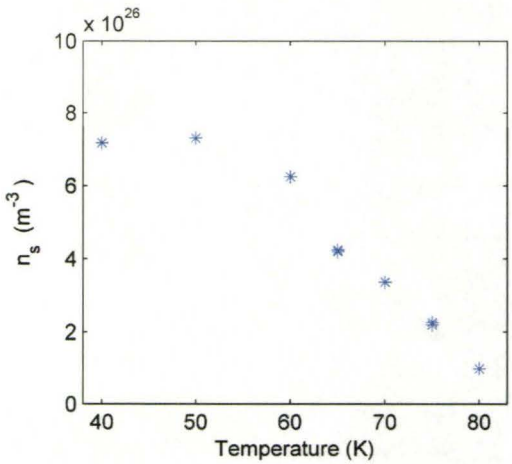

Figure 5.15 The number of superconducting quasiparticles for an optimally doped film determined through a fit to the imaginary part of the conductivity which is based on the two-fluid model.

As seen previously, the real part of the optical conductivity only depends on the scattering time and the number density of normal quasi-particles:

$$\sigma_n = \frac{n_n e^2 \tau}{m(1 - i\omega\tau)}. \qquad 5.5$$

The number density of normal quasiparticles can be determined directly from $\sigma_1(\omega)$ and the previous fit of τ. Filtering out the water lines, and taking the mean value gives a reasonable estimate of the number of normal quasiparticles, as shown in Figure 5.17. The total number of quasi-particles is found from $n_n = n_0 - n_s$. The estimated total number of quasiparticles is fairly constant across the entire temperature range. The average of n_0 is $1.08 \times 10^{27} \pm 0.08 \times 10^{27}$ m^{-3}, which is close to the value of n_0 obtained from the conductivity above T_c ($1.20 \times 10^{27} \pm 0.03$ m^{-3}).

Taking the total number of quasi-particles to be temperature independent, a more accurate estimation of the scattering time can be obtained by fitting the two-fluid model to the real part of the optical conductivity. Figure 5.18 shows the scattering time found using this method. There is reasonable agreement with values found from the scattering

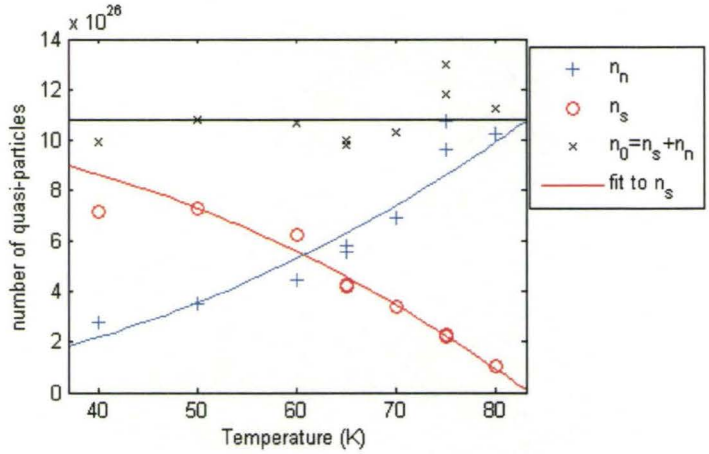

Figure 5.17 The number of superconducting quasi-particles, n_s (red circles), was found by fitting σ_2 to the imaginary part of the two-fluid model. The number of normal quasi-particles, n_n (blue crosses), was calculated from σ_1 and the estimation of τ found from the fit to σ_2. The total number of quasi-particles, n_0 (black x's), was found from $n_0 = n_s + n_n$ and is fairly constant across the entire temperature range. The black line is a guide to the eye to illustrate this. The red line is a fit to n_s, and the blue line uses the same fit, with n_s subtracted from the mean number of total quasi-particles.

time by previous groups,[39,67,69] especially if one considers the significant differences in film quality. The scattering time at T = 40 K has significant error, which is to be expected given that the real part of the conductivity is near zero at this temperature. A comparison of the superconducting fraction found using the methods outlined here to the temperature trend of the superconducting fraction found from the penetration depth by Hardy *et al.*[71] is shown in Figure 5.19.

With this improved scattering time, the previous fit for n_s, and the average value for n_0, the two-fluid model is in good agreement with both the real and imaginary parts of the conductivity calculated from the THz transmitted electric field, as seen in Figure 5.20.

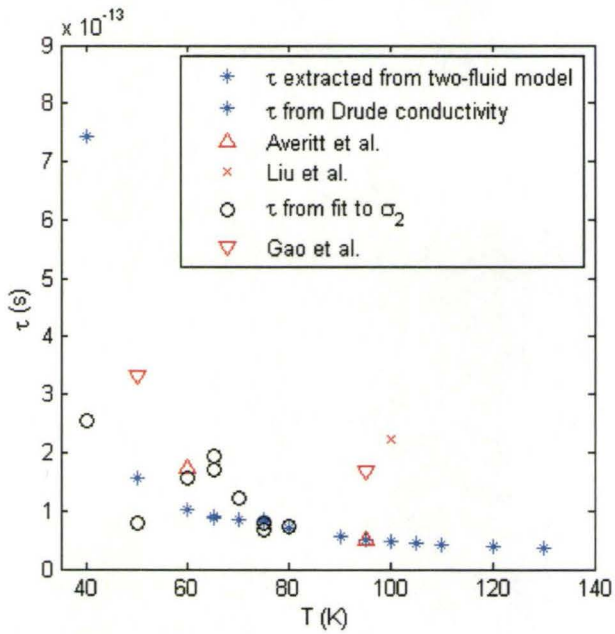

Figure 5.18 For an optimally doped film, the scattering time from the fit to σ_1 for $T < T_c$ (blue asterisk) is compared to the scattering time from a fit to σ_2 (black circles) and to various results obtained from other groups (39, 67, 69). The scattering time found for $T > T_c$ is also shown. Note that the fit to σ_1 gives a much smoother temperature dependence for the scattering time than the fit to σ_2.

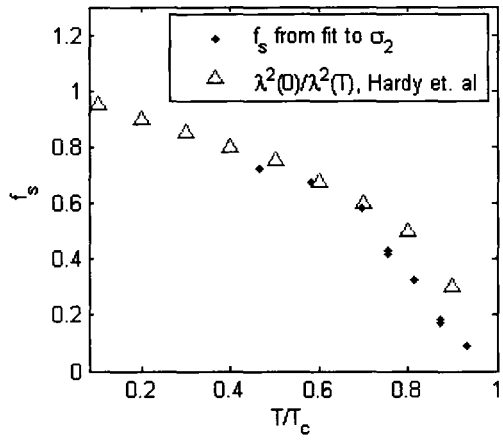

Figure 5.19 A comparison of the superconducting fraction found from a fit of the two-fluid model to the measured conductivity of an optimally doped film and the superconducting fraction obtained from penetration depth measurements by Hardy *et al.*[71] Note that our data appears to follow a similar linear trend at low T.

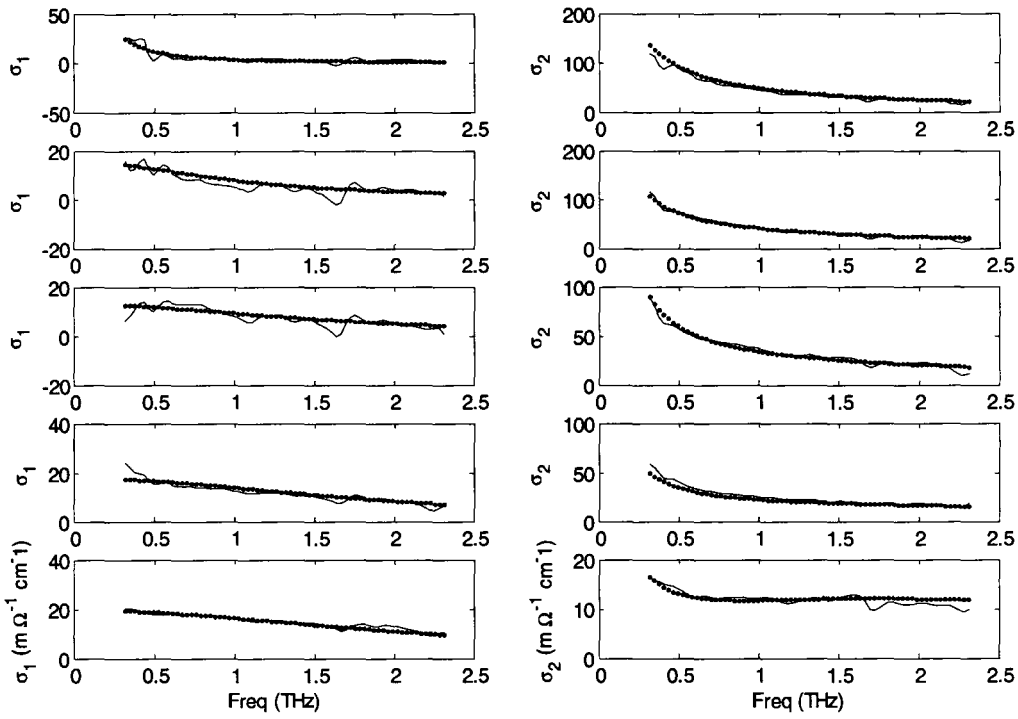

Figure 5.20 Fit of the optical conductivity of optimally doped YBCO to the hydro-dynamic two-fluid model. The blue dotted line is the fit and the solid line is the experimental conductivity. On the left is shown σ_1, and on the right is shown σ_2, for T=40, 50, 60, 70 and 80 K starting from the top.

5.2.2 Modelling the temperature dependence of τ and f_s

By modelling the behaviour of the n_s(T) and τ(T) it is possible to calculate the optical conductivity at intermediate temperatures. In the analysis of the film's response to optical excitation, this allows for the separation of any non-thermal behaviour associated with optical excitation from the inevitable temperature increase resulting from optical excitation. Above T_c, the behaviour of the scattering time can be fit to an exponential. The log of the scattering time can be fit it to a straight line, thus giving the necessary parameters for an exponential fit: $\tau(T > T_c) = e^{-AT+B}$, where A was found to be 0.01 and B was -29.62. This fit is shown in Figure 5.21. Below T_c, the scattering rate can be approximated as a quadratic as seen in Figure 5.22. While the resulting fit provides a useful interpolation through the temperature of interest, it becomes unphysical below about 35K. The fit to the scattering time is shown in Figure 5.23.

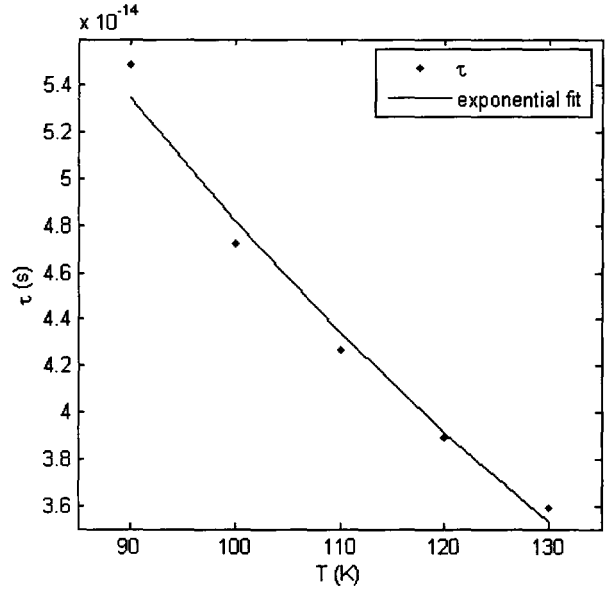

Figure 5.21 An exponential fit to the temperature dependence of the steady-state scattering time above T_c (86 K).

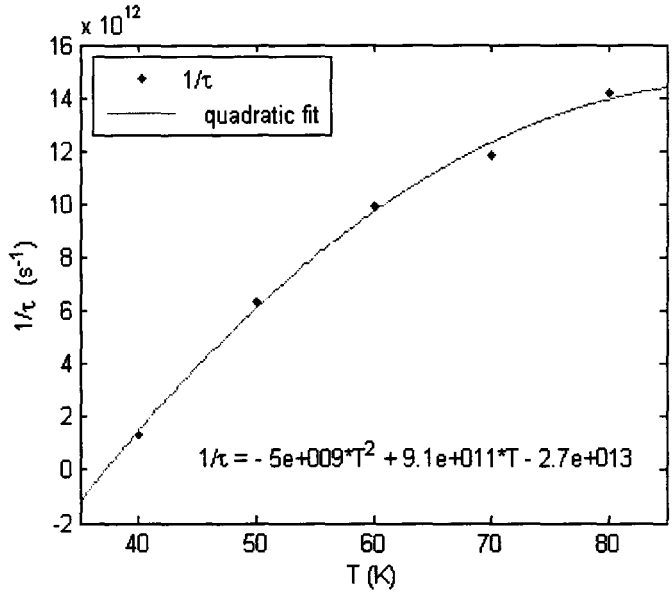

Figure 5.22 A quadratic fit to the temperature dependence of the steady-state scattering rate below T_c (86K).

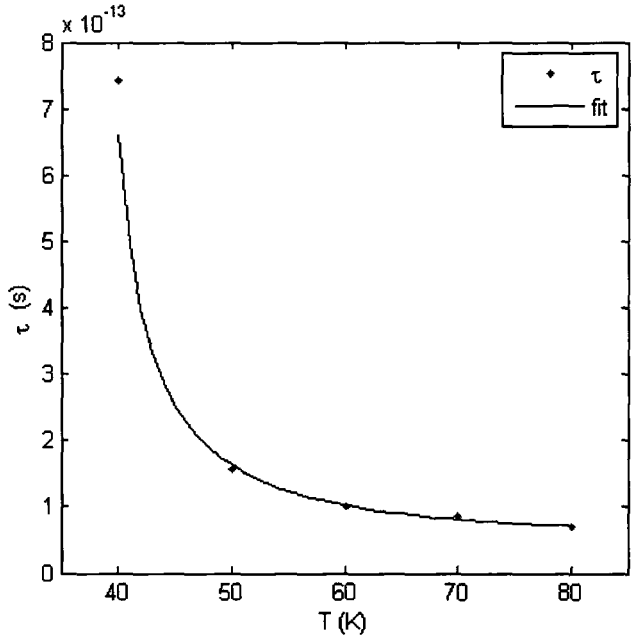

Figure 5.23 Fit to the steady-state scattering time below T_c (86 K).

Figure 5.24a shows a plot of the value of f_s extracted from a fit of the imaginary conductivity to the functional form $f_s = 1 - A\left(\frac{T}{T_c}\right)^B$, where A is found to have a value of 1.1, and B = 2.2 which is close to the fit of A = 1, B = 2.1 reported elsewhere.[134,135] This fit, combined with estimates for the total quasiparticle density and scattering rates, is used to calculate optical conductivities at intermediate temperatures for comparison with photo-excited conductivities. Potential alternative fits are shown in Figure 5.24b. One fit uses the same model as above, but with A set to unity. This results in a fitted value for B of 2.7. Removing the assumption that the normal fraction goes to zero for low temperatures, the fit becomes $f_s = A - \left(\frac{T}{T_c}\right)^B$ where A = 0.81 and B = 3.34. This fit, however, is not significantly better for the temperature range shown, and does not agree with previous results for the superconducting fraction at low temperatures.[126] Thus, the fit used in this thesis is the more familiar $f_s = 1 - A\left(\frac{T}{T_c}\right)^B$, where A = 1.1, and B = 2.2, as this appears to be the best fit for the temperature range of interest, and more closely agrees with previous results.

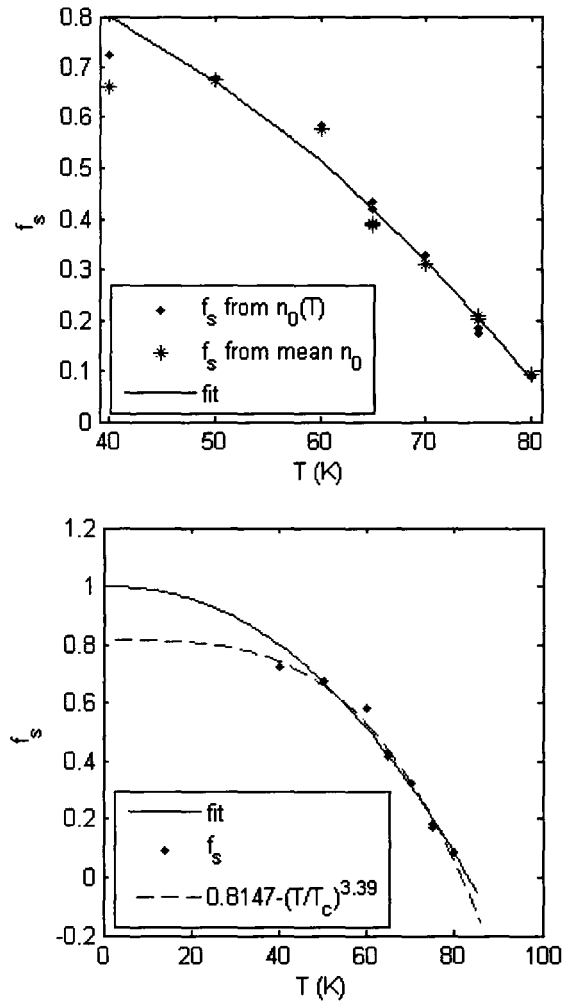

Figure 5.24 The superconducting fraction for a steady-state optimally doped YBCO thin film

a) Top: The fit to the superconducting fraction: $f_s = 1-1.1(T/T_c)^{2.2}$

b)Bottom: alternate fits - the fit $f_s = 1-(T/T_c)^{2.7}$ is shown in blue, and the fit $f_s = 0.8-(T/T_c)^{3.4}$ is shown in red.

5.2.4 Penetration depth

The penetration depth is an important experimental parameter that can be calculated using the optical conductivity and the scattering time. As was seen in Figure 5.16, it is not correct to ignore the normal contributions to the imaginary component of the conductivity. The appropriate expression for the penetration depth becomes:

$$\lambda(T) = \frac{1}{\sqrt{\mu_0 \omega(\sigma_2 - \sigma_1 \omega\tau)}} \qquad 5.6$$

where μ_0 is the permittivity of free space. Figure 5.25 shows the penetration depth calculated using the fitted values of the optical conductivity instead of the experimental data so as to avoid errors due to the water lines. From the equation $\lambda(0) = \lambda(T)\sqrt{f_s(T)}$ an estimate of the penetration depth at T = 0 K can be calculated using the measurements at each temperature. Figure 5.26 shows that each temperature yields a consistent estimate of $\lambda(0)$. The mean value, $\lambda(0) = 162 \pm 6$ nm, obtained agrees well with previously reported values of 150 nm[136] determined from kinetic inductance measurements and 148 nm[135] found using THz spectroscopy. Deviations between different samples are expected. The plasma frequency, given as $\omega_p = c/\lambda(0)$, is then found to be $1.8 \times 10^{15} \pm 0.5$ Hz. The plasma frequency for single crystal YBCO was found to be 2.1×10^{15} Hz by Hardy *et al.*,[71] whereas the plasma frequency for a thin film has a somewhat smaller reported value of 1.5×10^{15} Hz.[137] By then using the model for the superconducting fraction and the estimated value for the penetration depth at T = 0 K, the penetration depth can be determined at any temperature, as shown in Figure 5.25.

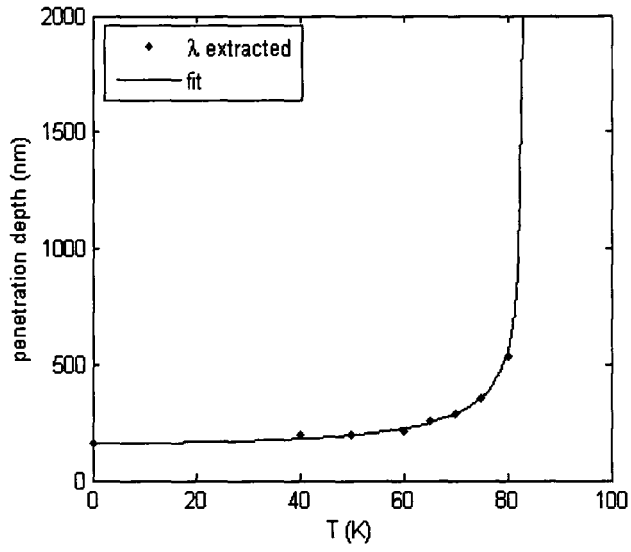

Figure 5.25 The penetration depth extracted from the optical conductivity and the scattering time (red dots) of a steady-state optimally doped film compared to penetration depth calculated from the modeled superconducting fraction and λ(0). The excellent agreement confirms the steady-state analysis of the film.

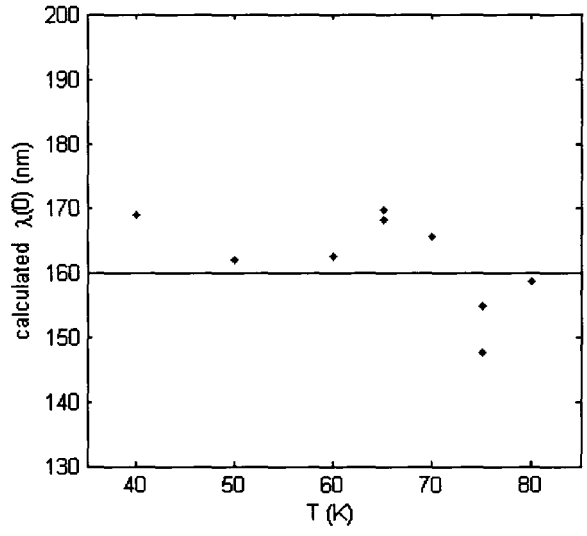

Figure 5.26 λ(0) found from λ(T) and f_s(T) for an optimally doped YBCO thin film. Each temperature gives a consistent value for λ(0). The horizontal line at 162 nm shows the mean value.

5.3.1 Film dynamics following optical excitation

As discussed in section 1.6, the optical excitation of a YBCO thin film has a number of effects on the system. Initially, the energy from the optical pulse will be transferred to the electronic system, perturbing the condensate by breaking Cooper pairs and generating high energy normal quasiparticles. These high energy quasiparticles will cascade down in energy, generating both phonons and breaking additional Cooper pairs. The electronic system is expected to rapidly form a quasi-thermal state with a temperature that is higher than the lattice temperature. As the electronic temperature comes to equilibrium with the lattice, the superconducting condensate will reform. An indication of the timescale required for the return of the sample to equilibrium can be obtained by looking at the total THz transmission of an optically excited thin film as a function of time. Figure 5.27 shows the transmitted THz radiation for three different temperatures for an optimally doped YBCO film and an excitation power corresponding

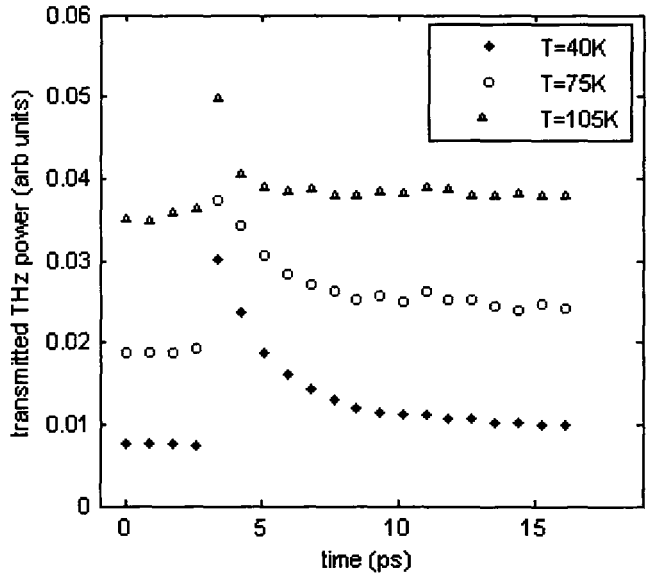

Figure 5.27 Temporal response of an optimally doped YBCO thin film to a 28 mW IR pulse above and below T_c, where $t = 0$ ps is arbitrarily chosen. The peak corresponds to the time when the IR pump pulse arrives at the sample coincident with the most energetic part of the THz pulse. An initial fast partial recovery followed by a slower recovery is consistent with previous findings.

to 28 mW†. Figure 5.27 shows the transmitted power spectrum, i.e. the integrated square of the measured electric field. The position of $t = 0$ is arbitrary in these figures. Looking at times before the peak one can get a sense of the steady state transmission as a function of temperature. The film shown here has a T_c of 86 K and is 40 nm thick. Similar optical excitation studies have been reported for YBCO and BSSCO using THz, [32,86,87] and optical probe techniques.[58,62,80,89,138] There is a fast partial recovery lasting a few picoseconds, followed by slow recovery, which has previously been held as a purely thermal response.[62,80] For initial temperatures above T_c, the scenario above is altered since there are no Cooper pairs to break. Experimentally, it has consistently been shown that the initial recovery of the transmission is much faster above T_c than below.

Figure 5.28 shows the optical excitation of a 100 nm thick underdoped thin film with a $T_c = 73$ K. The recovery above T_c appears to be slower than for optimally doped film which may be evidence for the existence of pre-formed Cooper pairs in this sample at 100 K. Figure 5.29 shows the optical excitation of an underdoped film for three

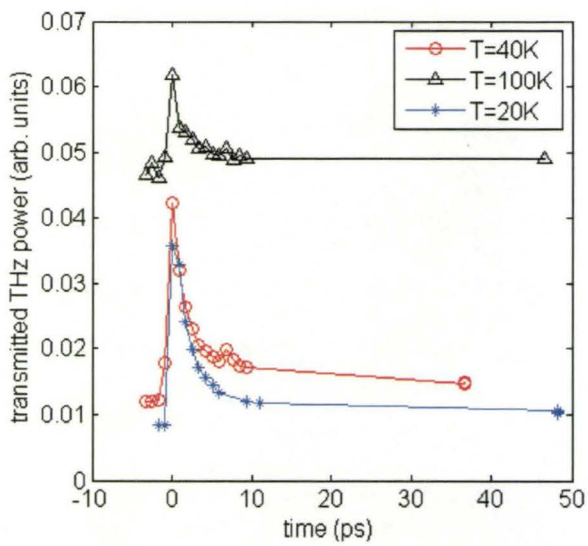

Figure 5.28 Temporal response of an underdoped YBCO thin film (T_c= 73 K, 100 nm thick) to a 24 mW IR pulse above and below T_c.

† A 28 mW average excitation power is equivalent to a fluence of 152 J/cm^2 for each pulse.

different excitation powers. The film shown is the same film as in Figure 5.28 and is initially at 40 K, well below T_c. It is clear that although the magnitude of the effect is reduced for lower optical excitations, the basic response is similar. The initial recovery of the film is faster for lower optical excitations. Previous studies of the reflectivity of YBCO using optical pump optical probe spectroscopy show a dramatically slower recovery at early timescales for lower optical excitations for both optimally doped and underdoped crystals.[58,62,89] The observed change in the total transmitted THz electric field following optical excitation is generally faster than the observed change in the optical reflectivity reported by Gedik *et al.*[58] It is unclear if the difference in the power dependence of the recovery should be attributed to differences between the optical excitation of single crystals and thin films, or the fact that a probe at optical frequencies

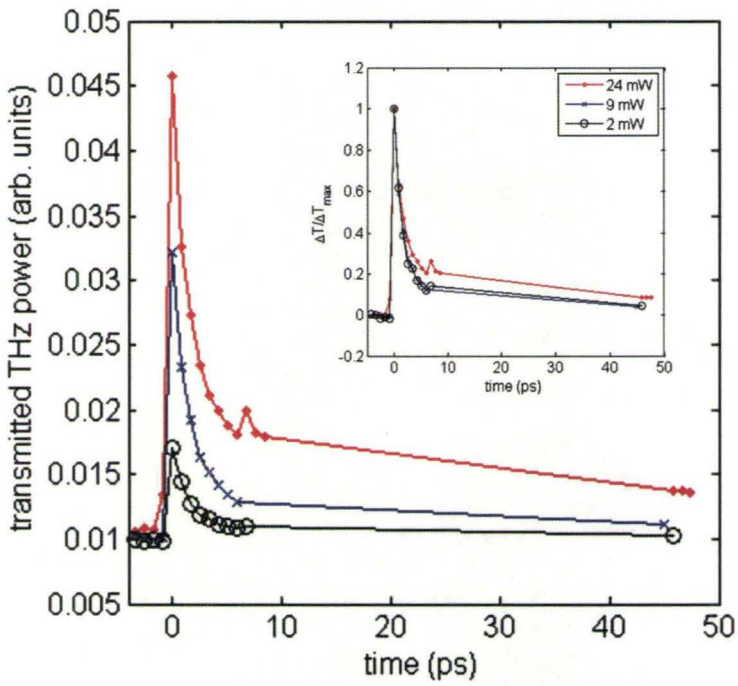

Figure 5.29 The effect of different levels of optical excitation for an underdoped film (T_c = 73 K) at T = 40 K. Three pump powers are shown: 24 mW (red), 9 mW (blue), and 2 mW (black). The inset shows the change in transmission normalized by the maximum change in transmission for these three powers. Note that the early recovery is faster for lower optical powers and that there is no significant difference in the recovery rate between the 9 and 2 mW optical pump powers. The peak at ~8 ps is due to the internal reflection of the excitation beam from the back surface of the substrate.

measures different properties than the THz probe. Observed timescales associated with the recovery of YBCO thin films using optical pump THz probe spectroscopy from Averitt *et al.* show reasonable agreement with our results.[32,139]

5.3.2 Specific heat

If the response at long timescales is purely thermal, the temperature rise in the film due to optical excitation can be predicted using the temperature dependence of the film's steady state THz transmission as a thermometer. Figure 5.30 shows the temperature trend of THz transmission for an optimally doped film for both steady state (non-excited) conditions, and 50 ps after optical excitation. Above T_c, the transmission is linear with temperature, and below T_c, the shape of the curve is determined by the temperature dependent penetration depth. Using the equilibrium temperature response as a guide, the apparent increase in temperature due to the optical excitation can be determined. Due to the repetitive nature of the optical excitation, during the experiment

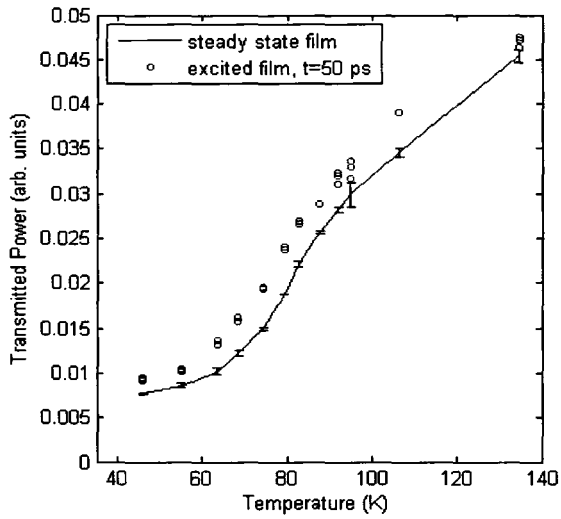

Figure 5.30. The transmitted THz power through an optimally doped thin film is shown as a function of temperature. The open circles show the response of the film 50 ps following optical excitation, with the temperature corrected for background laser heating.

there is a ~3 K increase in the background temperature of the film relative to substrate as was shown in Figure 4.12. Therefore, for pump-probe results, the temperature of the film prior to optical excitation must be corrected as it will be higher than the recorded temperature of the cryostat cold finger. Figure 5.31 shows the apparent temperature increase at 50 ps after the optical excitation for an optimally doped YBCO film. The results of Bessergenev *et al.*[140] showing the total specific heat of an optimally doped YBCO thin film are shown in Figure 5.32. One can use the energy of the laser pulse and the specific heat (C_v) to predict the temperature increase:

$$\Delta T = \frac{\Delta U}{C_v} \qquad 5.7$$

An estimate of ΔU, the absorbed energy of the optical pump, can be determined from the measured average power of the pump at the input of the cryostat. The transmission through the cryostat window and the reflection must be taken into account. The power available to the film is given by:

$$P = P_i T_{window} (1 - R_{YBCO}) \qquad 5.8$$

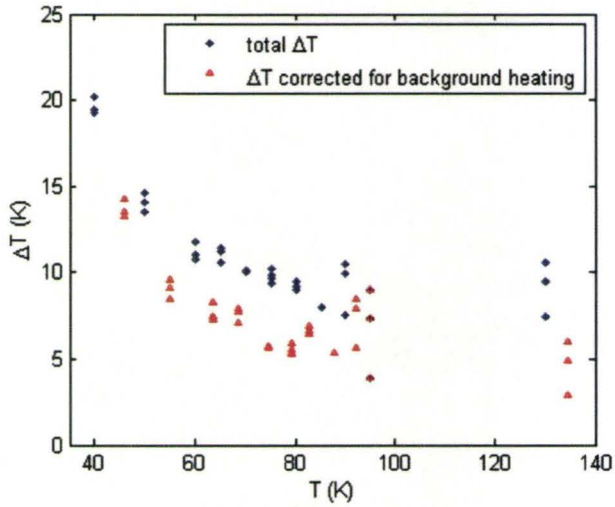

Figure 5.31 The apparent increase in temperature due to laser heating of an optimally doped film 50 ps after the arrival of the optical pulse. Note that the repetitive nature of the optical excitation increases the background temperature of the film.

where P_i is the measured laser power at the cryostat window. The transmission through the window, T_{window} (60 μm polypropylene), is 90%[141] while the reflectivity of YBCO at the pump wavelength, R_{YBCO}, is 16 % at T = 100 K and 20% at 300 K.[142] The average pump power at the cryostat[‡] is 28mW, and therefore the maximum power available to the film is 20.2 mW. The repetition rate of the laser is 1 KHz, so the energy per pulse will be 2.02×10^{-5} J. The spot size[§] is estimated to be 0.25 cm^2 and the film thickness is assumed to be 36 nm. Thus the estimated energy incident upon the film is U = 22.4 J/cm^3. Not all of this energy is absorbed by the film.

The film is thin enough that a significant amount of energy is transmitted through the film. The measured optical power transmitted through the sample and cryostat is ~ 6 mW. Using the transmitted power, it is possible to construct an estimate for the optical power absorbed by the film. The aperture in the sample holder is smaller than the incident pump beam, and so the reduced spot size of 0.181 cm^2 is used in calculating the

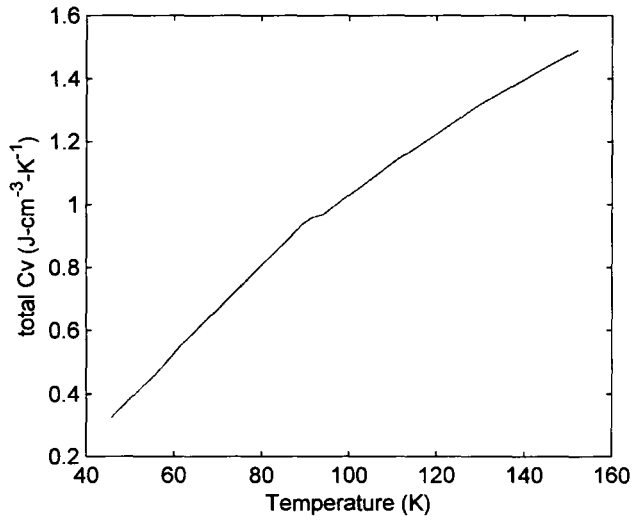

Figure 5.32 The total specific heat for an optimally doped YBCO thin film, T_c = 92.2 K reproduced from Bessergenev *et al.* [140]

[‡] This is measured with a large thermal head power meter and gives the average power of the excitation beam.

[§] The spot size incident upon the sample is determined by the dimensions of the pump mirror, which is smaller than the spot size of the laser. The beam is assumed to be roughly uniform.

energy of the transmitted pump pulse. Thus, the power of the pulse transmitted through the sample, substrate and window is ~ 9.5 J/cm^3. Taking into account loss at the window (10%) and the transmission of 800 nm light through LSAT (80%)[143], the expected power of the pulse leaving the YBCO thin film is 13 J/cm^3.

The power absorbed by the film can be estimated with the equation:

$$P_{out} = (P_{in} - P_{abs})(1 - R_{YBCO}) \qquad 5.9$$

where P_{out} denotes the measured optical power transmitted through the film, P_{in} denotes the optical power incident upon the film and P_{abs} denotes the power absorbed by the film. From Equation 5.9, the energy density absorbed by the film is approximately 5.94 J/cm^3. The increase in temperature due to laser heating using this estimate of the energy absorbed by the film is seen in Figure 5.33. The theoretical estimate for the temperature

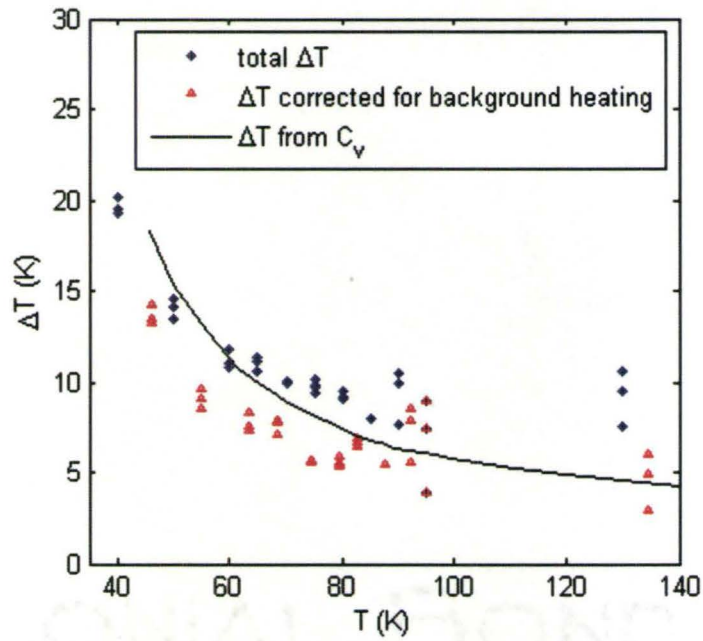

Figure 5.33 A comparison of the expected temperature increase due to laser heating, calculated using the total specific heat and an estimate of the energy absorbed by the film, to the apparent change in temperature of an optimally doped film. Here it can be seen that the expected temperature increase matches fairly well with the data corrected for long timescale background heating.

increase agrees reasonably well with the measured temperature increase. The theoretical estimate, however, is somewhat higher than the measured values that have been corrected for background heating. One would expect the presence of a spinon bottleneck to increase the apparent temperature rise since the deposited energy would not be shared with the phonon modes. Since the apparent temperature at long timescales can be accounted for by the specific heat, there is no observed evidence for a spinon bottleneck.

In Figure 5.34 the effective temperature of the film following optical excitation is converted from the temporal evolution of the transmission. At short times, one would expect this analysis to be invalid. For example, the sample initially at 46 K would require an increased energy density of approximately 19.6 J/cm^3 if the increase in transmission at t = 0 ps were due to a purely thermal effect. This is about 4 times the estimate of the energy absorbed by the film. However for long timescales it is reasonable to expect that the only effect of the optical excitation on the film would be an elevated temperature. For $T \geq T_c$, a similar analysis rules out purely thermal behavior for times less than 4 ps. Above T_c, the increase in transmissivity at 4 ps is still much too large to be purely thermal. It is interesting to note that the initial apparent increase in temperature is similar

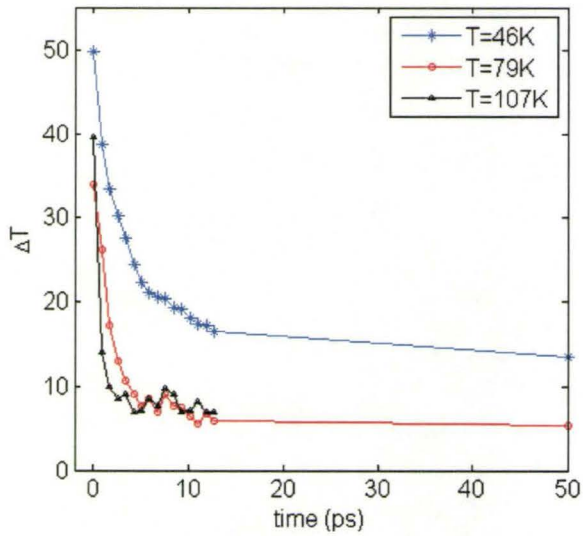

Figure 5.34 The apparent temperature change as a function of time after optical excitation for an optimally doped film above and below T_c (86K). Above T_c, ΔT levels off much faster than below T_c.

for temperatures starting above and below T_c, but that the recovery of the film starting in the normal state is much more rapid. Based on this analysis, it is reasonable to conclude that at early timescales the film's quasiparticles dynamics and the condensate recovery are largely responsible for the decay in THz transmission. While for timescales greater than 10 ps, a purely thermal argument cannot be ruled out to explain the plateau in the transmitted THz power.

5.3.3 Dynamic conductivity

In order to further probe the dynamics of the system, the non-equilibrium optical conductivity can be examined. If the increase in transmitted THz power is due to a purely thermal effect, then the optical conductivity should match that of a film at an elevated temperature. Figure 5.35 shows the real part of the optical conductivity of an optimally doped film after optical excitation for an average pump power of 20.3 mW for different delays. Figure 5.36 shows the recovery of the imaginary part of the optical conductivity derived from the same experiment. The $t<0$ ps conductivity is the conductivity prior to excitation and is given for comparison.

The imaginary part of the conductivity is of particular interest as it contains the contribution from the superconducting condensate. Thus, if the condensate has fully recovered one would expect σ_2 to exhibit the $1/\omega$ behavior as previously discussed in Chapter 1. The destruction of the superconducting response in the THz regime at short times is clearly depicted with σ_2 taking the same general form and magnitude as in the normal state. The conductivity at t = 0 ps does not appear to show a full destruction of the superconducting state as seen in Figure 5.36. This might be associated with a delay in the destruction of the superconducting state, but it is important to remember that the THz pulse has a longer duration than the optical pulse, and that a convolution of the THz pulse with the optical response must be considered for any analysis of the early timescales to be meaningful.[75]

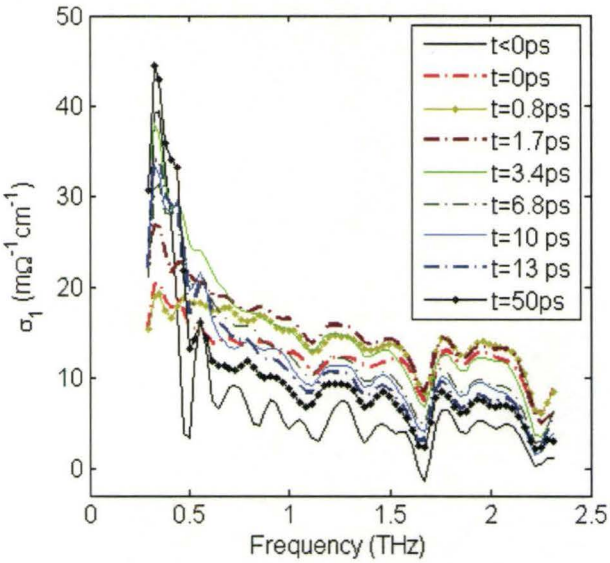

Figure 5.35 The recovery of σ_1 for an optimally doped film at T = 46 K for various times after optical excitation. The recovery of the real part of the conductivity seems to be spectrally uniform.

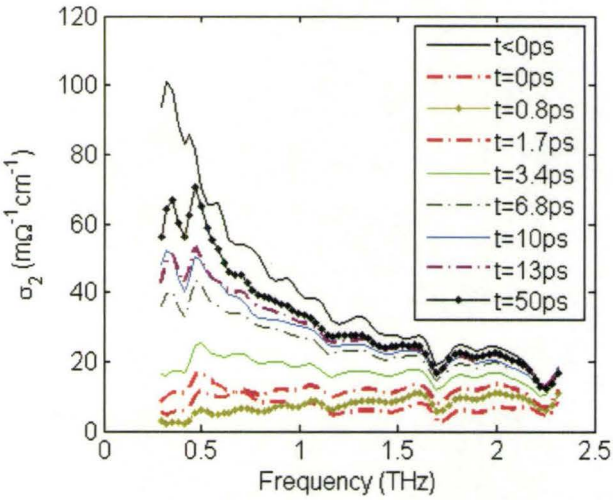

Figure 5.36 The recovery of the imaginary part of the conductivity for an optimally doped film initially at T = 46 K. Note that conductivity recovers faster at higher frequencies.

Using the steady-state transmitted THz power as a guide, an apparent temperature evolution of the film can be determined for the optically excited film as shown in Figure 5.37. By comparing the imaginary part of the conductivity of the excited film to the steady state conductivity for the corresponding temperature, the timescale of the recovery of the superconducting condensate can be determined. If the superconducting condensate has fully recovered, and the effect is purely thermal, then one would expect the optical conductivities of the optically excited film and the heated film in equilibrium to be the same.

In Figure 5.38 we see that at a delay of 5.2 ps, the condensate has not fully recovered. The imaginary conductivity is compared with the expected imaginary conductivity for a film at a temperature of 62.4 K with the normal and superconducting contributions identified. Figure 5.39 and Figure 5.40 shows the same type of analysis at 10 and 13 ps. In both cases, the magnitude of the optical conductivity is much greater than can be accounted for by the normal state indicating the recovery of the condensate is well underway. However, while the conductivity has the expected frequency dependence

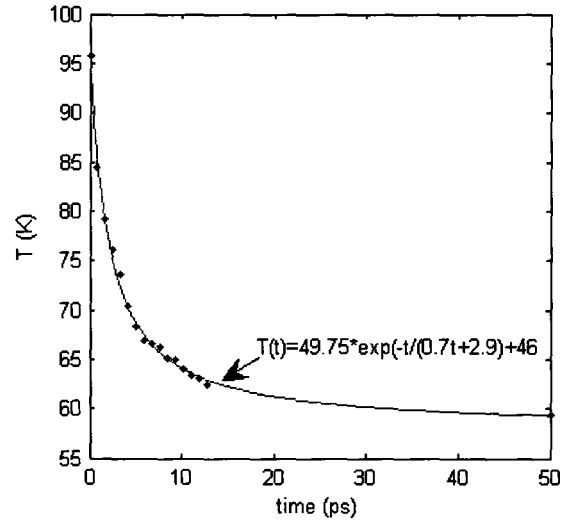

Figure 5.37 The temporal evolution of the apparent temperature of an optically excited optimally doped film. This apparent temperature is used to calculate the steady-state conductivity as a comparison to the dynamic conductivity.

at high frequencies, at lower frequencies the recovery appears to be incomplete. Averitt *et al.*[75] have reported on the artifacts that can occur at times on the order of one or two picoseconds due to the non-zero duration of the THz pulse, however by 12 ps these artifacts should not be a concern. Indeed Figure 5.41 shows that even at t = 50 ps, the effect can still be seen.

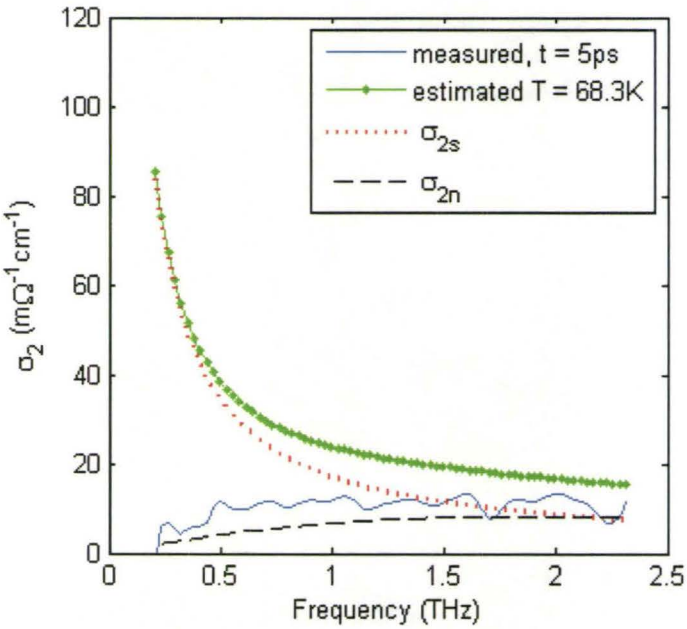

Figure 5.38 A comparison of the measured imaginary part of the optical conductivity (blue curve) for an optimally doped film 5 ps after excitation, and the modeled conductivity for a steady state film at 68.5K (green). The dotted line represents the theoretical contribution of the superconducting condensate to σ_2 and the black dashed line represents the quasiparticles contribution. It can be seen from this analysis that the condensate has not recovered by 5ps. Note that the superconducting contribution (red dots) and the normal contribution (black dashes) are added to produce the total imaginary conductivity (green).

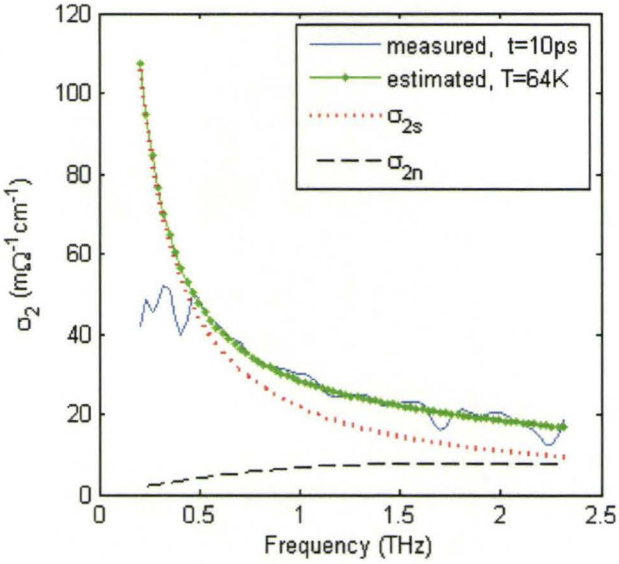

Figure 5.39 A comparison of the measured imaginary part of the optical conductivity for the same film 10 ps after excitation (blue), and the modeled conductivity for a steady state film at 64.6K (green). The dynamic conductivity matches the steady state at high frequencies, but is suppressed below 0.5 THz.

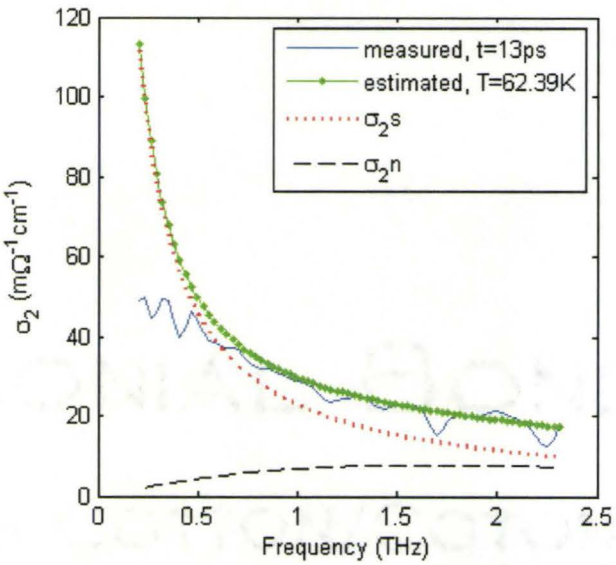

Figure 5.40 A comparison of the measured imaginary part of the optical conductivity for the optimally doped film 13 ps after excitation (blue), and the modeled conductivity for a steady state film at 62.4 K (green). The conductivity has not yet recovered at low frequencies.

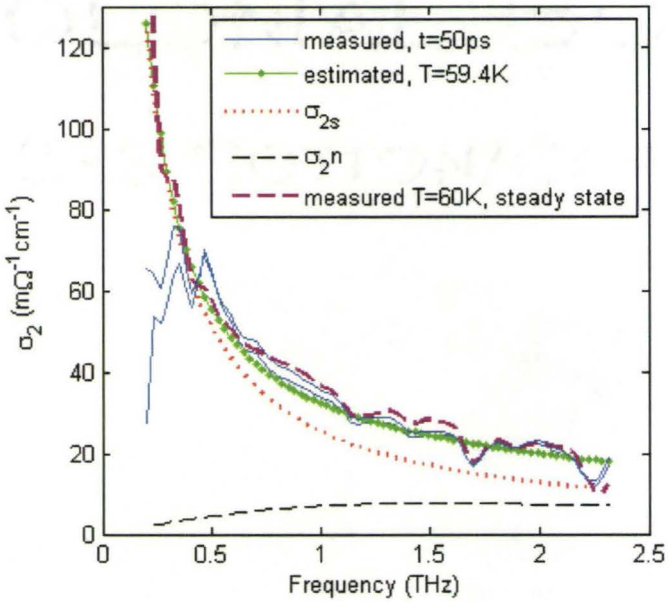

Figure 5.41 Looking at long timescales of t = 50 ps following optical excitation for an optimally doped film. Note that the imaginary part of the measured conductivity at low frequencies is still suppressed.

One issue with this analysis is that it involves comparing the results for an optically excited film to results for a film that is in equilibrium with its substrate. An ideal comparison would be with a steady state film on top of a cooler substrate. The transmission of the substrate decreases with increasing temperature. So a hot film on a cool substrate will have a greater transmission than a hot film on a hot substrate. As a result there will be a small but systematic overestimate of the apparent increase in temperature. Since the imaginary part of the optical conductivity rises rapidly at low frequencies as the temperature decreases this effect would actually lead to an underestimate of the low frequency conductivity.

Similar results are observed for underdoped samples. Figure 5.42 shows the t = 50 ps results for an underdoped film of T_c = 73 K. The optical conductivity for a film 50 ps after excitation is compared to a film at equilibrium where the transmitted THz power is the same. The effect of a partial recovery at low frequencies is very pronounced for the

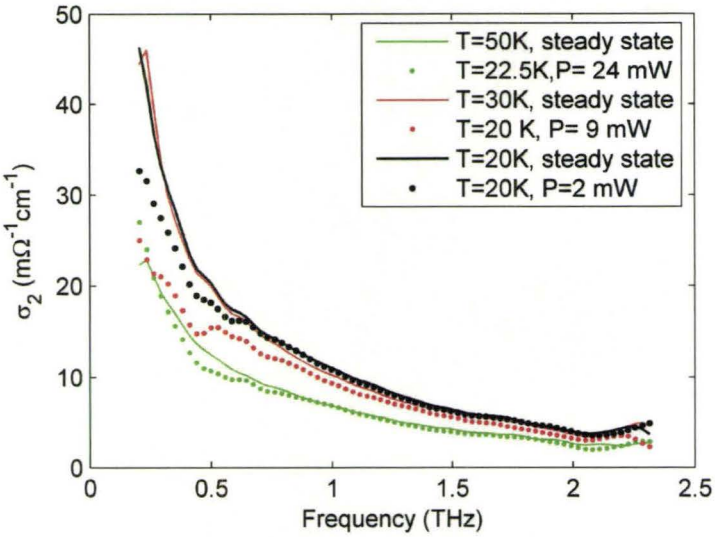

Figure 5.42 Comparing the imaginary part of the conductivity for an underdoped film (T_c = 73 K) 50 ps after optical excitation to the steady state conductivity of the same film at the corresponding apparent temperature (denoted by np). The results for three levels of optical excitation are shown. For the 2.3 mW case, the apparent temperature of the film is 23 K and is compared to the steady state film at 20 K.

optical excitation of 9.3 mW. An optical pump of 23.7 mW produces a THz transmission that is similar to a film at 50 K.[**] It is interesting to note that at the lowest frequencies the conductivity of the excited film rises above that of the steady state film. This occurs because the substrate is cooler than the excited film. This effect is less obvious for low powered optical excitations, as the difference between the film temperature and the substrate temperature is smaller.

Figure 5.43 shows that the suppression of the conductivity at long timescales occurs in each of the three films of differing doping levels. At long timescales both the imaginary and the real parts of the optical conductivity appear not to recover fully at low frequencies.

[**] The evolution of the apparent temperature trend for the underdoped film is shown in Appendix 5.

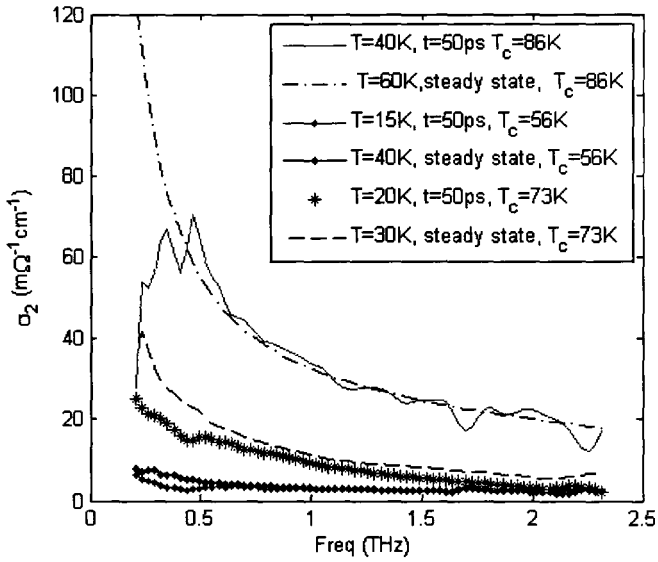

Figure 5.43 The comparison of the imaginary part of the conductivity of an optically excited film at 50 ps to a film at equilibrium for three different oxygen doping levels. The pump powers are ~28 mW for the film of T_c = 86 K, ~9 mW for the film of T_c = 73 K, and 23 mW for the film of T_c = 56 K. Note that each of the films exhibits a suppressed conductivity at low frequencies when compared to the corresponding steady-state conductivity.

5.4 Origins of the partial recovery

5.5.1 Phonon bottleneck

Previously, the long recovery of YBCO following optical excitation has been attributed to the presence of a phonon bottleneck.[32,78,80,81,86,144] As discussed in Chapter 2, there is not a consensus on the existence of a phonon bottleneck associated with the gap in cuprates.[59,61,62,88,89] There are at least two distinct issues to consider. In conventional superconductors, the bottleneck is associated with an excess of phonons with the same energy as the gap. In a d-wave superconductor there is no minimum energy to excite a normal quasiparticle out of the condensate due to the nodes. Also, it is

generally believed that phonons do not mediate quasiparticle pairing in d-wave superconductors, so it is unlikely that they would form a bottleneck preventing the condensate recovery. In any case, the experimentally observed preferential recovery at higher frequencies is not consistent with a phonon bottleneck picture. The presence of excess phonons would slow the thermal recovery of the film and the rise of the condensate, however it would not affect the $1/\omega$ dependency in the imaginary part of the conductivity arising from the condensate.

5.4.2 Spin fluctuations

If quasiparticle pairing is mediated by spin fluctuations, rather than phonons, one could imagine a spinon bottleneck. A bottleneck process, however, would be diminished due to the lack of long range magnetic order in YBCO in the absence of magnetic fields. Without long-range order, the constraints on relaxation processes due to k-space considerations would be dramatically reduced and the lifetimes associated with excess spin fluctuations might be expected to be relatively short. Again, a spinon bottleneck would slow the formation of the condensate but not change the $1/\omega$ contribution to the imaginary part of the conductivity. The contribution to the imaginary part of the conductivity from the normal component does have a downturn at low frequencies, however it is not large enough in absolute terms to explain the dramatic downturn observed in the optimally doped case, or the kink observed in the underdoped cases. Thus, a bottleneck due to phonons or spinons is an unlikely explanation for the spectral signature observed.

5.4.3 Inhomogeneity

The observed behavior is consistent, however, with a spatial inhomogeneous superconducting condensate. Indeed, a similar frequency dependence has been observed in the imaginary part of the conductivity for MgB_2 in high magnetic fields by Lee *et al.*[94] In their case, the inhomogeneity was due to vortices. As discussed in Chapter 2, evidence for inhomogeneity due to a number of different mechanisms has been previously observed in cuprates. It is expected that inhomogeneity in the condensate leads to a peak in the conductivity. Spectral weight is removed from the condensate, and for the case of granular superconductors, is generally considered to reappear at the Josephson plasma frequency.[145] However, this assumes that the normal fraction is zero. Once the presence of normal quasiparticles is included, the position of the resonance peak is expected to shift to a lower frequency. Indeed, low frequency peaks attributed to inhomogeneity have been observed by Noh *et al.* in $La_{2-x}Sr_xCuO_{4-y}$ particles.[146] The structure of the inhomogeneity must also be considered. For example, metallic spheres in an insulating medium exhibit a resonance peak near $\omega_p/\sqrt{3}$, but when the metallic inclusions are non-spherical, the resonance splits into several peaks at different frequencies.[147]

In a superconductor the binding energy of a Cooper pair increases with increasing condensate fraction. This is the fundamental reason why the superconducting transition does not typically go through a pre-paired incoherent state. It is probable that the Cooper pair formation rate is also a positive function of the condensate fraction. As a result, once nucleated, "droplets" of superconducting condensate may form and grow in size until the film reaches equilibrium, at which point the condensate would be essentially uniform. If the droplet separation is greater than the coherence length of the quasi-particle pairs, a single coherent condensate can not form and the resulting $1/\omega$ signature would not be expected. As an analogy, a non-continuous metallic film relies on tunneling between metallic grains for current to flow. Even a semi-continuous film exhibits a reduced conductivity, as the electrons must percolate through channels of metallic

material. In the superconducting case, the inhomogeneity may manifest in the phase, where the droplets or grains of superconductivity are separated not by insulating material, but by the normal metallic phase. Even if a weak percolative path for superconducting current is established, the size of the delta function in the conductivity will be diminished and as a result spectral weight will be shifted to higher frequencies. A detailed description of the expected optical conductivity from such a non-uniform superconductor-normal mixture is complicated by the fact that the length scale and structure of the inhomogeneity will be important. This is particularly true if one is near the percolation limit as would appear to be the case for our results.

5.4.4 Drude-Smith model

One would expect similar results in simpler metal-insulator mixtures. Gold nano-particles have been shown to be less conductive than continuous gold films, and exhibit a similar suppression at low frequencies.[16] Of course, inhomogeneity of the condensate would not be a case of a metal interspersed with an insulator, but rather superconducting regions interspersed with poor metallic regions. In one recent result, Walther *et al.* explored the conductivity of a semi-continuous metallic film deposited on an insulator as a function of film continuity through the percolation transition.[15] They observed a significant suppression at low frequencies and applied a number of models in an attempt to capture this behavior. The most successful model found was the Drude-Smith model.[14] As outlined in section 1.1.3, the Drude-Smith model attempts to describe the conductivity for a system where the quasi-particle scattering is non-isotropic. The Drude-Smith conductivity is given by:

$$\sigma = \frac{ne^2\tau}{m(1-i\omega\tau)}\left[1+\frac{c}{(1-i\omega\tau)}\right] \qquad \textbf{5.10}$$

where c is 0 for isotropic scattering, as is assumed in the Drude model and c = -1 for the case of complete backscattering.

Motivated by this result, we can consider an extension of this approach. In this approach it is necessary to consider not only the backscattering of electrons in the metallic region, but also the backscattering in the condensate. As the Drude-Smith model is consistent with a Kramers-Kronig analysis, it can be a useful tool in analyzing the conductivity, even if the fit is merely parametric. Consider a near perfect Drude metal where the scattering time is large. If we add the expansion term introduced by Smith but let the expansion terms depend upon a shorter scattering time consistent with a poor metal we have a rough physical model for the behaviour of the dynamic conductivity of our YBCO thin film. This "two τ" Drude-Smith model can be used to capture the downturn in the imaginary part of the conductivity observed in the optimally doped sample, as seen in Figure 5.44. As this model is consistent with Kramers-Kronig, it may be used to generate a reasonable approximation for the real part of the conductivity, as seen in Figure 5.45. The kink observed in the imaginary part of the conductivity in the

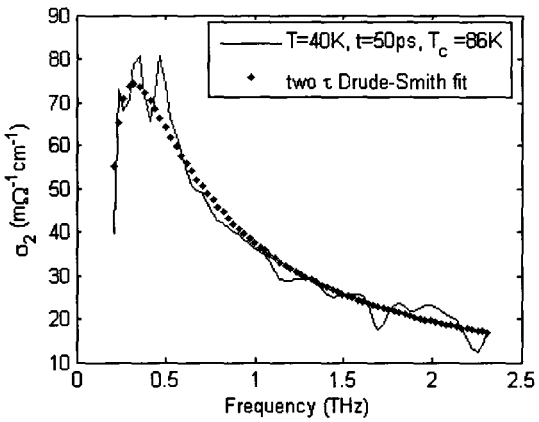

Figure 5.44 Fit of the "two τ" Drude-Smith model to the imaginary part of the conductivity for an optimally doped film at T = 46 K, 50 ps following optical excitation.

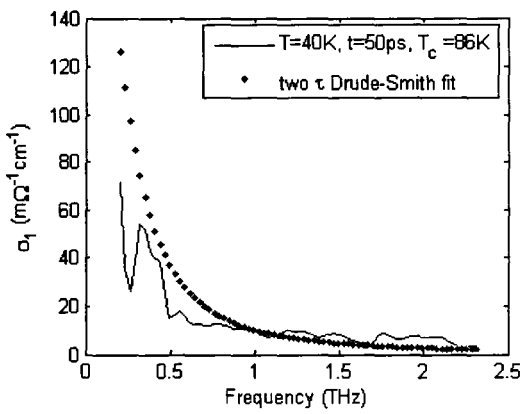

Figure 5.45 A comparison of the real part of the conductivity for an optimally doped film at T = 46 K, 50 ps following optical excitation and the conductivity calculated from a fit of the "two τ" Drude-Smith model to the imaginary part of the conductivity.

underdoped samples is not readily modeled using this approach.

Based on the success of the Drude-Smith model, a modification to the two-fluid model is proposed:

$$\sigma = \frac{n_0 e^2 \tau}{m}\left(\frac{1-f_s}{1-i\omega\tau} * \left(1+\frac{c_n}{1-i\omega\tau}\right) + i\frac{f_s}{\omega\tau} * \left(1+\frac{c_s}{\omega\tau}\right)\right) \qquad 5.11$$

Here, the "backscattering" constant is allowed to vary for the metallic (c_n) and superconducting (c_s) cases. Fitting the new two-fluid model to the real and imaginary part of the conductivity, while allowing the temperature, c_n and c_s to vary, allows for reasonable agreement as is shown in Figure 5.46 and Figure 5.47. There is no direct measurement of the electronic temperature and, as a result, we do not have independent knowledge of the appropriate value for f_s and τ. Thus, the temperature, c_n and c_s are all treated as fit parameters. Unfortunately the nature of the fit does not lead to tight constraints on the parameters, i.e. the backscattered coefficients can be varied substantially if the temperature is adjusted. Furthermore, the modified two-fluid model fit can only be considered a phenomenological fit to illustrate the possibility of adapting an approach similar to Drude-Smith to superconductivity.

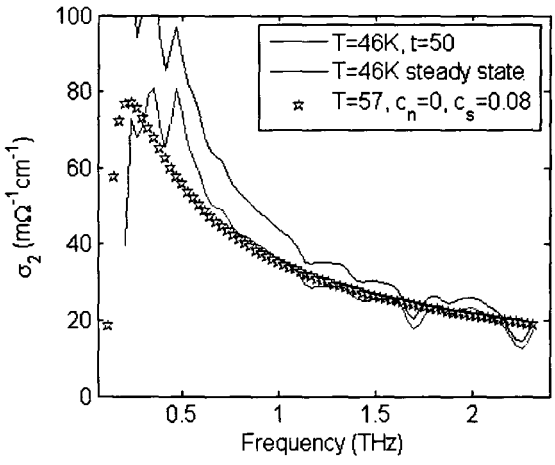

Figure 5.46 The modified two-fluid model fit to the imaginary part of the conductivity for an optimally doped YBCO film at 46 K, 50 ps after optical excitation.

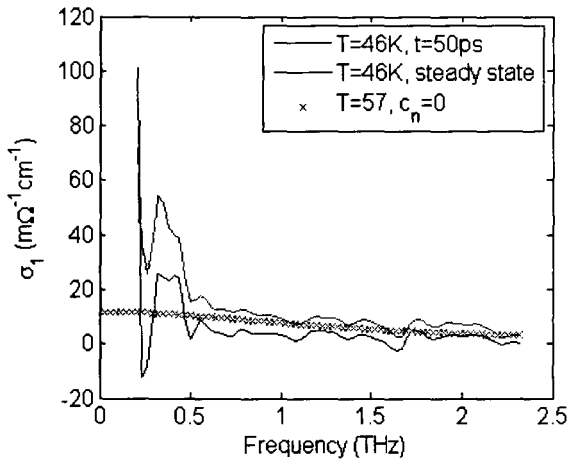

Figure 5.47 The modified two-fluid model fit to the real part of the optical conductivity of an optimally doped film 50 ps after excitation.

5.4.5 Effective Medium Approximations

An alternative approach to modeling inhomogeneities is to use an effective medium approximation. Effective medium theories predict the electrical properties of a composite material from the properties of the individual components. Generally, the models describe a picture of one material embedded in a second material. There is a significant body of work devoted to modeling the characteristics of inhomogeneous materials.[148,149,150] The general case includes the geometric information of the embedded material in a spectral function that can be generated numerically. A simpler approach is to use an effective medium approximation based on an assumed geometry. These types of effective medium approximations have had considerable success in describing the properties of metallic films. An effective medium approach has also been used to describe granular superconductivity.[151,152] Effective medium approximations are suitable for THz measurements of inhomogeneous materials, as the inclusions are smaller than the probe wavelength, while generally still being large enough to be described by a separate conductivity.[158] Effective medium approximations, such as Brugeman's model and the Maxwell-Garnet model obey Kramers-Kronig relations.[153]

Bruggeman's model[154,155] provides a reasonable starting point for the conductivity of an inhomogeneous film. The effective conductivity of a film containing spherical inclusions is given to be:

$$\sum_{i}^{m} f_i \frac{\sigma_i - \sigma_{eff}}{\sigma_i + (n-1)\sigma_{eff}} = 0 \qquad 5.12$$

where m is the number of different components, f_i is the fraction of component i, n is the number of dimensions, σ_i is the conductivity of component i, and σ_{eff} is the effective conductivity of the composite sample. In our case we have two components: the normal component and the condensate, and assume a two-dimensional system. Barabash *et al.*[156] simplifies the model to:

$$\frac{\sigma_A - \sigma_{eff}}{\sigma_A + \sigma_{eff}} + \frac{\sigma_B - \sigma_{eff}}{\sigma_B + \sigma_{eff}} = 0 \qquad \textbf{5.13}$$

Thus, the effective conductivity becomes: $\sigma_{eff} = \sqrt{\sigma_A \sigma_B}$. This simple model is not sufficient to describe the behaviour of the conductivity seen in Figure 5.43. Clearly a more complex effective medium approximation is required to model the effect. Indeed, the effective medium theory becomes more complicated when superconducting electrodynamics are taken into consideration.[157]

The Maxwell-Garnet model (also known as the Clausius-Mossotti model) is another commonly used effective medium approximation. It has been used successfully to model VO_2 metallic thin films, where the Bruggeman model was insufficient near the percolation threshold.[158] The Maxwell-Garnett model is considered to be more valid in cases where the grains (or inclusions) are well separated: i.e. where the volume fraction of the high conductivity regions is small.[158] For the case of metallic inclusions in an insulating medium, the effective dielectric function is given by:

$$\varepsilon_{eff} = \varepsilon_i \frac{\varepsilon_m(1+2f) - \varepsilon_i(2f-2)}{\varepsilon_i(2+f) + \varepsilon_m(1-f)} \qquad \textbf{5.14}$$

where ε_i is the dielectric function of the insulator, ε_m is the dielectric function of the metal, and f is the volume fraction of the metallic regions. This effective medium approximation must be modified when studying superconducting inclusions in metallic regions. Lee *et al.*[94] modeled the conductivity of MgB_2 thin films in high magnetic fields using the Maxwell-Garnet approximation modified to assume normal metallic disks embedded in superconducting materials. The effect of the vortices was successfully described by their model. Although it is not expected that the superconducting droplets in our case would be as evenly distributed as magnetic vortices, their approach offers a reasonable first step in applying the Maxwell-Garnet approximation to phase inhomogeneities in YBCO thin films. The effective dielectric constant is given by:

$$\varepsilon_{eff} = \varepsilon_n \frac{\varepsilon_n(1-f)+\varepsilon_s(1+f)}{\varepsilon_n(1+f)+\varepsilon_s(1-f)} \quad \textbf{5.15}$$

where ε_n is the dielectric function of the normal metallic regions, ε_s is the dielectric function of the condensate, and f is the volume fraction of the superconducting regions. Recalling the relationship between the optical conductivity and the dielectric function:

$$\varepsilon = \varepsilon_r - i\frac{\sigma}{\varepsilon_0 \omega} \quad \textbf{5.16}$$

where ε_r is taken to be 1, and ε_0 is the permittivity of free space, it is possible to calculate an effective conductivity from equation 5.16. The normal and superconducting contributions to the two-fluid model are used as the conductivities of the normal regions and the superconducting disks. Thus, it is possible to model the effective conductivity of an inhomogeneous film for various temperatures. Figure 5.48 and Figure 5.49 show the effective conductivity for different volume fractions at T = 45 K. It can be seen that although the there is a peak present in the imaginary part of the conductivity; it is located at a lower frequency than the peak in our measured conductivity seen in Figure 5.41.

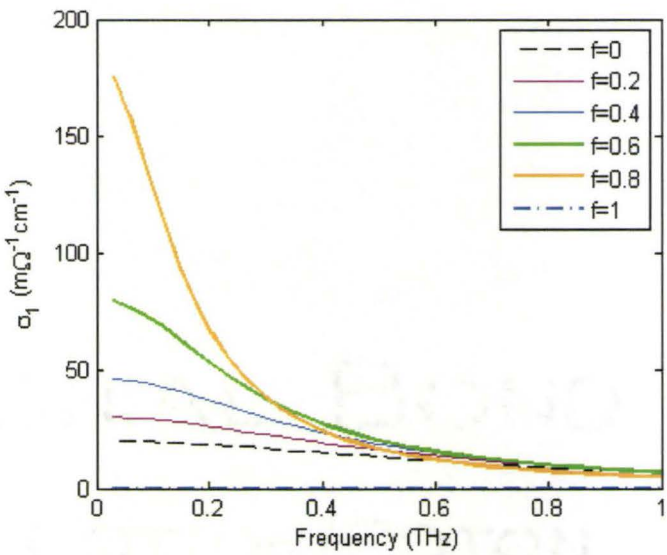

Figure 5.48 Evolution of the Maxwell-Garnet effective medium approximation of the real part of the conductivity for differing volume fractions of the superconducting regions. f = 0 represents a case where the film is uniformly normal, and f = 1 represents the case where the film is uniformly superconducting.

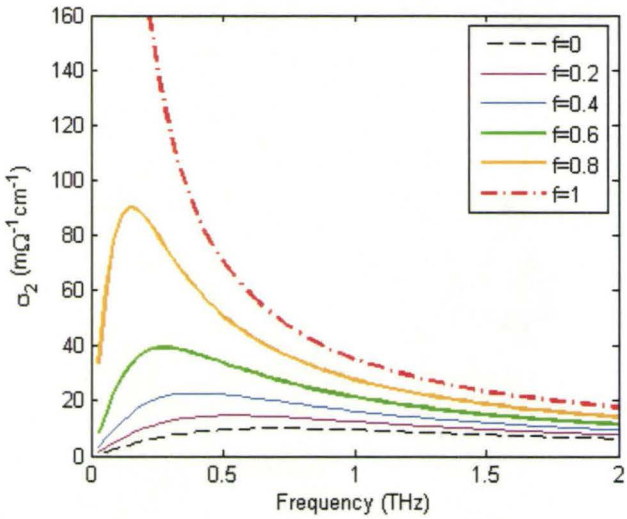

Figure 5.49 Evolution of the Maxwell-Garnet effective medium approximation of the imaginary part of the conductivity for differing volume fractions of the superconducting regions. The conductivity of the superconducting disks is taken from the condensate's contribution to the two-fluid conductivity at 46 K, and the conductivity of the normal regions is taken from the normal contribution. Thus, f=0 represents a case where the film is uniformly normal, and f =1 represents the case where the film is uniformly superconducting.

5.5 Normal state dynamics in underdoped samples

As discussed in Chapter 2, there is a possible existence of pre-formed pairs associated with the pseudogap above T_c in cuprates. While the THz probe only contains energies lower than the pseudogap, the optical pump THz probe experiment may be able to indirectly detect the existence of preformed pairs. If such pairs exist, the optical excitation could lead to pair breaking which might modify the optical response in the THz regime. Unlike the case below T_c, this would not result in a dramatic change in the optical conductivity, but rather a broad suppression. As can be seen in Figure 5.50, the normal state dynamics of the optimally doped film recovers faster than the underdoped films. The slower recovery of the transmitted THz power in the underdoped films may be indicative of a perturbation of the pseudogap following optical excitation. However, when the apparent change in temperature is examined (Figure 5.51), the differences between optimally doped and underdoped samples do not seem very pronounced.

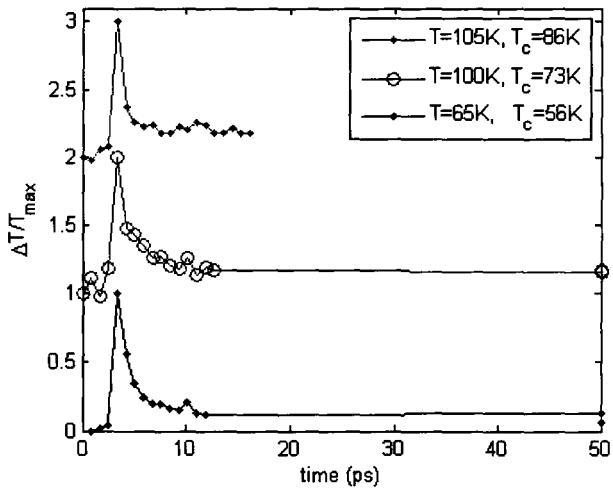

Figure 5.50 The change in the total transmitted THz electric field above T_c normalized by the maximum transmission for three samples of different oxygen doping: T_c = 86 K (red), T_c = 73 K (blue), T_c = 56 K (black). The transmission of the optimally doped film appears to recover faster than the underdoped films. The optical pump power for the optimally doped case was 28 mW, and ~23 mW for the underdoped films. The graphs are vertically offset for clarity and t = 0 is chosen arbitrarily.

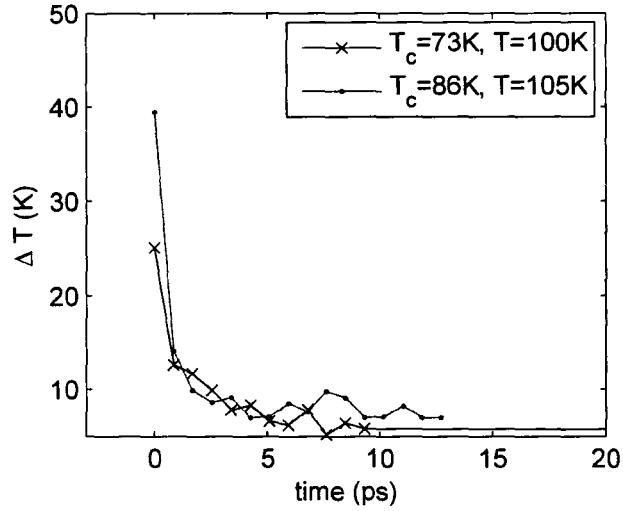

Figure 5.51 The evolution of the apparent change in temperature due to optical excitation of an optimally doped and underdoped sample. The optical pump power for the optimally doped sample was 28 mW, and the power for the underdoped sample was 24 mW. Note that there is no significant difference between the responses of the two films.

Spectroscopically, at long timescales, the conductivity of an optically excited film looks similar to a thermally excited underdoped film. As expected, there is no evidence of inhomogeneity above T_c. Figure 5.52 illustrates that the optical conductivity of an underdoped film (T_c = 56 K) 50 ps following optical excitation seems to have almost fully recovered thermal equilibrium. The lack of any defined spectroscopic signature in the optically excited conductivity in the normal state indicates no evidence of perturbation of incoherent quasiparticle pairs. It is expected that the effect on the conductivity in our frequency range would be a broad suppression of the conductivity, however this was not observed. The recovery of the films above T_c was faster than below T_c. It may be possible that the temporal resolution of the THz probe was not fast enough to capture the relevant processes in the film above T_c.

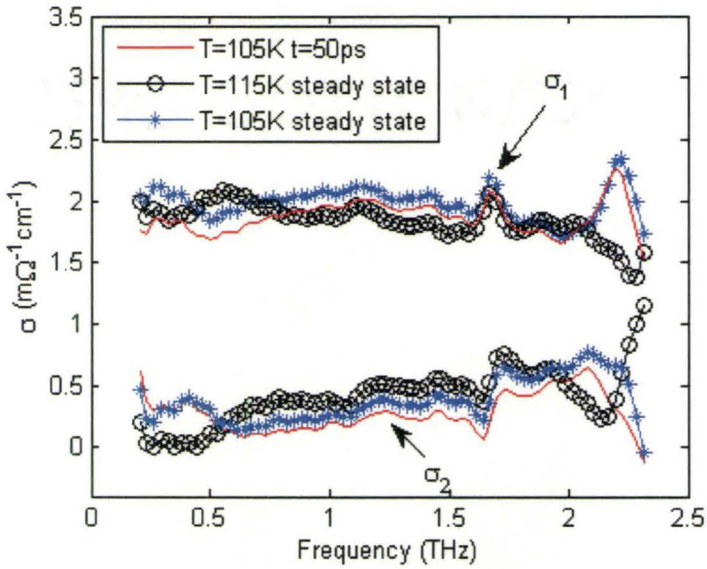

Figure 5.52 The optical excitation of an underdoped film (T_c = 56 K) 50 ps after optical excitation (red line) at 105 K compared to the steady state conductivity at 105 K (blue star) and 115 K (black circle). The top curves show the real part of the conductivity and the bottom curves show the imaginary part.

5.6 Summary

The steady-state properties of an optimally doped film have been derived from the THz conductivity, and are in agreement with previously reported measurements of the optical properties of optimally doped YBCO. We have measured the change in the transmission of optimally doped and underdoped films for different levels of optical excitation, and have observed a faster recovery than is generally reported for optical pump optical probe experiments. Additionally, we have not observed the dramatic increase in the recovery time associated a decrease in the optical energy density when using optical pump optical probe techniques. We have consistently observed a slow recovery at long timescales for both optimally and underdoped YBCO films below T_c.

Although a thermodynamic argument supports the hypothesis that the slow recovery of the transmission is purely thermal, the spectroscopic evidence contradicts this conclusion. A change in the $1/\omega$ dependency of the imaginary part of the conductivity, taking the form of a low frequency suppression, as was observed in the optimally doped film at 40 K, is not indicative of either a phonon bottleneck or excess spin fluctuations. The simplest explanation for a change in the spectral content of the film is the presence of spatial inhomogeneity in the superconducting fraction. As discussed in Chapter 2, there has already been considerable evidence for various inhomogeneities in cuprates. In this thesis we have presented spectral evidence of instable spatial inhomogeneities in the condensate, indicating a more complex mechanism for the recovery of the condensate following optical quenching.

Chapter 6 Conclusions and Future work

6.1 Conclusions

The signature property of high temperature superconductors is, of course, the relatively high value of the superconducting transition temperature. However, associated with the large T_c is a small value of the coherence length. The in-plane coherence length for YBCO depends on the doping, but is on the scale of nanometers, a lengthscale dramatically less than that observed for conventional superconductors such as lead. In conventional superconductors, the long coherence length suppresses any spatial inhomogeneity in the superconducting properties. Indeed, inhomogeneity in HTSC has recently gained great interest both in terms of understanding recent experimental results and new theoretical approaches. Inhomogeneities in the electronic density of states, the charge distribution and the order parameter (gap) were not accounted for in historical models of superconductivity. Now, rather than considering these inhomogeneities an experimental nuisance, there is a growing belief that their study may provide further insight into the interactions present in type II superconductors.[146,159] Indeed, it has been postulated that the pairing mechanism in high temperature superconductors is intrinsically related to mesoscale* electronic structure.[160] To date, there is no consensus on the universality of intrinsic inhomogeneities in high temperature superconductors. It is, therefore, necessary that experimentalists produce sufficient evidence for the existence (or lack thereof) of intrinsic inhomogeneity.

In the thesis presented, a picture of the inhomogeneous recovery of the condensate in YBCO thin films has been presented. The observed suppression of the optical conductivity at low frequencies following optical excitation appears to be analogous to the results observed for the effect of vortices on the conductivity.[94] Although we cannot directly observe the inhomogeneous regions, we can infer, based on

* ie: inhomogeneities on lengthscales that are bigger than the coherence length, but of the same order of magnitude.

the wavelengths used, that the lengthscales involved must be smaller than 100 μm. Extrinsic inhomogeneities have been often observed in superconducting films, due to point defects, doping inhomogeneities etc. This type of inhomogeneity has been considered the mark of poor film quality and the experimentalist's bane. For the case presented in this thesis, the inhomogeneity is not the static inhomogeneity observed due to film defects, but is rather a dynamic inhomogeneity observed due to the nucleation of the condensate following its optical destruction. The superconducting droplets would most likely condense in the most perfect regions of the film, as defects tend to reduce the condensate's energy.

Other explanations for the recovery of the optical conductivity at long timescales are an anharmonic phonon bottleneck, or a spin wave bottleneck. While it is true that excess phonons created by the relaxation of energetic quasiparticles could lead to a delay in the thermal recovery of the film, this does not account for the frequency dependence of the imaginary part of the recovering conductivity since, while excess spin waves may delay the recovery of the condensate, they would not change the condensate's spectral contribution to the conductivity. Previous studies of the dynamics of cuprate superconductors have assumed a spatially uniform recovery of the film. Based on the evidence presented here, techniques that are sensitive to these inhomogeneities may merit a more complex analysis to include this effect. The emergence of transient spatial inhomogeneities in the superconducting fraction, following the optical quenching of the condensate, points to the existence of new intriguing processes involved in the formation of the condensate in thin film cuprates. Further study of these temporally instable inhomogeneities is warranted.

6.2 Future Work

6.2.1 Experiments

The results presented here can only give indirect evidence of phase inhomogeneity. A more direct confirmation of the "droplet" formation of the condensate would, therefore, be valuable. Although experimentally challenging, THz imaging techniques may be able to "see" at least the largest of the structures in the recovering condensate. THz imaging of the spatial resolution of the optical conductivity has already been carried out by Brucherseifer *et al.*[102] for films in equilibrium. They observed inhomogeneity in the conductivity of the film as an indicator of film quality. If, through using a similar technique, the inhomogeneity of the optical conductivity was enhanced by optical excitation, then this would strengthen the case for a non-uniform recovery of the condensate. The temporal resolution would be problematic, however, and as a result the experiment would likely be limited to timescales in excess of 10 ps.

An obvious suggestion for the next experimental step in this investigation is to look for similar behaviour in other cuprates and high temperature superconductors. A survey of superconducting films using optical pump THz probe spectroscopy could be valuable in determining the universality, and consequently the importance, of this effect.

The short superconducting coherence length of YBCO is what makes our observation of an inhomogeneous condensate plausible. It would therefore be useful to conduct a similar experiment upon a superconducting film with a longer coherence length, such as niobium diselenide. It is expected that the suppression of the conductivity at low frequencies would be absent in this experiment.

Any other technique used to investigate dynamic phase inhomogeneities would need to be non-destructive and of low enough energy not to perturb the system being imaged. If the formation of phase droplets was of a chaotic nature, then a statistical analysis of an STM measurement for a film following optical excitation could show this. This would have very significant experimental complications, as the STM may perturb

the system too much, and a strong repetitive optical pulse would interfere with the STM. It is known that the presence of inhomogeneities leads to peaks in the conductivity. A search at higher frequencies for peaks that appear following optical excitation would give further evidence of phase inhomogeneity.

6.2.2 Theory

In this thesis, several models designed to approximate an inhomogeneous medium have been investigated. The most successful model in fitting our data was the modified two-fluid model based on the Drude-Smith model. The weakness of this model - while capable of providing a phenomenological fit to the recovering conductivity, is that it is not theoretically rigorous. The work presented here represents a preliminary treatment of the modified semi-continuous two-fluid model. Further theoretical development to the Drude-Smith model and its extension to the two-fluid model is recommended. The original Drude-Smith model has been successfully used to describe inhomogeneous metallic and semi-conducting films,[15,160,161] however the theoretical basis for treating the fit parameter c as a backscattering constant is not rigorous. From an experimental perspective, a relationship between c and the percolation limit in semi-continuous metallic films has been investigated by Walther *et al.*[15] This type of analysis could also be beneficial when modeling the recovery of a superconducting film.

A more rigorous analysis of the modified two-fluid model would require an accurate estimate of the thermal evolution of the film. It has been shown from the spectroscopic analysis presented here that while the optical pulse does indeed elevate the temperature of the film, the change in transmission does not provide an accurate guide to the temperature of the film at early timescales. Indeed, even at 50 ps following optical excitation, the response of the film is not purely thermal. Thus, if the scattering time is included, the fit to the conductivity will yield more than one solution.

The modified Drude-smith model is only one possible model. Several modifications to the Drude model exist that could be adapted to the two-fluid model,[14]

and the effective medium theory has been successfully used to interpret inhomogeneous materials.[153,162,163]

The effective medium approximation is the most popular approach to inhomogeneous materials. The Bruggeman model and the Maxwell-Garnet approximation are the simplest, and consequently widely used. It is not strictly correct, however, to use these simplistic approximations, as the effective conductivity depends significantly on the configuration of the microstructure.[164] The effective medium theories stem from the Bergman theory which defines an effective dielectric constant as:

$$\varepsilon_{eff} = \varepsilon_1 \left(1 - f \int_0^1 \frac{g(y)}{\left(\frac{\varepsilon_1(\omega)}{\varepsilon_1(\omega) - \varepsilon_2(\omega)} - y \right)} dy \right) \qquad \textbf{6.1}$$

where f is the volume fraction, and g is the spectral density, which depends on the geometry of the inclusions. Thus, the rigorous solution is highly dependent upon knowing the spectral density, a quantity that is not trivial to derive, especially when the geometry of the inhomogeneity is unknown. Thus, most authors use the simpler forms described previously in Chapter 5. Finally, any model used to describe inhomogeneities in superconductors must be modified to reflect the electrodynamics of the condensate. A theoretical model that includes a "droplet" approach to condensate formation would be very useful for modeling the data presented in this thesis. Further development and testing of theories that include phase inhomogeneities is warranted.

Appendix 1 Terahertz Conversion Table

ν (THz)	ν (GHz)	λ (μm)	λ^{-1} (cm^{-1})	E (zJ)	E (meV)	E (y-cal)	T (K)
0.3	300	1000	10.0	0.12	1.24	47	2.898
0.5	500	600	16.7	0.33	2.07	79	4.83
1.0	1000	300	33.3	0.66	4.14	158	9.66
1.5	1500	200	50.0	0.99	6.21	238	14.49
2.0	2000	150	66.7	1.32	8.28	317	19.32
2.5	2500	120	83.3	1.66	10.34	396	24.15
3.0	3000	100	100	1.99	12.4	475	28.98
31	31000	9.66	1035	20.54	128	4899	300

Appendix 2 Path length instabilities

Substantial beam path instability can contribute alignment issues in THz generation, detection and in sample alignment. These issues are discussed in Chapter 3 of this thesis. Possible sources of instability are poor alignment of the laser cavity, thermal fluctuations, and external vibrations. With proper laser maintenance, the cavity alignment can be kept stable. Spectral analysis of the seed pulse can determine that the bandwidth and output power is optimum, which is a good indicator of proper laser alignment. Alignment of the seed in the amplifier can be checked on pinholes. Thermal fluctuations can come from many sources and are much harder to control. The effect of localized fluctuations caused by heat sources such as the laser power supply can be minimized by building shielding to direct hot air away from the optical tables. Otherwise, the table will gradually heat up, causing the mirrors to shift. There was a 50% improvement in the measured THz power drift following the shielding of nearby heat sources. Drift of the ambient room temperature can be problematic. Without proper climate control, the solution was to closely monitor laser stability along with room temperature at various locations and abort experiments on days when room temperature stability was compromising quality of data. Short experiments tend not to be adversely effected by laser drift. Localized heating or gradual room temperature drift occurs over the course of hours.

A 2.1 Beam profile monitoring

By monitoring the beam profile throughout an experiment, small changes in the beam direction can be observed and corrected at the output of the laser. Additionally, by repeating a control measurement at regular intervals during an experiment any phase shifts due to beam wander can be detected. Figure A2.1 shows the beam profile taken at the beginning and end of an experiment. It is possible to correct for phase shifts due to beam wander at the data analysis stage, as long as there is no clipping of the beam.

Consider the effect of moving the THz spot on the detector crystal; the spectroscopic effect of moving the spot by 100 microns on the detector crystal is significantly smaller than the associated path length change*. A misalignment originating further upstream would require a greater path length change to produce the same deviation on the detector crystal. Thus it can be concluded that by monitoring the phase change of the spectrum in the time domain and the beam profile it is possible to maintain very good quality control.

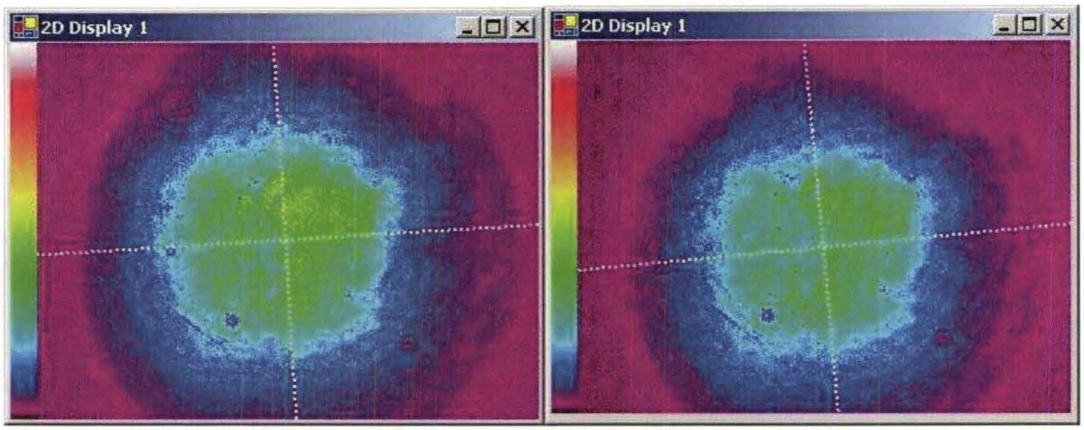

Figure A2.1 Beam profile taken behind a mirror on the THz generation beam line using Ophir optics's Beamstar data acquisition program. On the left shows the beam at the beginning of the experiment, on the right shows the beam at the end of the day. Small intensity variations are expected over time.

Appendix 2.2 Humidity control

The presence of the water vapour also subtly changes the index of refraction of the air in the THz regime, and so the pulse is phase shifted. Thus, it is crucial that the humidity does not change during a scan, or between the measurements and the reference scan, as discussed in Chapter 3. It is non-trivial to simply correct for the phase shift introduced by water vapour at the analysis stage as the phase shift is not spectrally

* The effect of beam position on the detector crystal is discussed in Appendix 4

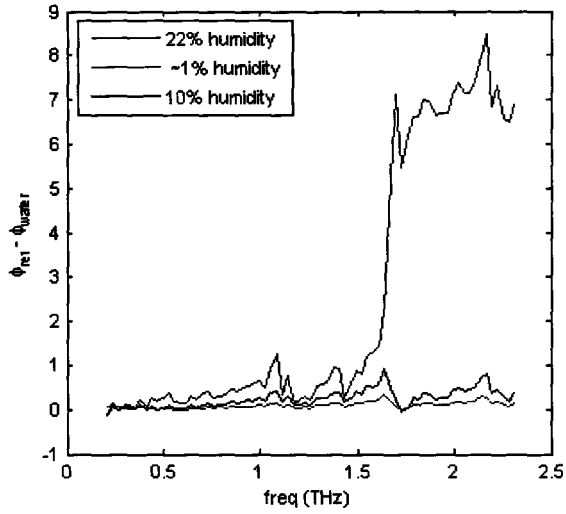

Figure A.2.2 The change in phase of the THz electric field between a reference scan of dry air and humid air.

uniform, as shown in Figure A.2.2. The phase shift is negligible at a humidity of 1%, and even at 10% the shift is small.

The reference scan is of a nitrogen purge for 1 hour at a flow of 20 S.C.F.M[†] after the humidity reading reached 0% on the hygrometer. The humidity level of 10% is reached after a purge with a flow of 10 for 10 minutes. Figure A2.3 shows the relative humidity as a function of purge time. The error associated with the hygrometer is ±5% below 15% relative humidity. Errors associated with phase shift due to changes in humidity are avoided by keeping the purge constant throughout each experiment. A purge of 30 minutes or more is sustained before each experiment to ensure that the humidity is reduced to <3%. Thus any phase shift will be negligible. Absorption peaks will persist, due to residual humidity in the air but can easily be filtered out.

[†] Standard cubic feet per minute

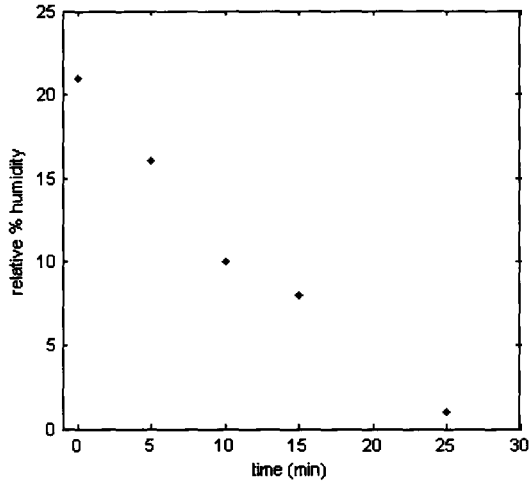

Figure A2.3 Relative humidity inside the purge box for a N_2 flow of 10 S.C.F.M

A.2.3 Effect of phase difference introduced by film

The calculation of the conductivity using the thin film approximation relies on t*, the ratio of the electric field through the bare substrate to the electric field through the film-substrate sample. Thus, the phase shift associated with the index of refraction of the film (θ) is integral to the resulting conductivity. t^* can be re-written as $|t^*|(\cos\theta + i\sin\theta)$. Thus, the real part of the conductivity depends upon the cosine of the phase shift introduced by the film, and the imaginary part of the conductivity depends on the sine of the phase shift. As can be seen in Figure A.2.4, the phase shift associated with the film well below T_c gives a phase close to 90° therefore the imaginary part of the conductivity is less susceptible to small errors in the phase, as the sine does not change rapidly near 90° while the cosine does. Above T_c, the phase shift is more like 0°, and so the imaginary part of the conductivity is less accurate above T_c.

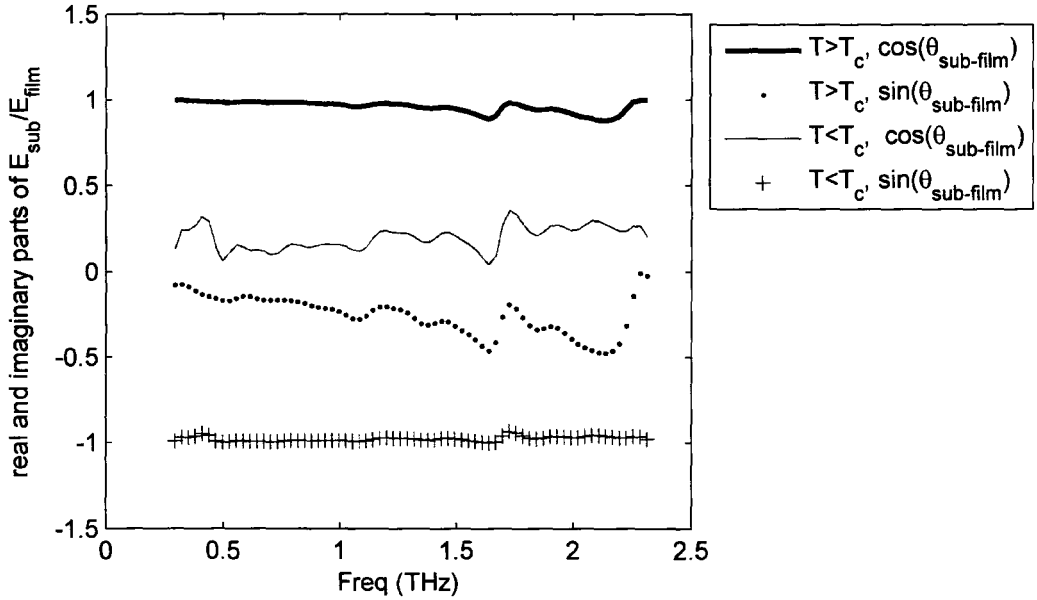

Figure A.2.4 The cosine and sine of the phase introduced by an optimally doped YBCO film above and below T_c.

Appendix 3. Laser Stability

The stability of the output power of the laser is crucial to the success of pump-probe THz spectroscopy. Both the THz generation and detection are accomplished with amplified IR pulses. Thus, if the laser power drops, both the THz power and the ability to detect it will be compromised. The change in laser power leads to a relatively uniform change in the THz spectrum. Figure A3.1 shows the ratio of the detected THz electric field for a laser power of 456mW to the field detected for a laser power at various other power levels. As the power decreases significantly, the spectral change becomes less uniform. The laser power used for the experiments reported in this thesis is well above this region.

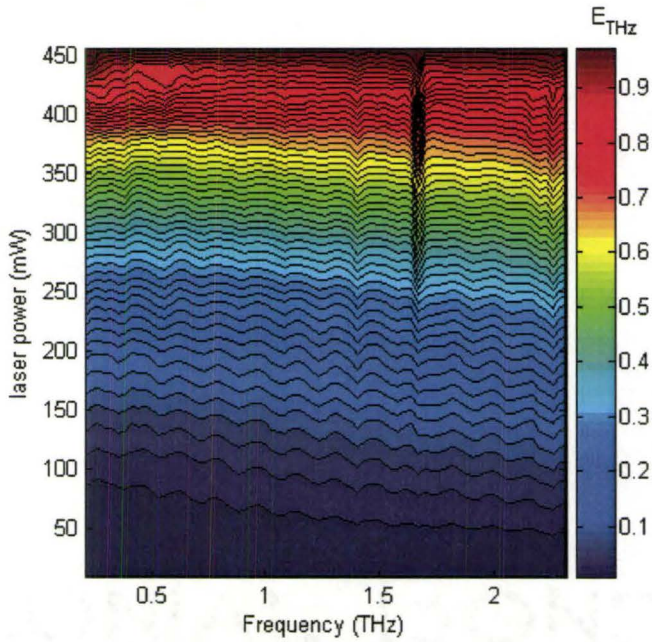

Figure A3.1 The THz electric field normalized at various laser powers to the measured electric field at 456mW is shown in colour to illustrate the spectral evolution of the THz electric field for various output powers of the laser. The colour denotes the electric field strength, where blue represents a small electric field and red represents a large electric field. It can be seen that the generated THz spectrum decreases fairly uniformly for higher laser powers. The dip at 1.6 THz is a water absorption line.

A3.1 Power dependence on the chiller temperature

For optimum laser stability, the temperature of the gain medium must be kept constant. Figure A3.2 shows the correlation between the temperature of the chilled water supplied to the gain medium of the laser amplifier, and the output power of the laser system. The chiller also provides cooling to the gain medium in the laser oscillator. The thermal cycling of the water temperature generally occurs at a period of ~5min. As this timescale corresponds with the time it takes to acquire a THz scan, this effect is particularly insidious. Thermal cycling can be corrected by adjusting a shunt valve on the chiller unit. The temperature cycling shown in Figure A3.2 does not occur during optimal laser operation. Figure A3.4 shows the laser output during normal operation. With careful monitoring throughout the experiment, the temperature cycling can be spotted and corrected to less than 2%.

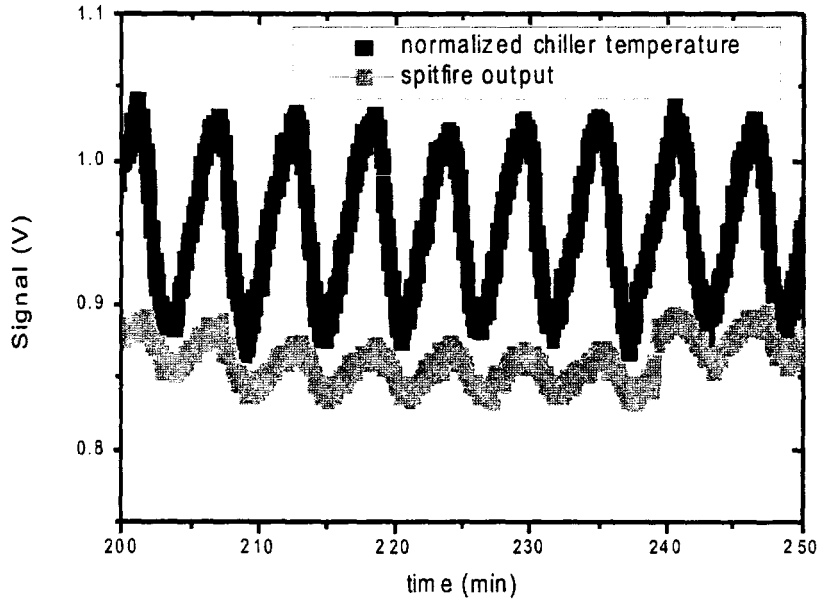

Figure A3.2 The correlation between the chiller temperature for the gain medium of the amplifier (top curve) and the amplifier output power can be seen.

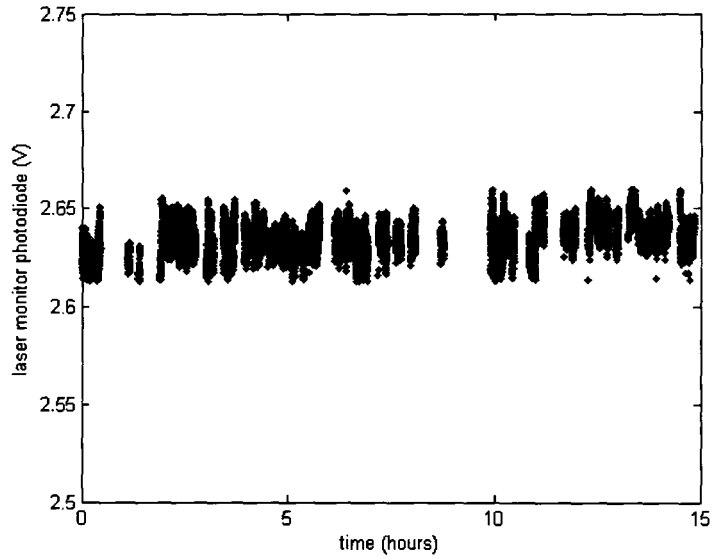

Figure A3.4 Laser power monitored throughout an experiment.

Appendix 4 THz Alignment Details

A4.1 Focal position of detector crystal

The THz emitted from the generation crystal is focussed onto the sample and detection crystal via a set of parabolic mirrors. The location of the THz focal spot can be controlled by minutely adjusting the position of the generation crystal via an x-y-z stage as shown in Figure 4.8. For maximum signal detection, the detector crystal must be located at the focus of the THz spot, as illustrated in Figure A4.1. Figure A4.2 illustrates that the optimal position is different for different frequencies. This indicates that the THz focal spot is somewhat frequency dependent. The position of the detector crystal with respect to the focus of the THz spot must not change between sample and substrate measurements. The role of the focal position of the detector only becomes important to results if there is a change between measurements.

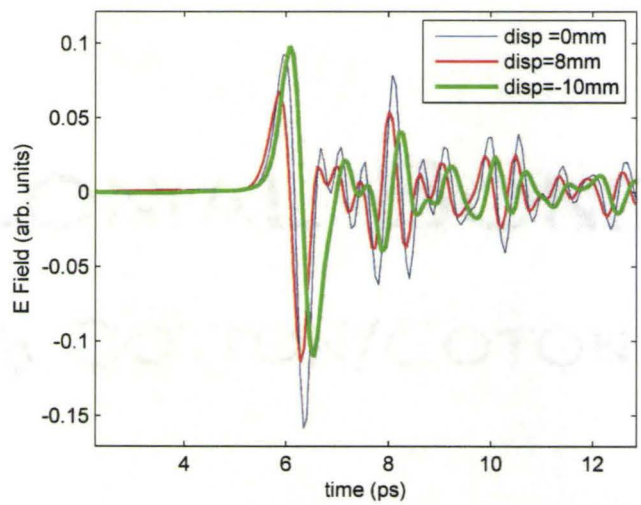

Figure A4.1 Effect of moving the detector crystal from the optimal focal position of the THz beam. "disp=0mm' denotes that the detector crystal is located at the focal spot, and is compared to displacements of 6mm and 10mm. Note that the peak THz electric field is diminished and slightly shifted by moving the focal length on the detector.

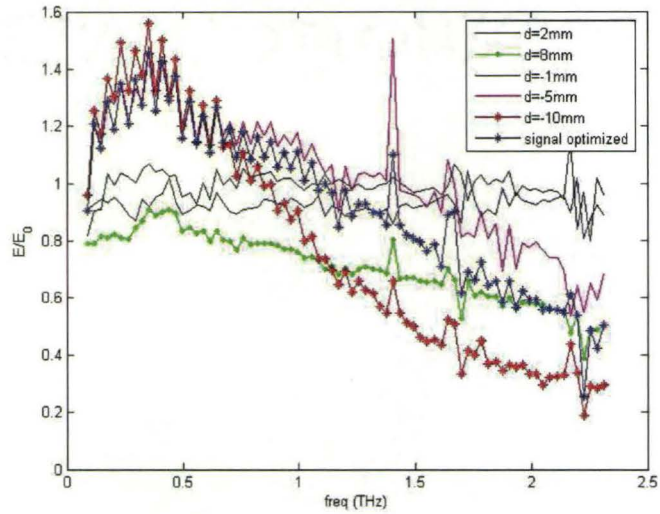

Figure A4.2 The ratio of the electric field detected when the detector crystal is displaced from the THz focal position to the field detected when the position of the detector crystal is optimized. The blue stars represent the case where the detector is positioned to optimize the signal for the main peak of the THz pulse. The frequency dependence suggests that different frequencies have different focal lengths.

A4.2 Overlap of THz spot and IR probe beam on detector crystal

The THz spot must be centered over the IR detector beam to ensure optimal detection of the THz radiation. During the alignment procedure the position of the THz spot on the detector crystal is tweaked to maximize the detected THz signal. Figure A4.3 shows the effect of altering the horizontal position of the THz spot in the detector crystal.

Changing the horizontal position of the THz spot not only affects the overall detected signal strength, but also significantly changes the THz path length, which is interpreted as a phase shift in the electric field. A 0.5mm displacement corresponds to a ~1.5ps shift. Figure A4.4 shows the amplitude of the detected THz electric field for various horizontal displacements of the THz spot. As expected, high frequencies are suppressed when overlap between the THz spot and the detector beam is poor. This illustrates that the spectral components of the THz spot are spatially separated, with high frequencies at the centre of the spot, and low frequencies at the edges.

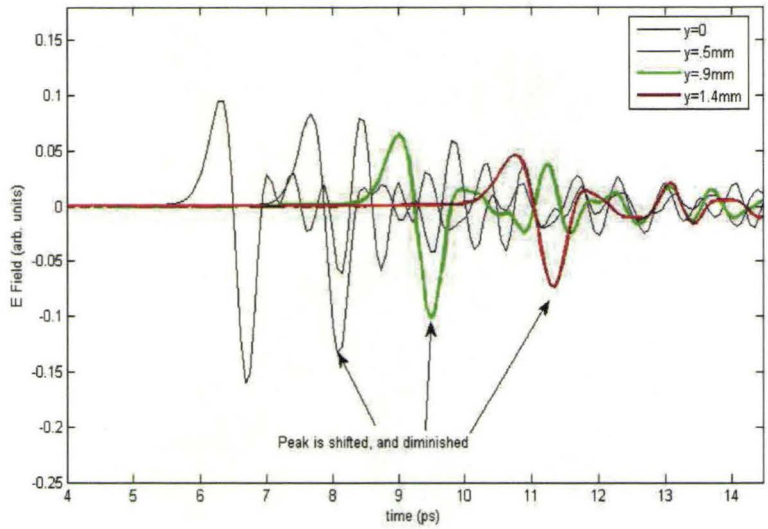

Figure A4.3 The effect on the detection of the THz electric field in the time domain of horizontally displacing the THz beam on the detector crystal, thus reducing the overlap of the THz beam and the IR probe. "y" denotes the displacement. The amplitude of the electric field is reduced. The path length is also significantly affected by the alignment change, as indicated by the shift of the main peak.

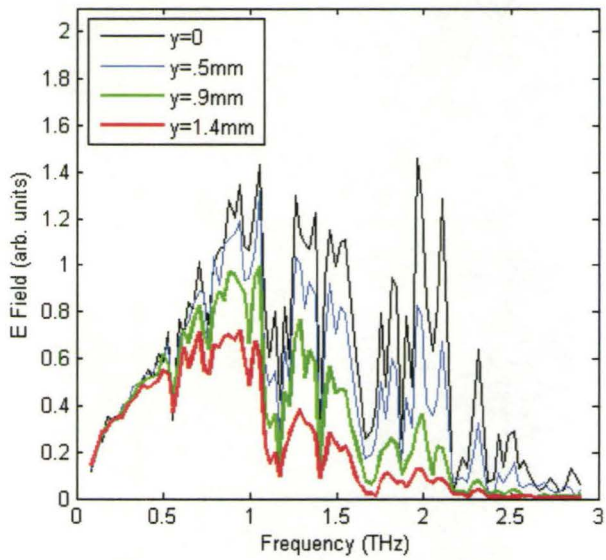

Figure A4.4 The effect on the detection of the frequency dependent electric field by horizontally displacing the THz beam on the detector crystal. The overall amplitude of the electric field is reduced by reducing the overlap between the THz spot and the IR probe. It is interesting to note that the higher frequencies are diminished more, which is consistent with spatial profile of the THz pulse.

The vertical alignment of the THz spot on the detector crystal is also important. Figure A4.5 shows that the measured signal strength decreases as the THz spot is moved vertically from the detector beam position. The path length is not affected appreciably. Figure A4.6 shows that similarly to the horizontal displacements, the high frequencies of the THz spot are not detected when only the edge of the THz spot overlaps with the IR detector beam. A comparison of the sensitivity to vertical and horizontal misalignment of the THz spot on the detector crystal can be seen in Figure A4.7 and Figure A4.8.

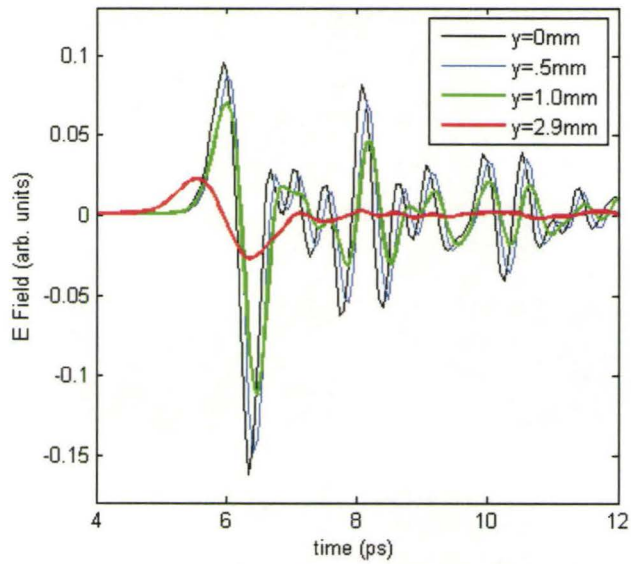

Figure A4.5 The effect on the detection of the electric field in the time domain of vertically displacing the THz beam on the detector crystal, thus reducing the overlap between the THz spot and the IR probe. The amplitude of the electric field is reduced, but the pathlength is not significantly changed.

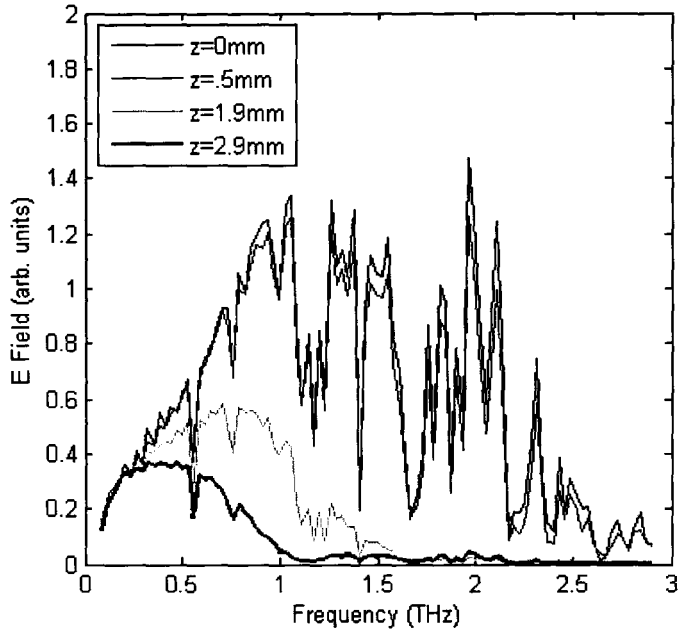

Figure A4.6 The effect on the detection of the electric field in the frequency domain of horizontally displacing the THz beam on the detector crystal. Again, The amplitude of the electric field is reduced by decreasing the overlap between the THz spot and the IR probe.

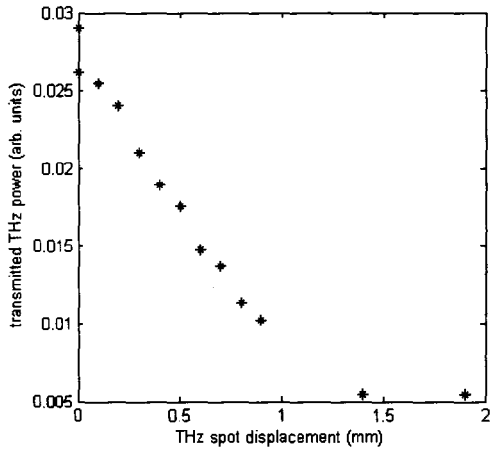

Figure A4.7 Transmitted THz power detected as a function of horizontal beam position on detector crystal

The THz system is more sensitive to horizontal displacements of the THz spot. This is due to beam geometry with respect to the parabolic mirrors. It is important that the position of the THz spot on the detector relative to the detector beam remains consistent between sample and reference measurements, aside from that, improved alignment results in gains to the high frequency content.

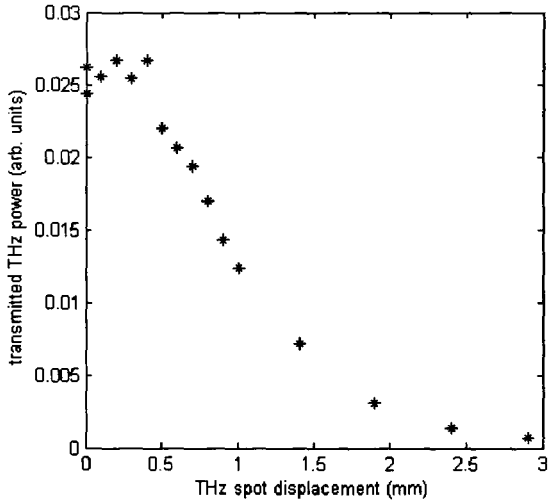

Figure A4.8 Transmitted THz power detected as a function of vertical beam position on detector crystal

Appendix 5. Troubleshooting

A5.1 Maintaining reproducibility during THz experiments

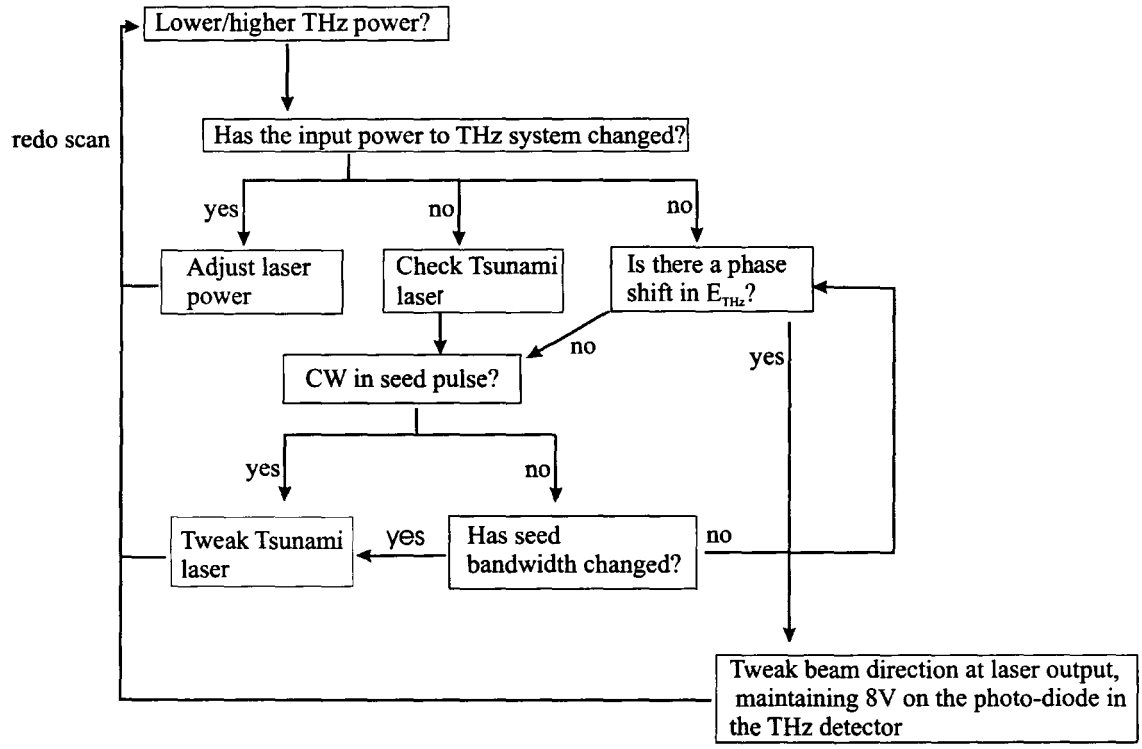

Figure A5.1 Flow chart for troubleshooting drift in the total THz power spectrum.

A5.2 Troubleshooting laser

If the laser amplifier output is very noisy, this indicates a problem with the pockels cell timing, the seed alignment, or the mode locking of the IR laser. If the seed loses mode-locking, the cavity mirrors of the tsunami (the seed laser) must be tweaked.. Using a reference spectrum taken of the seed pulse at the beginning of the day, the seed can be tweaked to minimize any effects on the THz spectrum. Check the bandwidth of the seed pulse. If bandwidth is too narrow (< 45 nm), or if CW is present tweak cavity mirrors to improve seed pulse.

Appendix 6 Birefringence in Lanthanum Aluminate

Initial experiments were carried out on YBCO films grown on Lanthanum Aluminate (LAO), substrates. In many respects LAO is an ideal substrate for THz experiments. It has a close lattice match to YBCO resulting in excellent film quality; it also has no sharp absorption bands in the THz frequency range.[164] Nevertheless, LAO proved to be an unsuitable material for our experiments as can be seen from Figure A6.1. The figure shows the apparent transmitted THz power as a function of the rotation angle of a LAO substrate. The periodicity results not from an anisotropic absorption, but rather from LAO's birefringence.

At high temperatures (above ≈ 500°C) LAO is cubic, but as the temperature is lowered it undergoes a structural phase transition which gives rise to the rhombohedral crystal structure observed at room temperature. The angle in the unit cell is close to 90°, thus LAO is almost cubic. The four-fold symmetry in the figure is consistent with this cubic crystal structure. The apparent change in THz transmission is linked to the measurement process in which the electric field associated with the THz radiation is used to rotate an optical probe in the detector crystal as described in Chapter 1, Section 3.2.

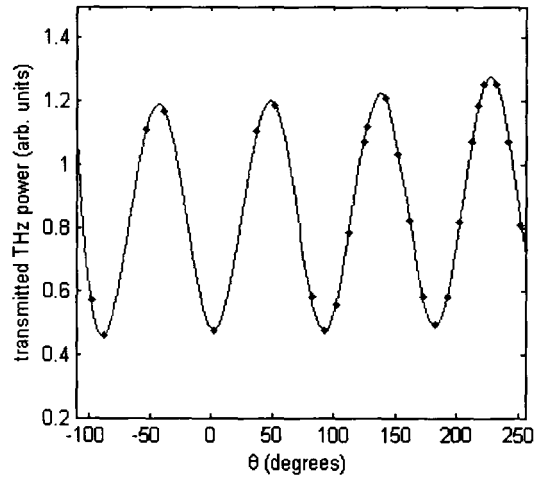

Figure A6.1 Apparent transmitted THz power through LAO as a function of crystal orientation. The angle here refers to the angle between the [010] crystal axis, and the THz polarization.

The detector crystal is aligned to maximize the rotation of the optical probe, and hence the sensitivity to THz radiation. LAO's birefringence can rotate the THz polarization, effectively changing the efficiency of the detection process. The crystal orientation of the sample at 0 degrees represents a 0 degree angle between the [010] axis and the THz polarization.

Figure A6.2 shows the spectral effect of rotating a LAO crystal in a linearly polarized THz beam. The measured THz radiation is minimized at ~2 THz when the crystal is oriented to minimize the apparent transmitted power. As a result, the ratio of the transmitted THz spectra for a crystal orientation that gives maximum THz transmission, to the minimized spectra gives a sharp peak at ~ 2 THz, as seen in Figure A6.2.

The rotation of THz electric field by the LAO crystal is proportional to d/λ (i.e. the ratio of the crystal thickness to the wavelength). This is the origin of the artefact and is what dictates its spectral position. In other words, the LAO acts as a wave plate where the order of the wave plate varies with frequency. A half-wave plate is a particularly interesting case, since it simply acts to rotate a linearly polarized optical field. Our data is consistent with the LAO acting as a half-wave plate near 2 THz. Rotation of the LAO

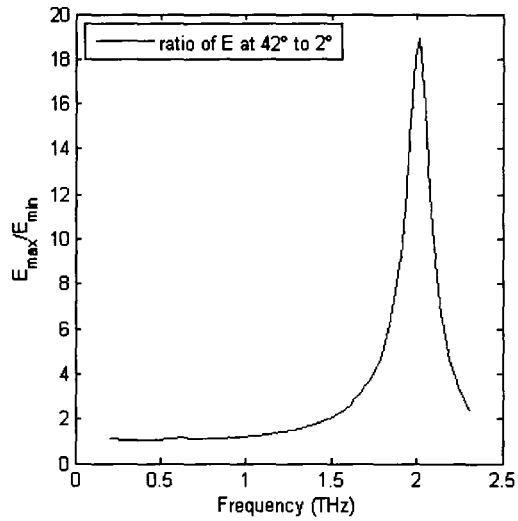

Figure A6.2 Spectral artifact in the ratio of the measured transmitted electric field through LAO oriented to give a nearly maximized THz transmission to the transmission for a crystal orientation corresponding to the minimum transmitted signal.

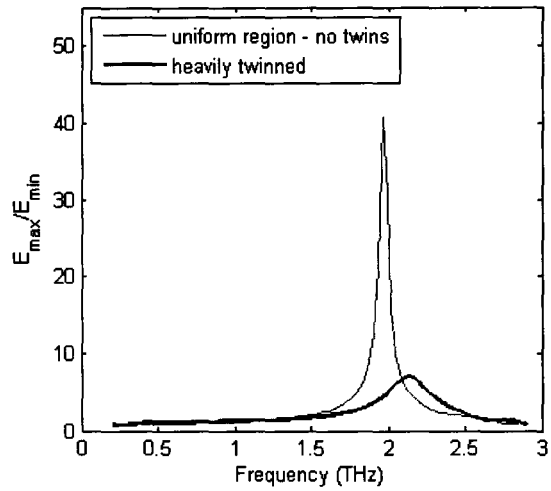

Figure A6.3 The presence of multiple twinning regions smears out the artifact seen in the ratio of the measured transmitted electric field at an orientation of maximum THz detection to an orientation of minimum THz detection.

crystal, can then rotate the optical field to an angle in which the detection efficiency is effectively zero. For all other frequencies, the LAO will not act as a half-wave plate and the THz will be converted to an elliptical polarization.

There is a strong propensity for substrates to develop a twin structure which can be visibly observed using cross polarizers as shown in the micrograph in Figure 4.20. Twinning of the substrate reduces the above effect as can be seen in Figure A6.3, since both domains are present and to an extent cancel each other out. However, even in a heavily twinned substrate, it is unlikely that the domains will exactly cancel and lead to a complete absence of birefringence.

In principal, the role of birefringence could be accounted for in these measurements. However, for an untwined substrate the requirements on aligning the orientation of the substrate to the THz polarization would limit the accuracy of the measurements. Using a twinned substrate would not eliminate this issue and would make measurements sensitive to the precise portion of the sample probed by the THz. To avoid both of these issues, all of the data analyzed in the remainder of this chapter was carried out on films grown on LSAT, a substrate with no birefringence.

Appendix 7. Apparent temperature evolution of an underdoped YBCO film

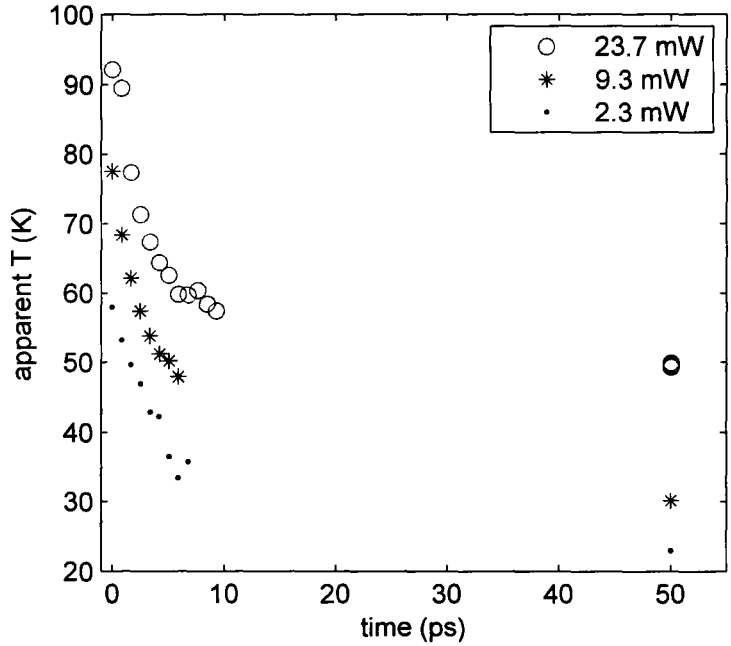

Figure A7.1 Temporal evolution of the apparent change in temperature of an underdoped film (Tc=75K) for differing levels of optical excitation at T=20 K. Note that early recovery does not seem to depend upon levels of optical excitation.

References

[1] J. Bardeen, L.N. Cooper, and J.R. Schrieffer, Phys. Rev. **108**, 1175 (1957)
[2] M. Tinkham, *Introduction to Superconductivity*, 2nd ed., McGraw-Hill, New York, pp. 375-382 (1996)
[3] C.C. Tsuei and J.R. Kirtley, Rev. Mod. Phys. **72**, 969 (2000)
[4] Khee-Kyun Voo, Hong-Yi Chen, and W.C. Wu, Phy. Rev. B **68**, 012505, (2003)
[5] C.J. Gorter, and H,B,G. Casimir Physik. Z. **35**, 963 (1934)
[6] P. M. Marcus, and E. Maxwell, Phys. Rev. **91**, 5, 1035 (1953)
[7] S. Anlage and D. H. Wu, J. Superconductivity **5**, 395 (1992)
[8] D. A. Bonn, R. Liang, T.M. Riseman, D. J. Baar, D. C. Morgan, K. Zhang, P. Dosanjh, T. L. Duty, A. Macfarlane, G. D. Morris, J. H. Brewer and W. N. Hardy, Phys Rev. B **47**, 11314 (1993)
[9] F. London and H. London, Z. Phys. **96**, 359 (1935)
[10] J. D. Doss, Engineers *Guide to High Temperature Superconductivity,* John Wiley & Sons Inc. USA, pp. 49-50 (1989)
[11] K. S. Cole and R. H. Cole, J. Chem. Phys. **9**, 341 (1941)
[12] D. W. Davidson and R. H. Cole, J. Chem. Phys. **19**, 1484 (1951)
[13] G. Williams and D. C. Watts, Trans. Faraday Soc. **66**, 80 (1970)
[14] N. V. Smith, Phys. Rev. B **64**, 155106, (2001)
[15] M. Walther, D. G. Cooke, C. Sherstan, M. Hajar, M. R. Freeman, and F. A. Hegmann, Phys Rev B **76**, 125408 (2007)
[16] A. Thoman, A. Kern, H. Helm, and M. Walther, Phys Rev B **77**, 195405 (2008)
[17] J. B. Baxter and C. A. Schmuttenmaer, J. Phys. Chem. B **110**, 25229 (2006)
[18] G. M. Turner, M. C. Beard, and C. A. Schmuttenmaer, J. Phys. Chem. B **106**, 11716 (2002)
[19] R. Liang, D. A. Bonn and W. N. Hardy, Physica C **304**, 105 (1998)
[20] R. Liang, D. A. Bonn, W. N. Hardy, J. C. Wynn, K. A. Moler, L. Lu, S. Larochelle, L. Zhou, M. Greven, L. Lurio and S. G. J. Mochrie, Physica *C* **383**, 1 (2002)
[21] Ding, T. Yokoya, J.C. Campuzano, T. Takahashi, M. Randeria, M.R. Norman, T. Mochiku, K. Kadowaki, and J. Giapintzakis, Nature **382** , 51 (1996)
[22] T. Timusk , and B. Statt , Reports on Progress in Physics **62,** 61 (1999)
[23] A. G. Loeser, Z.-X. Shen, M. C. Schabel, C. Kim, M. Zhang, and A. Kapitulnik, Phys. Rev. B **56** 14185 (1997)
[24] V. J. Emery, S. A. Kivelson, and O. Zachar Phys. Rev. B **56,** 6120 (1997)
[25] O. Fischer, M. Kugler, I. Maggio-Aprile, C. Berthod, and C. Renner, Rev. Mod. Phys. **79,** 353 (2007)
[26] D. Pines, Physica C 273, 282 (1997)
[27] P. Nozi`eres and F. Pistolesi, Eur. Phys. J. B **10**, 649 (1999)
[28] J.D. Jorgensen, Physics Today **44**, 34 (1991)
[29] M. C. Nuss, P. M. Mankiewich, M. L. O'Malley, E. H. Westerwick, and P. B. Littlewood, Phys. Rev. Lett. **66**, 3305 (1991)
[30] D.N. Basov, and T. Timusk, Rev. Mod. Phys. **77**, 721 (2005)
[31] R. A. Kaindl, M. A. Carnahan, J. Orenstein, D. S. Chemla, H. M. Christen, H.-Y. Zhai, M. Paranthaman, and D. H. Lowndes, Phys. Rev Lett. **88**, 027003 (2002)
[32] R. D. Averitt, G. Rodriguez, A. I. Lobad, J. L. W. Siders, S. A. Trugman, and A. J. Taylor, Phys. Rev. B **63** , 140502 (2001)

[33] D. Grischkowsky, S. Keiding, M. van Exter, and Ch. Fattinger, J Opt. Soc. Am. B **7**, 2006 (1990)
[34] B. Ferguson, and X.C. Zhang, Nature Materials **1**, 26 (2002)
[35] H. F. Tiedje, H. K. Haugen, and J. S. Preston, Opt. Comm. **274**, 187 (2007)
[36] A. G. Markelz, A. Roitberg, and E. J. Heilweil, Chem. Phys. Lett. **320**, 42 (2000)
[37] M. Walther, B. Fischer, M. Schall, H. Helm, and P. Uhd Jepsen, Chem. Phys. Lett. **332**, 389 (2000)
[38] M. C. Beard, G. M. Turner, and C. A. Schmuttenmaer, J. Phys. Chem. B **106**, 7146 (2002)
[39] R.D.Averitt, A.J. Taylor, J. Phys. Condens. Matter **14,** R1357 (2002)
[40] D. Grischkowsky, and S. Keiding, Appl. Phys. Lett. **57**, 1055 (1990)
[41] A. Rice, Y. Jin, X. F. Ma, X-C. Zhang, D. Bliss, J. Larkin, and M. Alexander, Appl. Phys. Lett. **64**,1324 (1994)
[42] M. C. Teich, Appl. Phys. Lett. **14**, 201 (1969)
[43] E. R. Brown, F. W. Smith, and K. A. McIntosh, J. Appl. Phys. **73,** 1480 (1993)
[44] S. Krishnagopal and V. Kumar, Radiat. Phys. Chem. **70**, 559 (2004)
[45] H. P. Freund and G. R. Neil, Proceedings of IEEE **87,** 782 (1999)
[46] F. Wang, D. Cheever, M. Farkhondeh, W. Franklin, E. Ihloff, J. van der Laan, B. McAllister, R. Milner, C. Tschalaer, D. Wang, D. F. Wang, A. Zolfaghari, T. Zwart, G.L. Carr, B. Podobedov, and F. Sannibale, Phys. Rev. Lett. **96,** 064801 (2006)
[47] T. Y. Chang and T. J. Bridges, Opt. Commun.**1**, 423 (1970)
[48] M. Inguscio, G. Moruzzi, K. M. Evenson, and D. A. Jennings, J. Appl. Phys. **60**, R161 (1986)
[49] J. Ward, E. Schlecht, G. Chattopadhyay, A. Maestrini, J. Gill, F. Maiwald, H. Javadi, and I. Mehdi, IEEE MTT-S Int. Microwave Symp. Dig. **3**, 1587 (2004)
[50] V. Krozer, G. Loata, J. Grajal de la Fuente, and P. Sanz, Proceedings of IEEE Tenth International Conference on Terahertz Electronics, 109 (2002)
[51] Spectra-Physics Lasers, Spitfire *User Manual,*California (2002)
[52] C. Rulliere, A. Bonvalet, and M. Joffre, *Femtosecond Laser Pulses*, Springer, New York, pp. 285-291 (1998)
[53] A. Nahata, A. S. Weling, and T. F. Heinz, Appl. Phys. Lett. **69**, 2321 (1996)
[54] Susuma Namba, J. Opt. Soc. Am. **51**, 76 (1961)
[55] C. Kittel, *Introduction to Solid State Physics*, 7th Ed. John Wiley & Sons Inc., New York pp.312 (1996)
[56] N. W. Ashcroft, N. D. Mermin, *Solid State Physics* Harcourt, Inc., USA pp. 562-568, (1976)
[57] J. H. Van Vleck, Phys. Rev. **59**, 724 (1941)
[58] N. Gedik , J. Orenstein, R. Liang, D.A. Bonn, and W. Hardy, Physica C **408**, 690 (2004)
[59] A. Rothwarf, and B.N. Taylor, Phys Rev. Lett. **19,** 27 (1967)
[60] K.E.Gray, *Nonequillibrium Superconductivity, Phonons, and Kapitza Boundaries* Plenum Press, New York, (1981).
[61] Nathan Bluzer, J. Appl. Phys.**71,** 1336 (1992)
[62] G.P. Segre, N. Gedik, J. Orenstein, D.A. Bonn, R. Liang, and W. N. Hardy, Phys. Rev. Lett. **88,** 137001 (2002)
[63] M. Tinkham, *Introduction to Superconductivity*, 2nd ed., McGraw-Hill, New York, pp. 99 (1996)
[64] R. Buhleier, S.D. Brorson, I.E. Trofimov, J.O. White, H.-U. Habermeier, and J. Kuhl, Phys. Rev. B **50**, 9672 (1994)
[65] T. Kiwa, and M. Tonouchi, Physica C **362**, 314 (2001)

[66] S.D. Brorson , R. Buhleier, I.E. Trofimov, J.O. White, Ch. Ludwig, F. F. BalaKirev, H.-U. Habermeier, J. Kuhl, and J. Opt. Soc. Am. B **13**, 1976 (1996)
[67] H.L. Liu, M. Quijada, D.B. Romero, D.B. Tanner, A. Zibold, G.L. Carr, H. Berger, L. Forró, L. Mihaly, G. Cao, Beom-Hoan O, J.T. Markert, J. P. Rice, M. J. Burns, and K. A. Delin, Ann. Phys. **15,** 606 (2006)
[68] D. A. Bonn, P. Dosanjh, R. Liang, and W. N. Hardy, Phys. Rev. Lett. **68**, 2390 (1994)
[69] F. Gao, G. L. Carr, C. D. Porter, D. B. Tanner, G. P. Williams,C. J. Hirschmug, B. Dutta, X. D. Wu, and S. Etemad, Phys. Rev. B **54**, 700 (1996)
[70] A. Frenkel, F. Gao, Y. Liu, J.F. Whitaker, C. Uher, S.Y. Hou, and J. M. Phillips, Phys. Rev. B **54**, 1355 (1996)
[71] W.N. Hardy, D.A. Bonn, D.C. Morgan, and R. Liang, Phys. Rev. Lett. **70**, 3999 (1993)
[72] I. Wilke, M. Khazan, C.T. Rieck, P. Kuzel, C. Jaekel, and H. Kurz, Pysica C **341,** 2271 (2000)
[73] J. Corson, J. Orenstein, S. Oh, J. O'Donnell, and J. N. Eckstein, Phys. Rev. Lett. **85**, 2569 (2000)
[74] J. R. Waldram, P. Theopistou, A. Porch, and H.-M. Cheah, Phys. Rev. B **55**, 3222 (1997)
[75] R. D. Averitt, G. Rodriguez, J. L. W. Siders, S. A. Trugman, and A. J. Taylor, J Opt Soc. Am B **17**, 327 (2000)
[76] Y. Yominari, H. Murakami, and M. Tonouchi, Chin. J. of Phys. **42**, 561 (2004)
[77] M. Tonouchi, M. Tani, Z, Wang, K, Sakai, N. Wada, and M. Hangyo, Jpn. J. Appl. Phys. **35**, L1578 (1996)
[78] H. Wald, P. Seidel, and M. Tonouchi, Physica C **367**, 308 (2002)
[79] Hagen Wald, Paul Seidel, and Masayoshi Tonouchi, IEEE Transactions on Applied Superconductivity **13**, 1020 (2003)
[80] V. V. Kabanov, J. Demsar, B. Podobnik, and D. Mihailovic, Phys Rev B **59**, 1487 (1999)
[81] S. G. Han, Z. V. Vardeny, K. S. Wong, O. G. Symco, and G. Koren, Phys. Rev. Lett. **65**, 2708 (1990)
[82] C. J. Stevens, D. Smith, C. Chen, J. F. Ryan, B. Podobnik, D. Mihailovic, G. A. Wagner, and J. E. Evetts, Phys. Rev. Lett. **78**, 2212 (1997)
[83] J. Demsar, B. Podobnik, V. V. Kabanov, Th. Wolf, and D. Mihailovic, Phys Rev Lett. **82,** 4918 (1999)
[84] R. A. Kaindl, M. Woerner, T. Elsaesser, D. C. Smith, J. F. Ryan, G. A. Farnan, M. P. McCurry and D. G. Walmsley, Science **287**, 470 (2000)
[85] R. A. Kaindl, M. A. Carnahan, D. S. Chemla, S. Oh, and J. N. Eckstein, Phys. Rev. B **72**, 060510 (2005)
[86] J. Demsar, R.D. Averitt, and A.J. Taylor, Journal of Superconductivity: Incorporating Novel Magnetism **17**, 143 (2004)
[87] M.A. Carnahan, R.A. Kaindl, J. Orenstein, D.S. Chemla, S. Oh, and J. N. Eckstein, Physica C **408**, 729 (2004)
[88] P. Kusar, V.V. Kabanov,1 J. Demsar, T. Mertelj, S. Sugai, and D. Mihailovic, Phys. Rev. Lett. **101**, 227001 (2008)
[89] N. Gedik, P. Blake, R.C. Spitzer, J. Orenstein, Ruixing Liang, D.A. Bonn, and W.N. Hardy, Phys. Rev. B **70**, 014504 (2004)
[90] R. A. Kaindl, M. Woerner, T. Elsaesser, D. C. Smith, J. I Ryan, G. A. Farnan, M. P. McCurry, and D. G. Walmsley, Physica C **341**, 2213 (2000)
[91] M.V. Sadovskii, Physics-Uspekhi **44**, 515 (2001)

[92] G. Blatter, M.V. Feigel'man, V.B. Geshkenbein, A.I. Larkin, and V.M Vinokur, Rev. Mod. Phys. **66,** 1125 (1994)
[93] O. M. Auslaender, L. Luan, E. W. J. Straver, J. E. Hoffman, N. C. Koshnick, E. Zeldov, D. A. Bonn, R. Liang, W. N. Hardy , and K. A. Moler Nature Physics **5**, 35 (2009)
[94] H. J. Lee, J. H. Jung, K. W. Kim, M. W. Kim, T. W. Noh, Y. J. Wang, W. N. Kang, Eun-Mi Choi, Hyeong-Jin Kim, and Sung-Ik Lee, Phys. Rev. B **65,** 224519 (2002)
[95] J. M. Tranquada, B. J. Sternlieb, J. D. Axe, Y. Nakamura, and S. Uchida Nature **375**, 561(1995)
[96] D. Reznik, L. Pintschovius, M. Ito, S. Iikubo, M. Sato, H. Goka, M. Fujita, K. Yamada, G. D. Gu, and J. M. Tranquada, Nature **440**, 1170 (2006)
[97] S. H. Pan, J. P. O'Neal, R. L. Badzey, C. Chamon, H. Ding, J. R. Engelbrecht, Z. Wang, H. Eisaki, S. Uchida, A. K. Guptak,K.-W. Ngk, E. W. Hudson, K. M. Lang, and J. C. Davis, Nature **413**, 282 (2001)
[98] J. Lee, J. A. Slezak, and J.C. Davis, J. Phys. and Chem. of Solids **66,** 1370 (2005)
[99] V. J. Emery and S. A. Kivelson, Phys. Rev. Lett. **64**, 475 (1990)
[100] V.J. Emery, S.A. Kivelson, and J.M. Tranquada, Proc. Natl. Acad. Sci. USA **96**, 8814 (1999)
[101] K. M. Lang, V. Madhavan, J. E. Hoffman, E. W. Hudson, H. Eisaki, S. Uchida, and J. C. Davis, Nature **415**, 412 (2002)
[102] M. Brucherseifer, A Meltzow-Altmeyer, P. Haring Bolivar, H. Kurz, and P. Seidal, Physica C **399**, 53 (2003)
[103] P. Y. Han, M. Tani, M. Usami, S. Kono, R. Kersting, and X.C. Zhang, J. Appl. Phys. **89**, 2357 (2001)
[104] Martin van Exter, Ch. Fattinger, and D. Grischkowsky Optics Letters **14**, 1128 (1989)

[105] Y. Lu, R.A. Hughes, T.Strach, T. Timusk, D. Poulin, and J.S. Preston, Physica C **197,** 75 (1992)
[106] A.W. McConnell, R.A. Hughes, A. Dabkowski, H.A. Dabkowska, J.S. Preston, J.E. Greedan, and T. Timusk, Physica C **225**, 7 (1994)
[107] J. Nam, PhD thesis, McMaster University (2005)
[108] R.A. Hughes, The optical properties of high-Tc superconductors grown by laser deposition, Ph.D. Thesis,McMaster University (1992)
[109] S. Geller and V.B. Bala, Acta Cryst. **9**, 1019 (1956)
[110] K. Abe, S. Komatsu, J. Appl. Phys. **77**, 6461 (1995)
[111] D. Dijkkamp, T. Venkatesen, X.D. Wu, S.A. Shaheen, N. Jisrawi, Y.H. Min-Lee, W.L. McLean, and M. Croft, Appl. Phys. Lett. **51**, 619 (1987)
[112] D. Schweitzer, T. Bollmeier, B. Stritker, and B. Rauschenbach, Thin Solid Films **280**, 147 (1996)
[113] M. Bauer, F. Baudenbacher, and H. Kinder, Physica C **246**, 113 (1995)
[114] S. C. Tidrow, A. Tauber, T. W. D. Wilber, R. T. Lareau, C. D. Brandle, G. W. Berkstresser, A. J. Ven Graitis, D. M. Potrepka, J. I. Budnick, and J. Z. Wu, IEEE Trans. App. Supercon. **7**, 1766 (1997)
[115] H. Y. Zhai, and W. K. Chu, Appl. Phys. Lett. **76**, 3469 (2000)
[116] F. Kadlec, P. Kuzel, and J. L. Coutaz, Opt. Lett. **30**, 1402 (2005)
[117] W.S. Fann, R. Storz, T. HWK, and J. Bokor, Phys. Rev. B **46**, 13592 (1992)
[118] J. Hermanson, J. Anderson, and G. Lapeyere, Phys. Rev.B **12,** 5410 (1975)
[119] J. Lambe, A.P. Thakoor, S.K. Khanna, J. Vac. Sci. & Tech. A, **2**, 2, 792 (1984)

[120] S. Kohiki, K. Oki, J. Electron Spectroscopy and Related Phenomena, **36,** 105, (1985)
[121] A. J. Gatesman, R. H. Giles, J. Waldman,J. Opt. Soc. Am. B, 12, 2, 212 (1995)
[122] A. Kuramata, K. Horino, K. Domen, et al. App. Phys. Lett. **67**,17, 2521, (1995)
[123] Y.F. Chen, S.K. Hong, H.J. Koh et al. App. Phys. Lett. **76,** 2, 245 (2000)
[124] Y.F. Chen, D.M Bagnall, H.J. Koh, et al. J. App. Phys. **84**, 7, 3912 (1998)
[125] R. E. Prange, H. D. Drew, and J. B. Restorff, J. Phys. C: Solid State Phys. **10**, 5083 (1977)
[126] A. Hosseini, R. Harris, Saeid Kamal, P. Dosanjh, J. Preston, R. Liang, W. N. Hardy, and D. A. Bonn, Phys. Rev. B **62**, 1349 (1999)
[127] P. C. Hammel, M. Takigawa, R. H. Heffner, Z. Fisk and K. C. Ott, Phys. Rev. Lett. **63**, 1992 (1989)
[128] Y. Kuroda and C. M. Varma, Phys. Rev. B **42**, 8619 (1990)
[129] R. E. Walstedt, W. W. Warren, R. F. Bell, G. F. Brennert, G. P. Espinosa, R. J. Cava, L. F. Schneemeyer, and J. V. Waszczak, Phys. Rev. B **38**, 9299 (1988)
[130] S. E. Barrett, D. J. Durand, C. H. Pennington, C. P. Slichter, T. A.Friedmann, J. P. Rice, and D. M. Ginsberg, Phys. Rev. B **41**, 6283 (1990)
[131] H. Saha, and P. Basu, Solid State Electronics **20**, 553 (1977)
[132] T.R. Tsai, C.C. Chi, and S.F. Horng, Physica C **391**, 281 (2003)
[133] MatLab, The MathWorks, Inc. 2004
[134] T. Valla, A. V. Fedorov, P. D. Johnson, B. O. Wells, S. L. Hulbert, Q. Li, G. D. Gu and N. Koshizuka, Science **285**, 2110 (1999)
[135] S. D. Brorson, R. Buhleier, J. O. White, I. E. Trofimov, H.-U. Habermeier, and J. Kuhl, Phys. Rev. **49**, 6185 (1994)
[136] A.T. Fiory , A.F. Herbard, P.M. Mankiewich, and R.E. Howard, Phys. Rev. Lett. **61**, 1419 (1988)
[137] L. A. de Vaulchier, J. P. Vieren, A. El Azrak, Y. Guldner, N. Bontemps, M. Guilloux-Viry, C. Le Paven-Thivet, and A. Perrin, Phys Rev B **52**, 564 (1995)
[138] N. Gedik, M. Langer, J. Orenstein, S. Ono, Y. Abe, and Y. Ando, Phys Rev Lett. **95**, (2005)
[139] R.D. Averitt, V.K.Thorsmølle, Q.X. Jia, S.A. Trugman, and A.J. Taylor Physica B **312,** 86 (2002)
[140] V.G. Bessergenev, Yu.A. Kovalevskaya, V.N. Naumov, and G.I. Frovlova, Physica C **245**, 36 (1995)
[141] Oxford Instruments, *Catalogue* (2004)
[142] Hsu-Feng Lai, and Juh Tzeng Lue, Materials Chemistry and Physics **40**, 126 (1995)
[143] H. Sakowksa, M. Swirkowicz, K. Mazur, T. Lukasiewicz, and A. Witek, Cryst, Res. Technol. **36**, 8 (2001)
[144] P. C. Howell, A. Rosch, and P. J. Hirschfeld, Phys. Rev. Lett. **92**, 037003 (2004)

[145] J. Orenstein, "Optical Conductivity and Spatial Inhomogeneity in Cuprate Superconductors,"*Handbook of High Temperature Superconductivity*, Springer, New York pp. 299-322 (2007)
[146] T.W. Noh, S.G. Kaplan, and A.J. Sievers, Phys. Rev. Lett. **62**, 599 (1989)
[147] Muhammad Sahimi, *Heterogeneous Materials I: Linear Transport and Optical Properties*, Springer New York, pp. 192 (2003)
[148] W.R. Tinga, W.A.G. Voss, and D.F. Blossey, J. Appl. Phys. **44**, 3897 (1973)
[149] P. Sheng, Phys. Rev. Lett. **45**, 61 (1980)
[150] J. Sturm, P. Grosse, S. Morley, and W. Theiss, Z. Phys. D **26**, 195 (1993)

[151] A. Diaz, J. Maza, and Felix Vidal, Phys. Rev. B **55**, 1209 (1997)
[152] T. C. Choy, and A. M. Stoneham, J. Phys.: Condens. Matter **2,** 939 (1990)
[153] E. Gorges, P. Grosse, and W. Theiss, Z. Phys. B **97**, 49 (1995)
[154] D.A.G. Bruggeman, Ann. Phys. Leipzig **24**, 636 (1935)
[155] D.J. Bergman, and D. Stroud, *Solid State Physics- Advances in Researcch and Applications*, Academic Press California, **46** pp. 147 (1992)
[156] S. V. Barabash, and D. Stroud, Physica B **338**, 224 (2003)
[157] T. C. Choyt and A. M. Stoneham, J. Phys.: Condens. Matter **2**, 939 (1990)
[158] P. U. Jepsen, B. M. Fischer, A. Thoman, H. Helm, J. Y. Suh, R. Lopez, and R. F. Haglund, Jr, Phys. Rev. B **74**, 205103, (2006)
[159] Jinho Lee, J. A. Slezak, and J.C. Davis, J. Phys. and Chem. of Solids **66**,1370 (2005)
[160] S. A. Kivelson and E. Fradkin, "Optical Conductivity and Spatial Inhomogeneity in Cuprate Superconductors,"*Handbook of High Temperature Superconductivity*, Springer, New York pp. 572-573 (2007)
[161] P. D. Cunningham, and L. M. Hayden, J. Phys. Chem. C **112**, 7928 (2008)
[162] J. Rozen, R. Lopez, R. F. Haglund, Jr., and L. C. Feldman, App. Phys. Lett. **88**, 081902 (2006)
[163] A.S. Moskvin, E.V. Zenkov, and Yu.D. Panov, J. of Luminescence **94–95**, 163(2001)
[164] J. Sturm, P. Grosse, S. Morley, and W. Theiss, Supplement to Z. Phys. D **26**, S 195 (1993)
[164] D. Grischkowsky, S. Keiding, Appl. Phys. Lett. **57**, 1055 (1990)